CR-152334

Acurex Project 7396

GALILEO PROBE THERMAL PROTECTION: ENTRY HEATING ENVIRONMENTS AND SPALLATION EXPERIMENT DESIGN

A. Balakrishnan, W. Nicolet, S. Sandhu, J. Dodson

Acurex Corporation/Aerotherm
Aerospace Systems Division
485 Clyde Avenue
Mountain View, California 94042

November 1979

ACUREX FINAL REPORT FR-79-21/AS

Prepared for
Ames Research Center
National Aeronautics and Space Administration

Contract No. NAS2-9909

(NASA-CR-152334) GALILEO PROBE THERMAL PROTECTION: ENTRY HEATING ENVIRONMENTS AND SPALLATION EXPERIMENTS DESIGN Final Report (Acurex Corp., Mountain View, Calif.) 133 p HC A07/MF A01 CSCL 22B G3/18

N80-14184

Unclas
43831

Acurex Project 7396

GALILEO PROBE THERMAL PROTECTION: ENTRY HEATING ENVIRONMENTS AND SPALLATION EXPERIMENT DESIGN

A. Balakrishnan, W. Nicolet, S. Sandhu, J. Dodson

Acurex Corporation/Aerotherm
Aerospace Systems Division
485 Clyde Avenue
Mountain View, California 94042

November 1979

Acurex Final Report FR-79-21/AS

Prepared for
Ames Research Center
National Aeronautics and Space Administration

Contract No. NAS2-9909

FOREWORD

The work reported in this document was performed for NASA-Ames Research Center under contract NAS2-9909. Mr. W. E. Nicolet* contributed Section 2, Mr. S. S. Sandhu contributed Section 4, and Mr. J. D. Dodson is responsible for the work described in Section 5. The rest of the sections were written by Dr. A. Balakrishnan. During the period of performance of this contract, Dr. C. T. Nardo was the business area manager and Mr. J. T. Howe was the NASA technical monitor. The authors wish to thank Dr. Nardo and Mr. Howe for their valuable assistance during the course of this program.

PRECEDING PAGE BLANK NOT FILMED

---

*Presently at Thermal Sciences, Inc., Sunnyvale, California

TABLE OF CONTENTS

TABLE OF CONTENTS (Concluded)

Section Page

LIST OF ILLUSTRATIONS

Figure Page

LIST OF ILLUSTRATIONS (Continued)

LIST OF ILLUSTRATIONS (Continued)

LIST OF ILLUSTRATIONS (Concluded)

LIST OF TABLES

LIST OF TABLES (Concluded)

LIST OF SYMBOLS

English letters

A	constant, probe forebody surface area
a	constant
B	base
b	constant
B	blowing parameter
C_H	smooth wall Stanton Number
C_f	friction coefficient
c	constant
C_p	specific heat at constant pressure
D	drag
d	diameter, constant
e	constant
F	quantity defined by Equation (3-9)
g	gravitational constant
H	shape factor, enthalpy
H_{ab}	heat of ablation
h	enthalpy
M	Mach number
m	mass fraction
$\dot{m}$	mass removal/injection rate
n	quantity defined by Equation (3-23)
P	quantity defined by Equation (3-36)
Pr	Prandtl number
p	pressure

LIST OF SYMBOLS (Continued)

q	heating rate
Re	Reynolds number
R	radius, recovery factor
r	radial distance
s	streamwise distance, recession
s	recession rate
T	temperature
t	time
u	velocity in streamwise direction
U	shock velocity
V	entry velocity of probe
v	velocity normal to wall
x	mole fraction, coordinate
y	coordinate

<u>Greek letters</u>

β	ballistic coefficient
γ	entry angle
δ	shock standoff distance, boundary layer thickness
δ^*	displacement thickness
ε	emissivity, eddy diffusivity
η	nondimensional variable
θ	cone half angle, momentum thickness
μ	dynamic viscosity
π	3.1415927

LIST OF SYMBOLS (Concluded)

ρ	density
σ	Stefan-Boltzman constant
τ	shear stress
ϕ	energy thickness
Ψ	nondimensional distance

Subscripts

B	base
C	convective
c	cone angle
e	edge value
f	friction
H	heat transfer
h	heat
i	inviscid
l	laminar
M	mass transfer
N	nose
R	radiative
s	streamwise, shock
t	turbulent, total
w	wall value
o	stagnation point, origin
∞	freestream

SECTION 1

INTRODUCTION

The National Aeronautics and Space Administration (NASA) is planning to launch a Jupiter Orbiter Probe during 1984. The goals of the mission (recently designated Galileo) are to explore the planet Jupiter and to gather clues to the origin of the solar system. The probe will carry an array of instruments for investigating the Jupiter atmosphere, including instruments to measure the atmospheric composition and perform a local radiative energy balance.

Because Jupiter is a massive planet, with roughly six times the gravity of Earth, the inertial velocity of the entry probe will be approximately 60 km/sec. However, Jupiter has a high rotational speed of about 12 km/sec. Using this rotational speed during the entry trajectory results in a relative entry velocity of roughly 48 km/sec. Because this is a hypersonic entry into a highly radiatively participating atmosphere, strong shocks envelope the probe, creating an extremely hostile radiative and convective heating environment.

To accommodate the intense entry heating, effective thermal protection systems must be designed. The heatshield must be able to withstand the intense heating, yet be light enough that a maximum payload of scientific instruments can be housed. Carbon-phenolic has been identified as the baseline material for this mission. As earlier studies show, carbon-phenolic can provide the required thermal protection for a heatshield weight allocation of 30 to 45 percent of the probe weight.

The heating environment is the primary factor affecting the weight of the heatshield. Predictions of the heating environment must consider several physical parameters including the atmospheric composition of the planet, the probe configuration, entry angle and velocity, and the probe shape change effects. Radiative and convective heating rates are also significantly affected by the massive blowing. Figure 1-1 shows the candidate Galileo probe configuration.

The objectives of the present study are to generate heating environments for the entry probe, to define an experiment to assess the importance of heatshield spallation, and to fabricate graphitic materials that contain transition metals. Additional objectives of this study are to investigate the vortical layer effects on cold wall convective heating rate and to assess the importance of entropy layer on cold wall radiative heating rate.

The following sections present the results of this study. Section 2 develops a valid procedure for predicting wall heating and ablation rates about the probe forebody. Solutions for Jupiter Orton model nominal atmospheric entry are obtained and are compared with other existing solutions. Solutions are also presented for the candidate Galileo probe at entry conditions for which results are not available.

Entropy layer effects on convective heating rate are analysed and the computed results are presented in Section 3. The momentum-energy integral technique is used to assess the influence of vortical layer on heating rate.

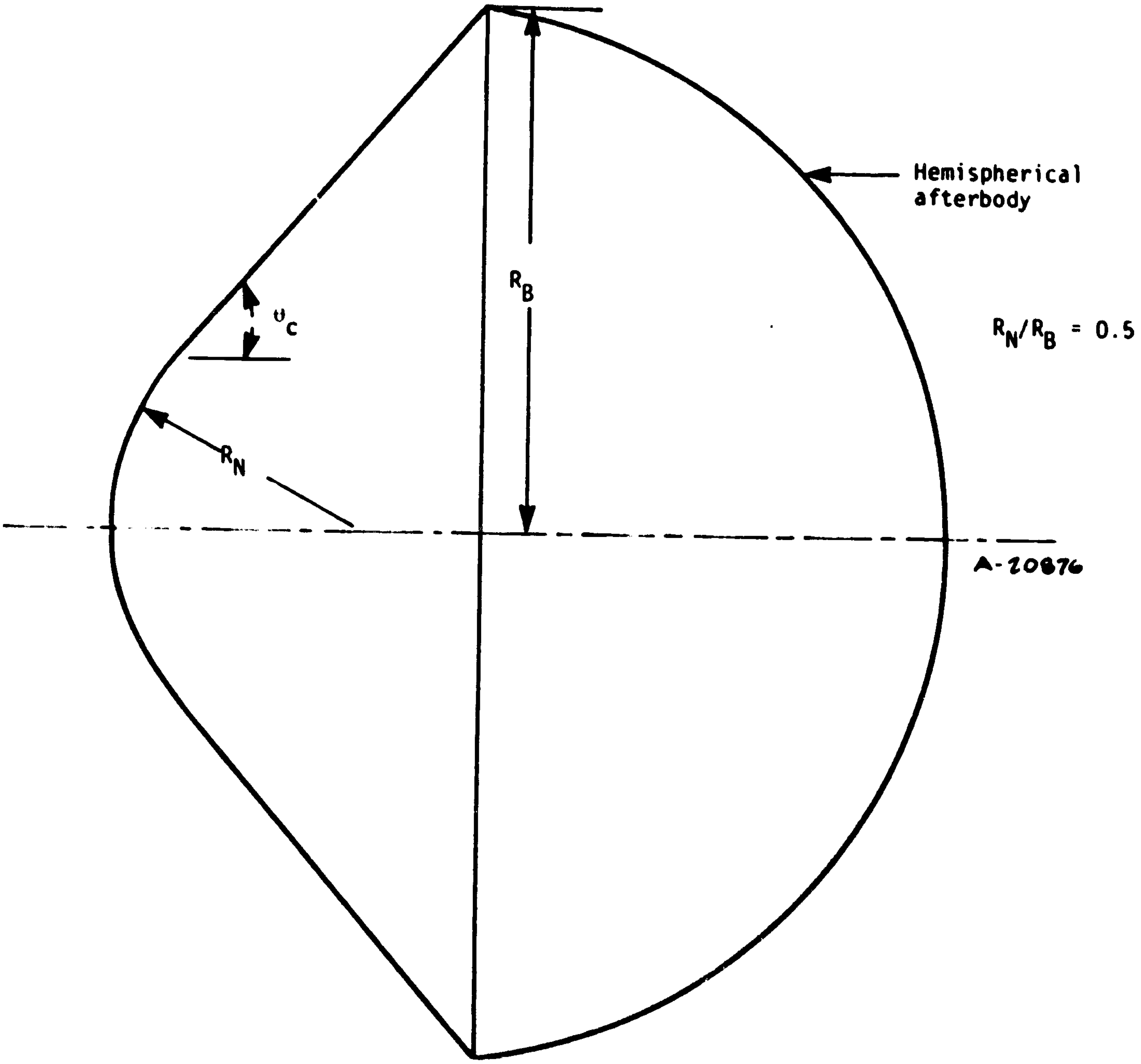

Figure 1-1. Entry Probe Configuration

The heating environment drives the material response which is usually estimated assuming that thermochemical ablation is the only mechanism for mass removal. However, if the heathsield loses material by mechanical erosion or spallation, the weight of heatshield will increase. This increased weight is a real threat to the Galileo mission. To assess the importance of spallation, an earlier study recommended an experimental approach. In Section 4, results of a feasibility study to perform an experiment, a candidate test facility, and a test matrix are presented.

Though carbon-phenolic has been identified as the candidate heatshield material for the Galileo probe, the severe entry heating conditions and the large required weight of heatshield, prompted a recommendation to investigate newly developed metal containing carbon-carbon materials. Section 5 summarizes the material selection, fabrication, and evaluation of the metal containing carbon-carbon composites for use on the Galileo probe.

Several models are available to describe the Jovian atmospheric structure. The effect of the various models on entry heating environment are investigated in Section 6. Entry trajectory calculations performed earlier assumed that the planet is a sphere. However, planet Jupiter is a oblate spheroid. The effect of nonspherical shape of the planet on entry trajectory is also considered in Section 6.

SECTION 2

OFF-STAGNATION POINT FLOWFIELDS FOR PLANETARY ENTRY PROBES

The important physical events encountered during planetary entry are significantly different from those encountered during earth reentry. In particular, the shock layer radiation causes massive ablation from the wall which affects the entire flowfield; the viscous/mixing region assumes the character of a free shear/mixing region instead of a boundary layer. This requires a significantly different modeling approach. Transition and turbulence are also important since they change the character of the mixing layer and, consequently, change the radiation flux reaching the wall. Therefore, benchmark solutions of the radiation coupled flowfield equations are necessary to (1) understand the physical events driving the aerothermodynamic heating, (2) support the design of candidate heatshields, and (3) support the selection of approximate methods and/or correlations for use in engineering trade studies.

The objective of the present study is to develop a valid procedure for predicting wall heating and ablation rates about the probe body. Methods for predicting these quantities at the stagnation point were described in a previous study (Reference 2-1). In the present study, the methodology is extended to off-stagnation conditions. Emphasis is on (1) the nonsimilar terms in the equations, (2) the turbulence terms, and

(3) the solution procedure. Reference 2-2 discusses the formulation and solution procedure. This discussion presents solutions, compares laboratory data to assess the sensitivity of the predictions to basic assumptions, and compares with the predictions of Moss (Reference 2-3) for the Jupiter entry. Heating environments over the candidate Galileo probe at entry conditions for which heating rates have not previously been available are also presented.

2.1 PREDICTIONS OF LABORATORY EXPERIMENTS

The highly cooled turbulent boundary layer data of Hopkins and Nerem (Reference 2-4) were selected for the first set of comparisons. The experiment consisted of a shock tube used as a driver to produce a high enthalpy, supersonic flow inside a tube. Instrumentation included uncoated platinum calorimeter heat transfer gages positioned at 2.54, 6.35, 8.90, 11.4, and 14 cm from the leading edge to measure the heat transfer distribution along the tube during steady flow conditions. A schematic of the apparatus and the flow conditions are given in Figure 2-1. This is a moderate Reynolds number; supersonic flow of high-temperature dissociated air composed primarily of nitrogen, oxygen, and oxygen atoms. The ratio of edge-to-wall temperature puts this experimental data in the highly cooled boundary layer category. The boundary layer was artificially tripped to turbulent flow at a point 2.5 cm from the leading edge, roughly the distance at which natural transition occurs (tripping the boundary layer simply ensures turbulent flow beyond the 2.5 cm station). The precise location of transition is useful when comparing analyses to data because it eliminates the uncertainty caused by intermittent turbulent flow.

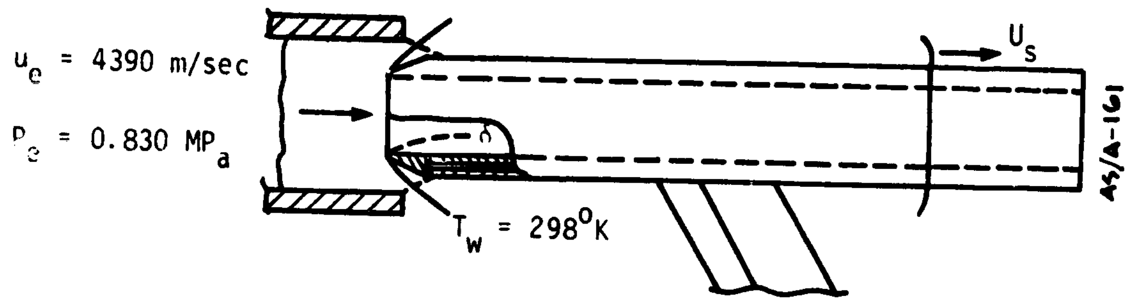

Figure 2-1. Schematic of Hopkins and Nerem's Apparatus

The predictions, compared to the data in Figure 2-2, are comprised of two different codes and five versions of the mixing length model. The present code, without density in the expression for the mixing length, is in very good agreement with the data and is closer than any of the others. With density in the mixing length equation, the present procedure significantly overpredicts the data.

The other predictions shown in Figure 2-2 were made with the Boundary Layer Integral Matrix Procedure (BLIMP) as modified by Bonnett and Evans (Reference 2-5). BLIMP is a well-developed, widely used, nonradiating boundary layer prediction technique which has, as alternate options, the mixing length models of Kendall, et al., (Reference 2-6),

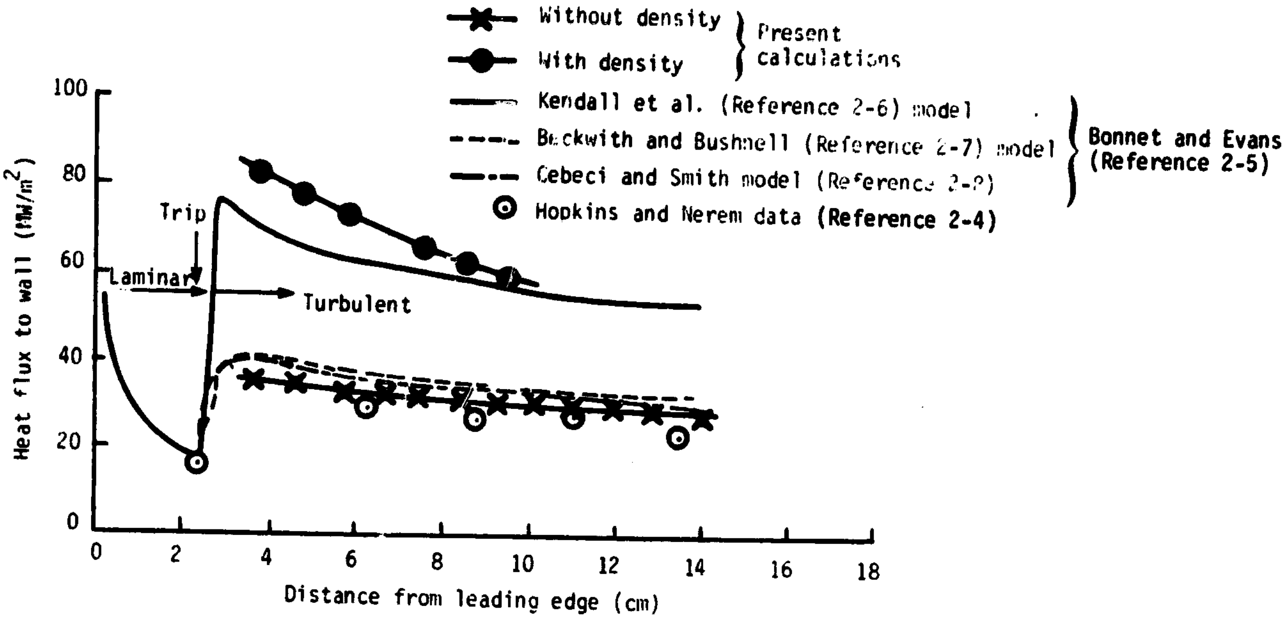

Figure 2-2. Comparison of Heat Transfer Predictions with the Data of Hopkins and Nerem (Reference 2-4)

Beckwith and Bushnell (Reference 2-7), and Cebeci and Smith (Reference 2-8). It is immediately evident that the turbulent models with density (the Kendall and the present model), significantly overpredict highly cooled wall boundary layer heat transfer. The other models show much better agreement with the level and the trend of the data. This comparison indicates that the incompressible mixing length expression is preferable for applications involving highly cooled walls. Therefore, it is employed in the present study.

A second set of predictions was obtained for comparison with the turbulent boundary layer data taken by Hartunian, et al. (Reference 2-9), behind a moving shock wave, which was analyzed by Mirels (Reference 2-10) using an approximate theory. Figure 2-3 shows that the present predictions, the approximate analysis, and the data are all in excellent agreement.

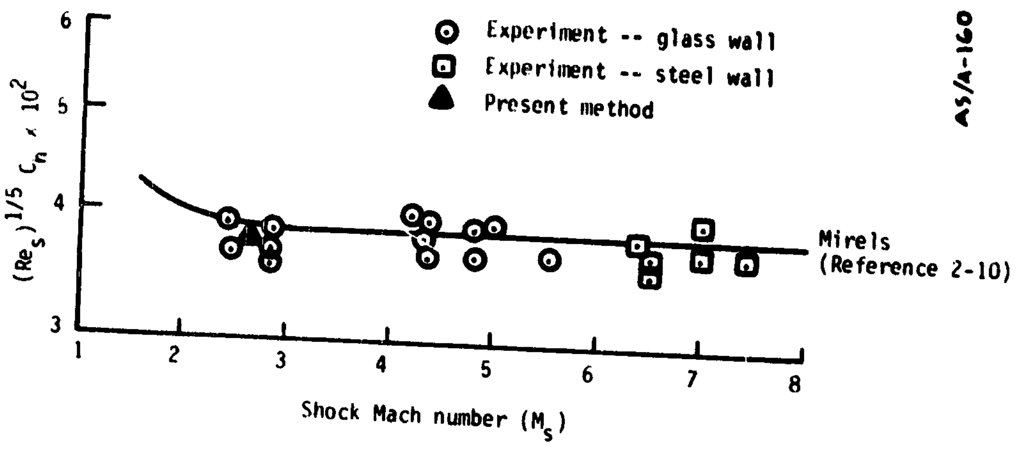

Figure 2-3. Comparison of Predictions with Data of Hartunian et al. (Reference 2-9) for Turbulent Heat Transfer in Air

A third set of predictions was obtained for comparison with the turbulent boundary layer data taken by Martin (Reference 2-11) behind a moving shock wave. Comparisons with directly measured quantities such as temperature profiles were satisfactory; comparison with quantities derived by the experimenter (velocity profiles and momentum thickness) were only fair, but are within the uncertainties introduced in reducing and interpreting the data.

2.2 FLOWFIELDS ABOUT PLANETARY PROBES

Current candidate probe shape for the Jovian entry mission is a spherically tipped 45 degree half angle cone. The important probe configuration and flight parameters are listed in Table 2-1, and flight conditions through the hypersonic heating pulse are presented in Table 2-2

Table 2-1. Probe Configuration and Entry Parameters

Parameter	Value
Probe Configuration (spherically blunted conical forebody)	
Half cone angle (degree)	45
Base radius (m)	0.3112
Bluntness ratio	2
Probe mass (kg)	242
Drag coefficient	1.094
Ballistic coefficient (kg/m^2)	181.82
Atmospheric Model (by Orton)	
H_2/He percentage (volume)	89/11
Entry Parameters	
Inertial entry velocity (km/s)	60
Inertial entry angle (degree)	-9
Entry altitude (km)	1000
Entry latitude (degree)	-6.4
Aximuth angle of inertial velocity vector (degree)	72.5

for entries into the Orton nominal atmosphere. Moss (Reference 2-3) has obtained solutions at some entry conditions (designated by asterisks). Benchmark solutions are unavailable at any of the remaining flight conditions prior to the present study.

A few initial solutions were obtained to assess the number of iterations required to converge on the body shape. The Falanga and Olstad (Reference 2-12) correlation with a slight smoothing in the corner region is used to estimate the initial shock shape. A comparison between the predicted and actual body shapes is shown in Figure 2-4 for flight conditions corresponding to 109 sec after entry. The predictions were obtained on the first iteration and compare quite well with the actual body shape. Predicted and actual body shapes were also compared for two

Table 2-2. Freestream Conditions

Time (s)	Velocity (km/s)	Density (kg/m^3)
99.9	48.07	2.651×10^{-5}
103.9	46.96	7.188×10^{-5}
107.2	44.83	1.635×10^{-4}
109.	42.88	2.546×10^{-4}
110.2*	41.16	3.375×10^{-4}
111.3*	39.29	4.364×10^{-4}
112.2*	37.52	5.340×10^{-4}
113.5*	34.67	7.017×10^{-4}
114.2*	33.01	8.053×10^{-4}
115.3*	30.31	9.892×10^{-4}
116.4	27.54	1.203×10^{-3}
117.4	25.07	1.414×10^{-3}

*HYVIS (Moss, Reference 2-3) solutions are available

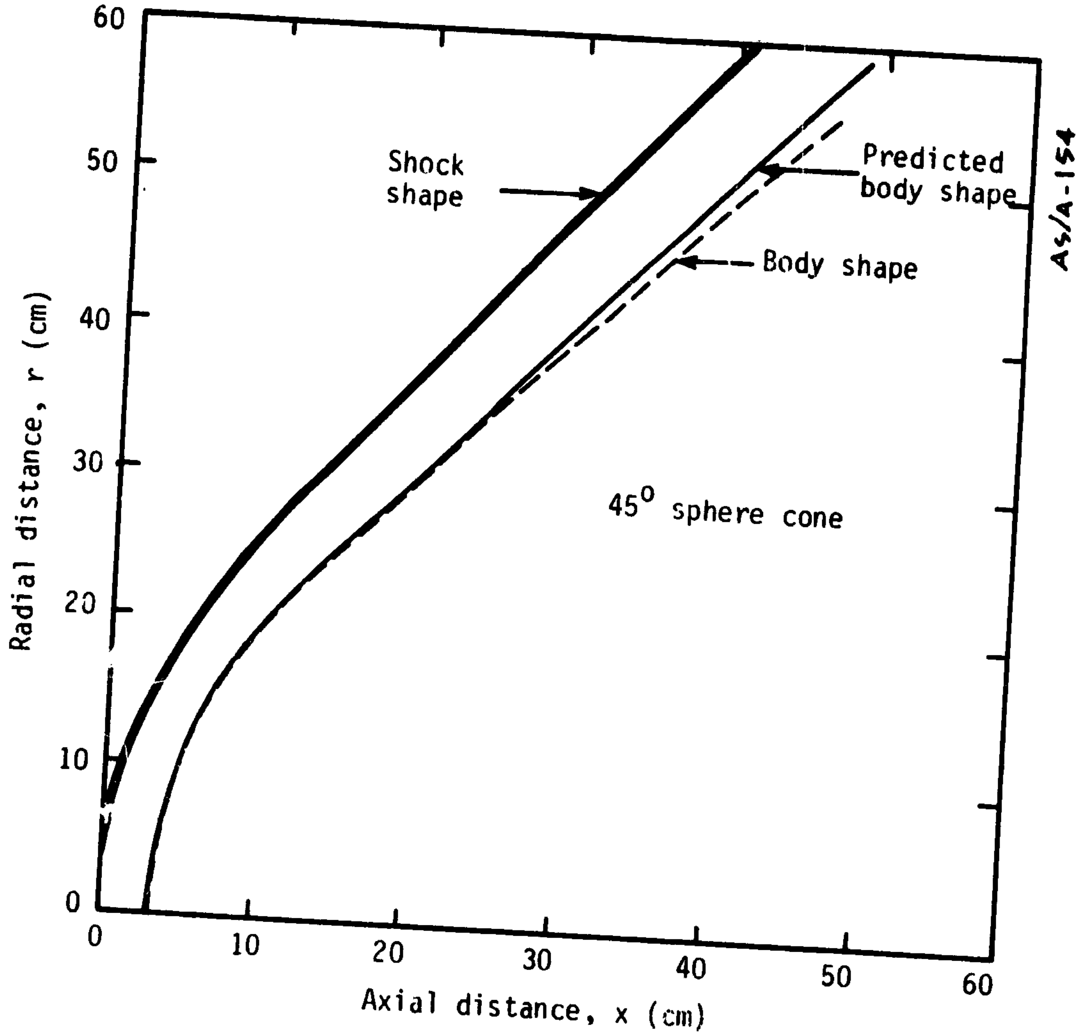

Figure 2-4. Comparison Between Predicted and Actual Shapes (t = 109 sec)

other flight conditions. In both cases, only one iteration was required, since both predictions showed good agreement with actual shapes.

Unblown solutions were obtained at 111.3 sec for comparison with the peak heating solutions of Moss (Reference 2-3). The radiative heating rates to the wall, presented in Figure 2-5, shows that agreement is excellent far back on the flank, and fair in the nose and overexpansion areas. The difference in the stagnation region is due to the pressure gradients employed in the calculation. The present methodology uses a shock front radius of curvature, whereas Moss (Reference 2-3) uses the body radius of curvature. According to the thin shock layer approximation basic to both prediction procedures, the two radii of curvature are identical. In reality, the shock radius of curvatures is somewhat larger, making the body in the present procedure appear to have a larger nose than it does in the Moss (Reference 2-3) procedure.

Solutions were also obtained at 111.3 sec with blowing and assuming a steady-state surface energy balance. The radiative heating rates at the wall are presented in Figure 2-6. The unblown heating rates replotted on this figure confirm a major finding attributed to Moss (Reference 2-3): the blown radiative heating rates overtake and surpass the unblown radiative heating rates back on the cone. This effect is not yet understood, but it is clearly associated with the turbulence in the flow. It updates and modifies important lessons learned from earlier laminar stagnation and off-stagnation point solutions.

Additional blown solutions obtained at 111.3 sec are presented in Figure 2-7 for the flank region of the body. One set of predictions presented in the figure shows the effect on the radiative heating rates of

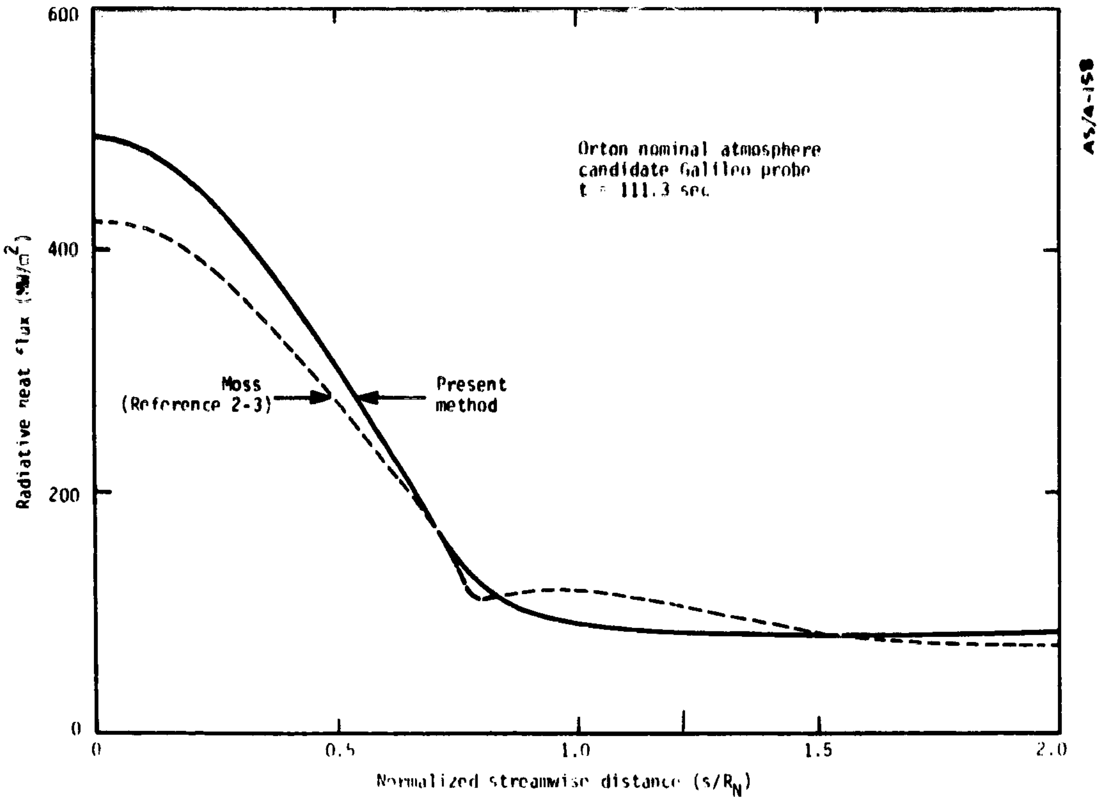

Figure 2-5. Comparisons with Moss (Reference 2-3) for Unblown Turbulent Flows

varying the normalized wake mixing length ($\tilde{\ell}_0$) at the first space station after transition.* The radiative heating rates on the probe flank are fortunately not very sensitive to changes in this parameter. The present solutions are also compared with one obtained by Moss (Reference 2-3) in the figure. Agreement is reasonably good in both level and trends.

---

*The initial value of the normalized wake mixing length ($\tilde{\ell}_0$) is a free parameter in the solution procedure. Its value sets the virtual origin of the turbulence. A baseline value of $\tilde{\ell}_0$ = 2 as obtained from a local wake law, Equation (2-32) of Reference 2-2.

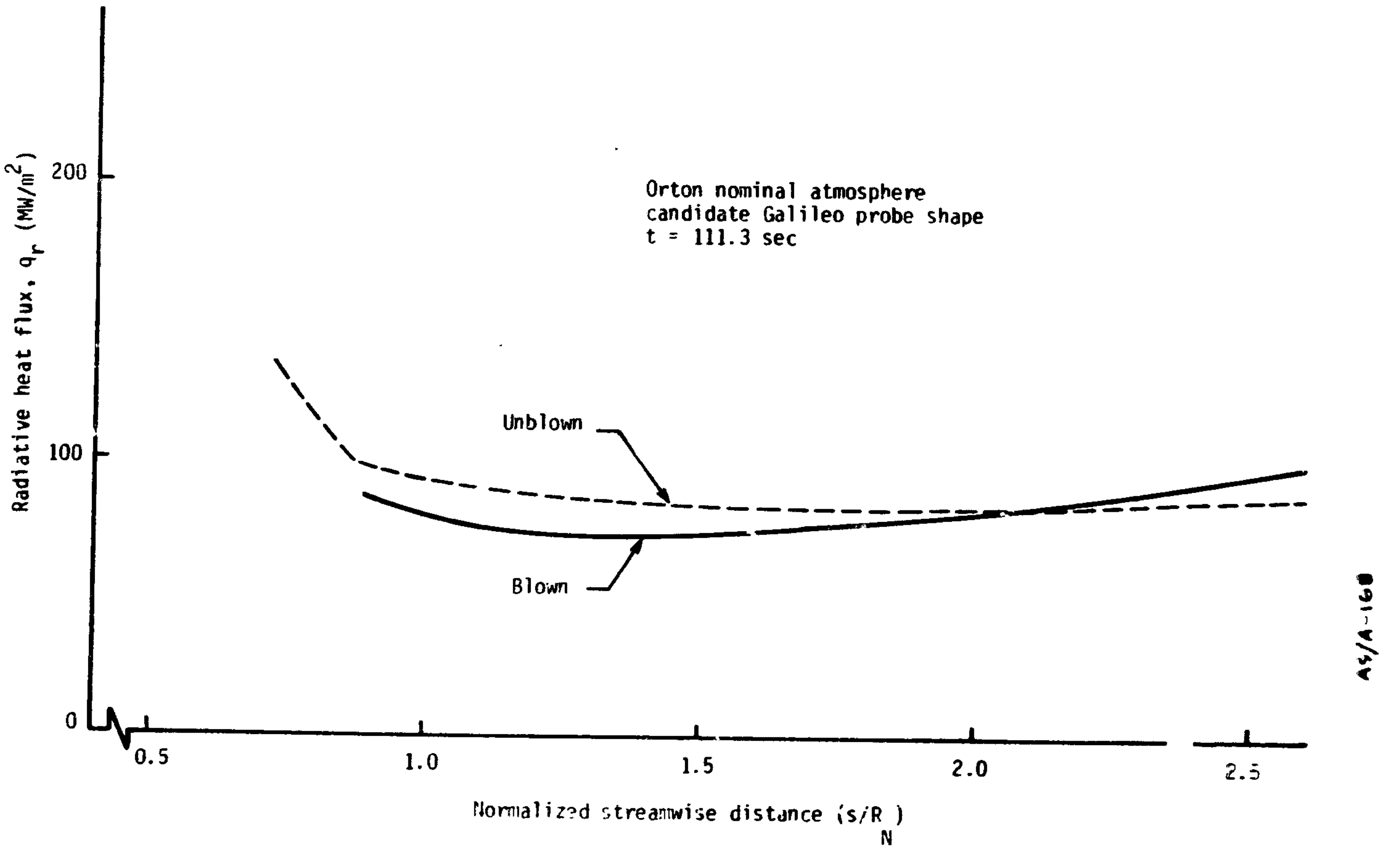

Figure 2-6. Present Predictions Showing Effects of Blowing on Probe Flank

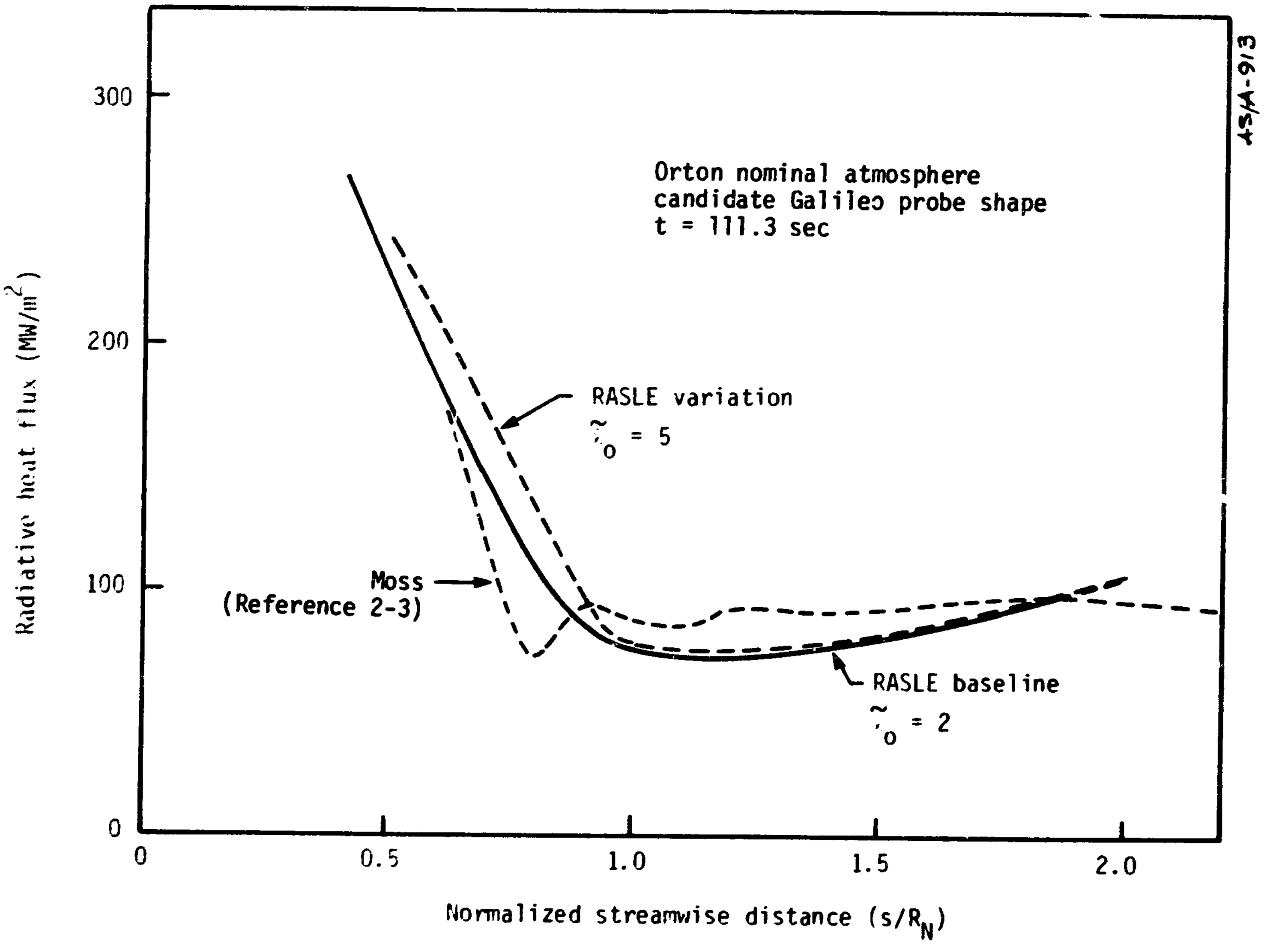

Figure 2-7. Blown, Turbulent Flows on the Flank

Normalized velocity and enthalpy profiles are presented in Figures 2-8 and 2-9, respectively. Comparison between the present predictions and those of Moss (Reference 2-3) show important differences all across the shock layer. Moss' solutions show significantly smaller gradients in the near wall ($y/\delta < .4$) region which can be partially attributed to differences in the blowing rates; his are about 15 percent higher than those in the present study. However, this is not likely to account for a significant fraction of all the differences observed. Apparently, the eddy viscosities predicted in the wall-law region differ significantly. Differences existing in the outer region of the shock layer, as seen in Figure 2-8, were expected, and were attributed to turbulent eddies in this region by the present model and to laminar flow in this region by Moss' (Reference 2-3) model.

The heating rates at the $s/R_N = 2.61$ station on the flank at 111.3 sec (corresponding to profiles presented in Figures 2-8 and 2-9) are:

Heating Rate	Present Study	Moss
Convective	12.7 MW/m^2	13.07 MW/m^2
Radiative	74.6 MW/m^2	80.09 MW/m^2

Agreement is good relative to the needs of the heatshield designer. However, this agreement is surprisingly good when taking into account the considerable differences between the two models and between the predicted profiles. It must be concluded that the heating rates to the wall (especially the dominant radiative component) are not sensitive functions of the flowfield profile details.

It is also interesting to compare the normalized enthalpy profile to the normalized velocity profile for each of the predictive approaches. Agreement is excellent, making Reynolds' analogy an excellent approximation for such flows.

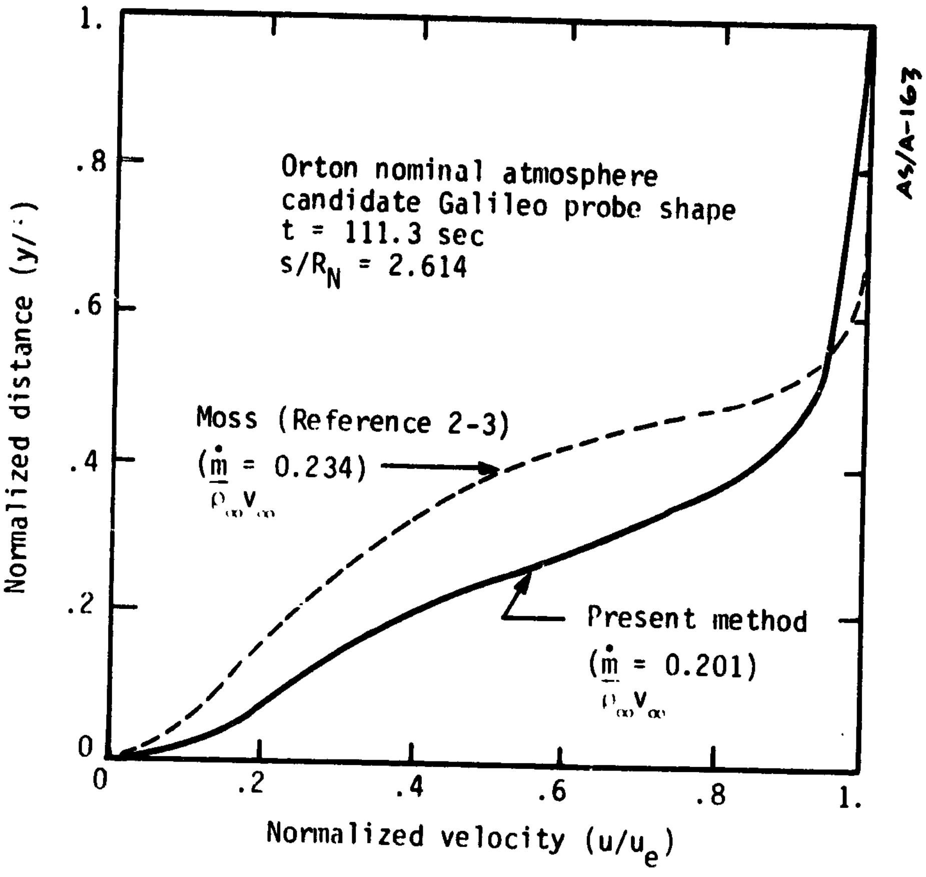

Figure 2-8. Velocity Profiles for Turbulent Flows With Steady-State Blowing

Solutions were also obtained at the early flight conditions where results were unavailable prior to the present study. The convective heating rates are presented in Figure 2-10, and the radiative heating rates are given in Figure 2-11. When generating these solutions, transition was assumed to occur at the first space station off the stagnation point. Interestingly, the maximum radiative and total heating rates are seen occurring in between the stagnation point and the corner. This indicates reattachment and the destruction of the ablation layer shielding the wall from the shock layer radiation in the immediate region of the stagnation point.

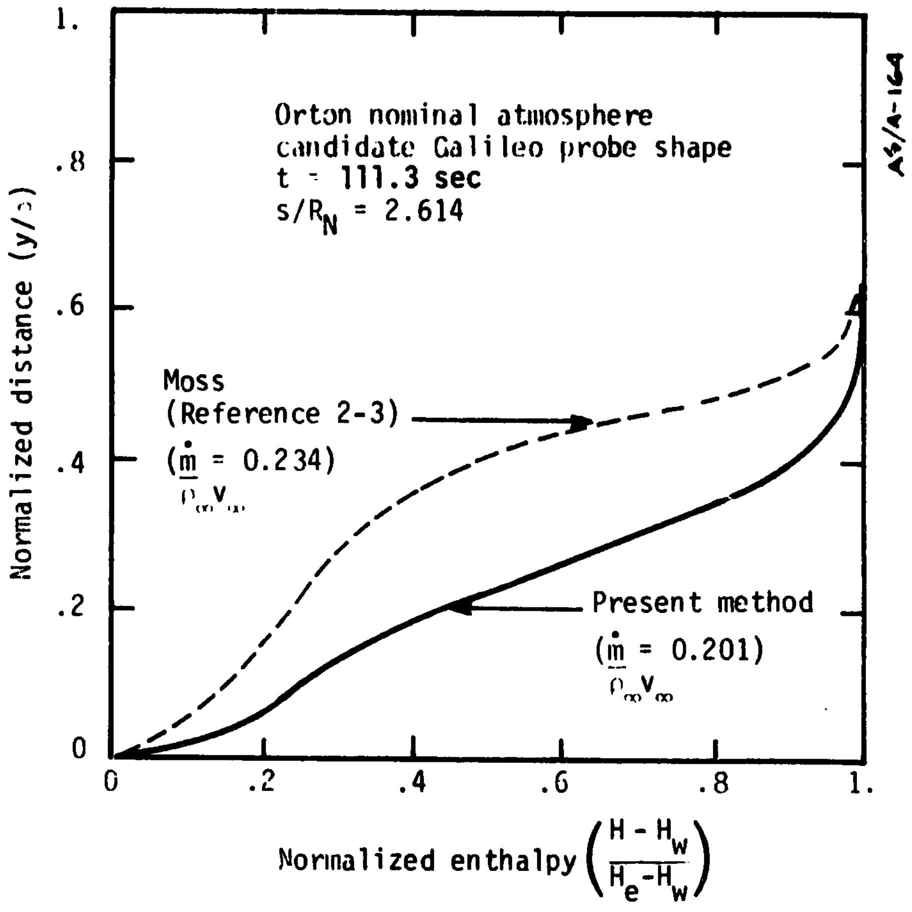

Figure 2-9. Enthalpy Profiles for Turbulent Flows With Steady-State Blowing

2.3 CONCLUDING REMARKS

On the basis of the present study, the following conclusions were reached relative to the prediction of off-stagnation point flowfields, the comparison with laboratory data, and the aerothermal environments for Jovian entry:

- A previously developed prediction procedure (Reference 2-1) can be upgraded to include nonsimilar terms, a turbulent model and a matching procedure for obtaining solutions about the body

- A reasonable turbulent model can be postulated which draws heavily from experience with free-mixing layers, jets and wakes
- The use of the Falanga and Olstad (Reference 2-12) shock shape correlation allows satisfactory solutions to be obtained in only one iteration
- The predictions compare well with the laboratory experiments of Hopkins and Nerem (Reference 2-4), Hartunian, et al. (Reference 2-9), Martin (Reference 2-11), and with the approximate theory of Mirels (Reference 2-10)
- Fair agreement was obtained with the quantities Martin (Reference 2-11) derived from his data
- Satisfactory comparison with the wall heating rates of Moss (Reference 2-3) for both blown and unblown flows
- The present predictions confirmed Moss' (Reference 2-3) finding of an anamolous effect of blowing on the probe flank
- Qualitative but not quantitative agreement was found with the flowfield profiles of Moss (Reference 2-3)
- Early time solutions for wall heating rates were obtained and presented
- Peak heating was observed to occur at off-stagnation location near the reattachment point where the ablation product layer breaks up

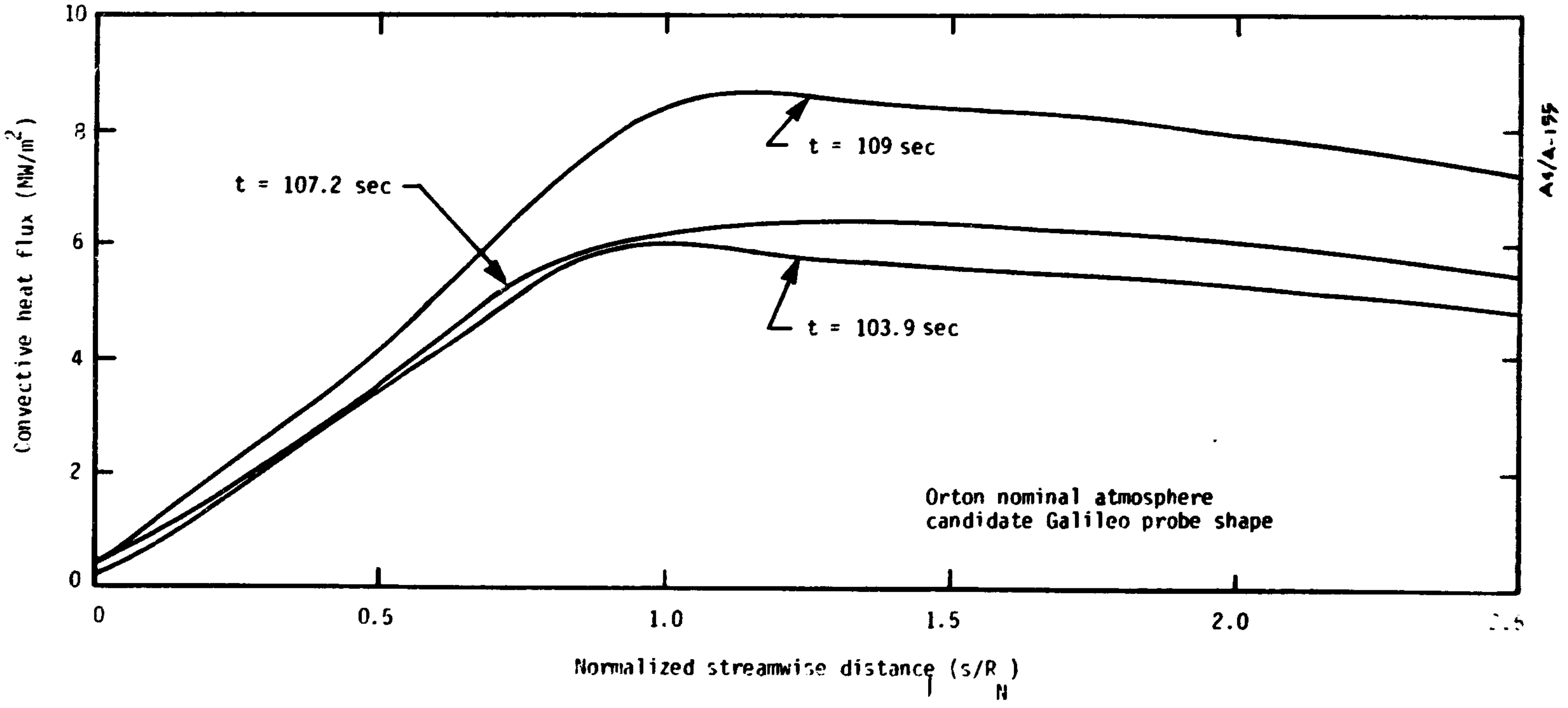

Figure 2-10. Blown Convective Heat Flux Distribution Around the Body for Early Entry Times

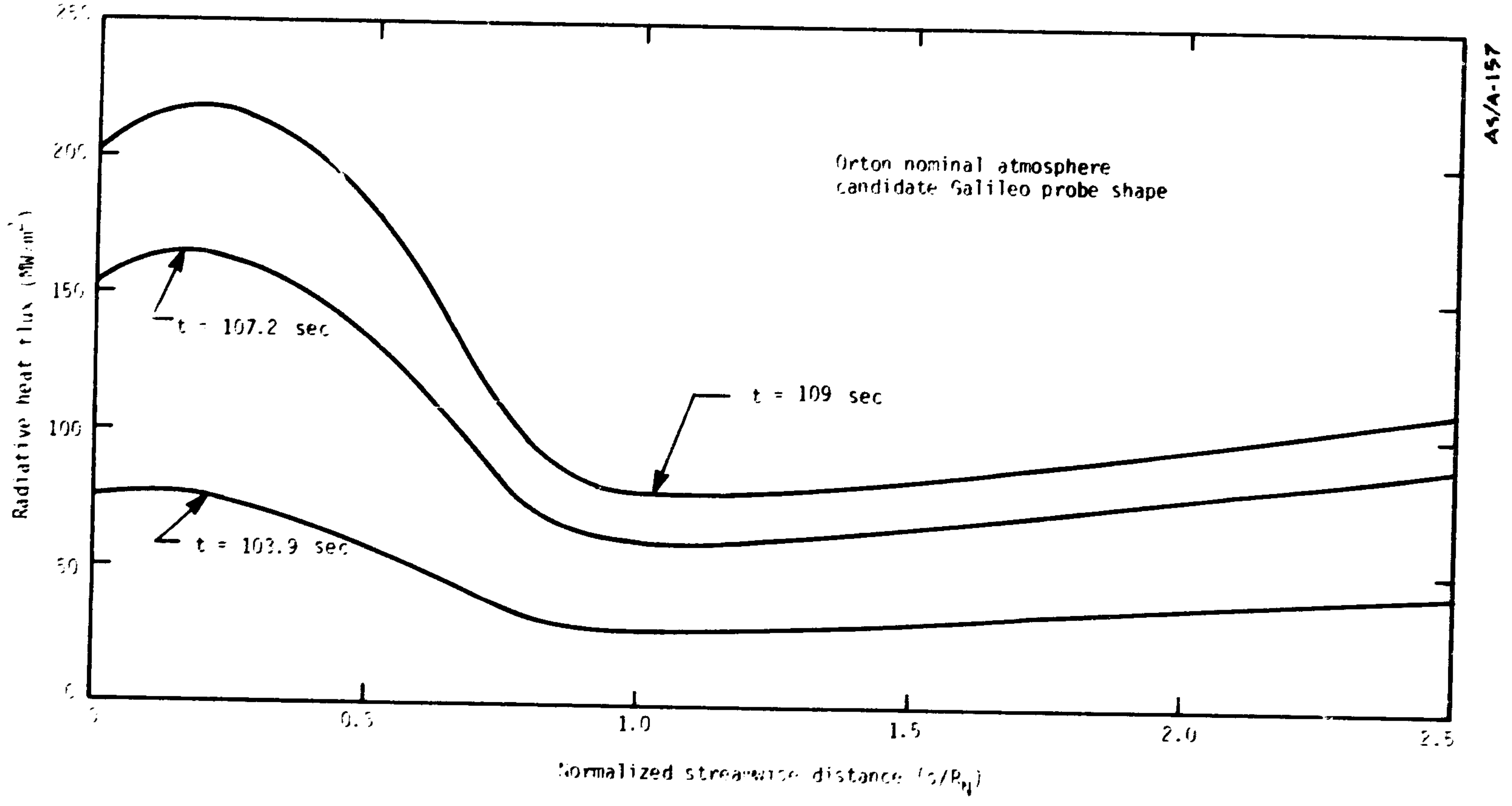

Figure 2-11. Streamwise Distribution of Blown Radiative Heat Flux at Early Entry Times

2.4 REFERENCES

2-1. Nicolet, W. E., Waterland, L. R. and Kendall, R. M., "Methods for Predicting Radiation-Coupled Flowfields about Planetary Entry Probes," AIAA Progress in Astronautics and Aeronautics: Aerodynamic Heating and Thermal Protection Systems, Vol. 59, edited by L. S. Fletcher, published by AIAA, New York, N. Y., pp. 120-136, 1978.

2-2. Nicolet, W. E., and Balakrishnan, A., "RASLE User's Manual," UM-79-10/AS, Acurex Corporation/Aerospace Systems Division, Mountain View, California, July 1979.

2-3. Moss, J. N., "A Study of the Aerothermal Entry Environment for the Galileo Probe," AIAA Paper No. 79-1081, presented at Orlando, Florida, June 4-6 1979.

2-4. Hopkins, R. A., and Nerem, R. M., "An Experimental Investigation of Heat Transfer from a Highly Cooled Turbulent Boundary Layer," AIAA Journal, Vol. 6, No. 10, p. 1912, October 1968.

2-5. Bonnett, W. S., and Evans, R. M., "Boundary Layer Integral Matrix Procedures; Verification of Models," NASA-CR-150271, April 1977.

2-6. Kendall, R. M., Anderson, L. W., and Angier, R. H., "Nonsimilar Solution for Laminar and Turbulent Boundary Layer Flows Over Ablating Surface," AIAA Journal, Vol. 10, No. 9, September 1972.

2-7. Beckwith, I. E., and Bushnell, D. M., "Calculation by a Finite-Difference Method of Supersonic Turbulent Boundary Layers with Tangential Slot Injection," NASA TN-D-6221, April 1971.

2-8. Cebci, T., and Smith, A. M. O., Analysis of Turbulent Boundary Layers, Academic Press, New York, 1974.

2-9. Hartunian, R. A., Russo, A. L., and Marrone, P. V., "Boundary Layer Transition and Heat Transfer in Shock Tubes," J. Aerospace Sci., Vol. 17, p. 587, 1960.

2-10. Mirels, H., "Attenuation in a Shock Tube Due to Unsteady-Boundary-Layer Action," NACA TN 3278, 1968.

2-11. Martin, W. A., "An Experimental Study of the Turbulent Boundary Layer Behind the Initial Shock Wave in a Shock Tube," J. Aerospace Sci., Vol. 25, No. 10, p. 644, October 1958.

2-12. Falanga, R. A., and Olstad, W. B., "An Approximate Inviscid Radiation Flowfield Analysis for Sphere Cone Venusian Entry Vehicles," AIAA Paper No. 74-758, presented at the AIAA/ASME 1974 Thermophysics and Heat Transfer Conference, Boston, Mass., July 15-17 1974.

SECTION 3

ENTROPY LAYER EFFECTS ON GALILEO PROBE CONVECTIVE HEATING ENVIRONMENT

As discussed in Section 1, the heating environment is the primary factor affecting the weight of the heatshield. Predictions of the heating environment must consider several parameters including the atmospheric composition of the planet, the probe configuration, entry angle, entry velocity, and the probe shape change effects.

The radiative and convective heating rates to the probe surface can be determined either by the HYVIS code (Reference 3-1) or by the RASLE code (Reference 3-2). These two available numerical procedures solve the boundary layer form of the Navier-Stokes equations which consider radiation, turbulence, and massive blowing. These two numerical procedures are of the benchmark type; they require ~ 4 to 5 min of computer time for each solution and are expensive to use for parametric design studies. Moreover, these two codes require careful attention in setting up each computer run. These factors led to the development of approximate methods which are computationally faster to obtain solutions.

For Galileo probe heatshield design parametric studies, the three widely used computer codes are the Aerotherm developed Trajectory-Heating Environment Techniques/Analysis (THETA) (Reference 3-3), General Electric Company developed Thermodynamic Outer Planet Insulation Code (TOPIC)

(Reference 3-4), and NASA-Ames Research center developed Coupled Entry Code (Reference 3-5). These design tools use approximate governing equations and/or correlations to estimate the radiative and convective heating rates. Like most of the approximate methods, the codes are not accurate. For example, the effects of flowfield gradients caused by the bow shock curvature on the radiative and convective heat transfer are neglected in these codes. The entropy layer is important under certain flowfield conditions. Entropy layer effects are thought to be small for large half-cone angled planetary entry probes and are, therefore, usually neglected. However, the candidate Galileo probe is a sphere cone configuration with the half-cone angle being set at 45 degrees.

The objective of this task is to determine, from basic governing equations, the effect of entropy layer on the probe heating environment. Only the convective heating history will be considered on this task. The following subsections present a brief summary of previous research in this area, the basic governing equations, solution procedure, and results obtained for a 45 degree sphere-cone shaped probe entering the nominal model (Orton) Jupiter atmosphere.

3.1 BACKGROUND

Entropy layer or the vortical layer develops on blunt bodies at hypersonic flow conditions due to the bow shock curvature. Neighboring streamlines in a vortical layer pass through a varying shock wave angle and attain different entropy levels. For the same static pressure, lower shock angle corresponds to lower entropy and higher velocity in the shock layer. As the higher velocity streamlines are swallowed by the growing boundary layer, the kinetic energy in the boundary layer and the heat transfer to the surface are increased; this increase in heat transfer may be significant.

The influence of entropy layer on heat transfer rates has been considered by the earth reentry vehicle design community. For analyzing nosetip ablation response, particularly for a RV, only convective heating rate is important. Ferri (Reference 3-6) presented approximate methods of heat transfer that included entropy gradient effects for the case of laminar boundary layer. Experimental results indicated that entropy layer effects are large and important. Rubin (Reference 3-7) presented a simple graphical approach to determine the variation of the flow conditions at the outer edge of a laminar boundary layer over blunted cone resulting from entropy gradients. His results indicated a significant increase in convective heating over levels computed on the basis of flow eminating through a normal shock. Edquist (Reference 3-8) extended Rubin's work to turbulent boundary layers and found that entropy effects increase the turbulent heat transfer rates by factors of 2 to 3.

Recently, Dahm, et al. (Reference 3-9) developed a momentum/energy integral technique (MEIT), which starts with and retains the exact boundary layer equations. The effects of wall blowing, acceleration, curved shock, and boundary layer properties are properly accounted for via the use of influence coefficients. These influence coefficients are included in the formulation of both the local Stanton number and friction coefficient.

A detailed development of the governing equations, solution procedure, and validation of MEIT methodology are described in Reference 3-9. Only a summary of the equations and a brief discussion of the solution technique are presented here.

3.2 GOVERNING EQUATIONS

The boundary layer momentum and energy integral equations are

$$\frac{1}{r}\frac{d}{ds}\, r\rho_e u_e^2 \;\; = \tau_w + (\rho v)_w u_{i,w} + H\theta\, \frac{dp}{ds} \tag{3-1}$$

and

$$\frac{1}{r}\frac{d}{ds}\, r\rho_e u_e (h_{t,e} - h_w)\, \phi = \dot{q}_w + (\rho v)_w\, (h_{t,i,w} - h_w) \tag{3-2}$$

The various quantities that appear in the above integral equations are defined below:

momentum thickness θ:

$$\theta = \int_0^\infty \frac{\rho u}{\rho_e u_e}\, \frac{u_i - u}{u_e}\, dy \tag{3-3}$$

energy thickness ϕ:

$$\phi = \int_0^\infty \frac{\rho u}{\rho_e u_e}\, \frac{h_{t,i} - h_t}{h_{t,e} - h_w}\, dy \tag{3-4}$$

boundary layer shape factor:

$$H = \delta^*/\theta \tag{3-5}$$

displacement thickness δ^*:

$$\delta^* = \int_0^\infty \left(1 - \frac{\rho u}{\rho_i u_e}\right) dy \tag{3-6}$$

In the above equations, the subscript e refers to the properties evaluated at the boundary layer edge; the subscript i refers to inviscid properties. The quantity $u_{i,w}$ is the inviscid velocity at the wall. The terms $h_{t,i}$ and $H_{t,e}$ refer to local and edge inviscid stagnation enthalpies respectively. For nonvortical inviscid boundary layer flows, $u_i = u_e$, $h_{t,i} = h_{t,e}$ is used for all streamlines; the above equations reduce to standard integral equations.

To solve the integral equations, the properties at the edge of the boundary layer are needed. The definition of boundary layer edge, particularly for vortical inviscid flows, is not straightforward. Usually, the boundary layer edge is defined as the location in the boundary layer where the local velocity is equal to 0.99 times the local inviscid velocity. Though this criterion is not fully satisfactory, Dahm, et al., recommended this criterion as reasonable, and this criterion is used in the present calculations.

The edge properties needed are obtained with the use of the entrainment relation. The entrainment relation can be formulated by performing a mass balance on the flow, i.e.,

$$\rho_\infty u_\infty (\pi \bar{y}^2) = 2\pi r \int_0^\delta \rho u dy - 2\pi \int_0^\infty (\rho v)_w r ds \tag{3-7}$$

where y determines the shock angle through which the boundary layer edge streamline has passed. The entropy behind the shock is shock angle dependent, as are the properties at the edge of the boundary layer.

Equation (3-7) can be rewritten as

$$\rho_\infty u_\infty \bar{y}^2 = 2rF\mu_e Re_\theta - 2 \int_0^s (\rho v)_w r ds \tag{3-8}$$

where

$$F = \frac{\delta - \delta_e^*}{\theta} \tag{3-9}$$

$$\delta_e^* = \int_0^\delta \left(1 - \frac{\rho u}{\rho_e u_e}\right) dy \tag{3-10}$$

$$Re_\theta = \frac{\rho_e u_e}{\mu_e} \qquad (3\text{-}11)$$

The wall shear stress and the heat transfer coefficient appearing in Equations (3-1) and (3-2) are related to friction coefficient and Stanton number, i.e.,

$$\tau_w = \frac{1}{2} \rho_e u_e^2 C_f \qquad (3\text{-}12)$$

$$\dot{q}_w = \rho_e u_e C_H (h_r - h_w) \qquad (3\text{-}13)$$

where h_r, the recovery enthalpy is given by

$$h_r = h_e + R \frac{u_e^2}{2} \qquad (3\text{-}14)$$

where R is the recovery factory.

The auxiliary relations needed to solve the integral equations are given below:

<u>Laminar flow</u>:

$$\frac{C_{f,\ell,o}}{2} = \frac{0.245}{Re_\theta} \qquad (3\text{-}15)$$

$$C_{h,\ell,o} = 0.22/Pr^{4/3} Re_\phi \qquad (3\text{-}16)$$

$$H_\ell = 3.029 \frac{T_w}{T_e} - 0.0614 \qquad (3\text{-}17)$$

$$F_\ell = 1.521 + 4.388\left(\frac{T_w}{T_e} + 0.0378\right)^{1/2} \qquad (3\text{-}18)$$

$$R_\ell = Pr^{1/2} \qquad (3\text{-}19)$$

Turbulent Flow:

$$C_{f,t,o} = \frac{0.245}{Re_\theta} + \frac{0.0123\ Re_\theta}{100 + Re_\theta}\left(\log_{10} Re_\theta\right)^{-1.6} \qquad (3\text{-}20)$$

$$C_{h,t,o} = \frac{0.22}{Pr^{4/3}\ Re_\phi} + \frac{0.0123\ Re_\phi}{Pr^{1/2}(100 + Re_\phi)}\left(\log_{10} Re_\phi\right)^{-1.6} \qquad (3\text{-}21)$$

$$H_t = 2.285(1 + 3.2\ e^{-n})\ \frac{T_w}{T_e} - 0.96 \qquad (3\text{-}22)$$

$$n = \frac{0.37 + \ell n\ Re_\theta}{2.79 - 0.14\ \ell n\ Re_\theta} \qquad (3\text{-}23)$$

$$F_t = 5.28\ \ell n\left(\frac{T_w}{T_e} + 2.8\right) + (n - 5) \qquad (3\text{-}24)$$

$$R_t = Pr^{1/3} \qquad (3\text{-}25)$$

For planetary entry probes, boundary layer effects such as acceleration, property variation, and vortical layer effects, are important. Since the purpose is to compute the non-blown convective heating rates to the probe surface, the effect of wall blowing is not included in the present calculations. The various effects are accounted for by modifying the Stanton number and friction coefficients given above. The modification is accomplished with the use of influence coefficients.

In general, both the Stanton number and the friction coefficient are written as

$$C_{x,y} = C_{x,y,o} \prod^{z} I_{x,y,z} \qquad (3\text{-}26)$$

where $I_{x,y,z}$ are the influence coefficients. The subscript x corresponds to heat or momentum transfer ($x = h$ or f), and the subscript y corresponds to laminar or turbulent ($y = \ell$ or t) flow, respectively. The subscript z refers to the type of boundary layer effect.

The three phenomena considered and their corresponding z subscripts are:

acceleration - β
property variation - p
vortical layer effects - Ω

The relationship for the influence coefficients for the three phenomena are:

Acceleration -- In laminar flow

$$I_{f,\ell,\beta} = (1 + 3\beta)^{1/3}, \quad \beta > 0 \tag{3-27}$$

$$I_{f,\ell,\beta} = 1.0, \quad \beta < 0 \tag{3-28}$$

$$I_{h,\ell,\beta} = (1 + 4\beta)^{1/6}, \quad \beta > 0 \tag{3-29}$$

$$I_{h,\ell,\beta} = 1.0, \quad \beta < 0 \tag{3-30}$$

where

$$\beta = \frac{2\xi}{U_e} \frac{dU_e}{d\xi} \tag{3-31}$$

and

$$\xi = \int_0^s \rho_e \mu_e U_e r^2 \, ds \qquad (3\text{-}32)$$

For turbulent flow, only the first terms of the appropriate basic turbulent laws are modified by the above influence coefficients.

Property Variation -- To account for property variation, the properties such as density, viscosity, and Prandtl number are evaluated at the reference enthalpy h'

$$h' = ah_e + bh_r + ch_w \qquad (3\text{-}33)$$

Influence coefficients are given by

$$I_{x,y,p} = \left(\frac{\rho'}{\rho_e}\right)^d \left(\frac{\mu'}{\mu_e}\right)^e , \quad \begin{matrix} x = f, h \\ y = \ell, t \end{matrix} \qquad (3\text{-}34)$$

The constants a, b, c, d, and e for various x, y combinations are listed in Table 3-1.

Inviscid Vorticity Effects

Due to lack of data base on which to derive the vorticity influence coefficients, all four of them were set equal to 1.

$$I_{x,y,\Omega} = 1 \text{ for } x = f, h \text{ and } y = \ell, t \qquad (3\text{-}35)$$

The relations given above for H, F, C_f, and C_h are only for fully laminar and for fully turbulent flows. However, the flow may transist to turbulent from laminar conditions. To estimate these four

Table 3-1. Constants Used to Evaluate Property Influence Coefficients

Property Influence Coefficients	Constant				
	a	b	c	d	e
$I_{f,1,p}$	0.23	0.19	0.58	0	0
$I_{h,1,p}$	0.23	0.19	0.58	1	1
$I_{f,t,p}$	0.36	0.19	0.45	1	0.25
$I_{h,t,p}$	0.36	0.19	0.45	1	0.25

parameters for transitional flow, the following relation was recommended in Reference 3-9.

$$P = (1 - f)\,P_{\ell} + f\,P_{t} \tag{3-36}$$

where P is one of the four parameters mentioned above, and f is the intermittency factor. The equation for f is

$$f = 1 - \frac{\left\{Re_{\theta}^{2}\,(C_{f,t} - C_{f,\ell})\right\}_{tr}}{Re_{\theta}^{2}\,(C_{f,t} - C_{f,\ell})} \tag{3-37}$$

where the subscript tr refers to conditions at the transition point.

3.3 SOLUTION PROCEDURE FOR THE BOUNDARY LAYER INTEGRAL EQUATIONS

The solution procedure for the governing integral equations consist of two steps. First, series solutions at and in the vicinity of the stagnation point are obtained. Second, away from the stagnation region, a finite-difference numerical scheme is used to obtain solutions.

Before the start of the solution procedure, the surface shape, pressure, and temperature distribution are to be specified. In addition, from known freestream conditions, the bow shock shape needs to be calculated. Relations which describe environmental gas thermodynamic and transport properties are also needed.

At the stagnation point, limiting solutions to the momentum and energy integral equations are obtained. From Equations (3-1) and (3-2), the limit as s approaches to zero, the momentum thickness is given by

$$\theta_o = \sqrt{\frac{0.245\ \nu_o}{(3 + H) \left.\frac{dU_e}{ds}\right|_o} \prod_i C_{f,\ell,i}} \tag{3-38}$$

and the energy thickness is given by

$$\phi_o = \sqrt{\frac{0.22\ \nu_o}{2\ Pr^{4/3} \left.\frac{dU_e}{ds}\right|_o} \prod_i C_{h,\ell,i}} \tag{3-39}$$

Note that the momentum and energy thicknesses depend on the stagnation point velocity gradient. At the vicinity of the stagnation point, following Reference 3-9, series solutions are obtained, i.e.,

$$\theta = \theta_o\ (1 + a\psi^2) \tag{3-40}$$

$$\phi = \phi_o\ (1 + b\psi^2) \tag{3-41}$$

where ψ is the normalized streamwise distance, i.e.,

$$\psi = s/R_N \tag{3-42}$$

where R_N is the nose radius or reference radius.

The constants given in Equations (3-40) and (3-41) are defined in Reference 3-9. Away from the stagnation point, the following implicit finite-difference scheme is used:

$$F_{x,I} = F_{x,I-1} + \frac{(s_I - s_{I-1})}{2} (F'_{x,I-1} + F'_{x,I}), \text{ for } x = f \text{ or } h \qquad (3\text{-}43)$$

where

$$F_f = r \rho_e u_e^2 \theta \qquad (3\text{-}44)$$

$$F_h = r \rho_e u_e (h_{t,e} - h_w) \phi \qquad (3\text{-}45)$$

$$F'_f = \frac{dF_f}{ds} \qquad (3\text{-}46)$$

$$F'_h = dF_h/ds \qquad (3\text{-}47)$$

and I is integration index along the surface.

The solution scheme is iterative in nature since the $F_{x,I}$ depends on $F'_{x,I}$. At each integration point, convergence is necessary before continuing on to the next point. Convergence criteria used are that changes in both the transfer coefficients are less than 0.1 percent between successive iterations. If the solution procedure fails to converge, it is usually traced to vortical layer effects. Convergence failure arises whenever the shock curvature is large; this leads to large inviscid flow entropy gradients. However, a default procedure is used in the event of nonconvergence. The default procedure is to use a local explicit solution obtained by setting $F'_{x,I} = F'_{x,I-1}$.

3.4 RESULTS AND DISCUSSION

Results obtained with the momentum-energy integral technique outlined in Section 3.3 are presented in this section. Extensive validation of the numerical method was performed and were reported in Reference 3-9. To check the accuracy of this method, convective heating rate at the stagnation point were compared. Table 3-2 presents the assumed probe configuration and entry parameters. For these assumed conditions, the Aerotherm-developed THETA computer code was run to generate the freestream conditions. Table 3-3 shows the freestream conditions as a function of time, and, in addition, the conditions behind the shock and the convective heating rate at the stagnation point are listed, where present calculations are compared with the calculated results of Moss (Reference 3-10).

The results of Moss are obtained with the HYVIS code. The HYVIS code accounts for radiation absorption and emission in the shock layer. The slight discrepancy in the convective heating rate is due to (1) the approximate nature of the MEIT methodology and, (2) coupling in the differnt modes of heat transfer.

Figure 3-1 and 3-2 show the vortical layer effects on convective heat flux distribution for two different freestream conditions. The flow was assumed to be laminar at the stagnation point and up to a streamwise distance of 0.1 R_N. Due to turbulence, heat flux reaches a maximum value and then falls. The vortical layer effect is not felt until a streamwise distance of unit nose radius is reached because the shock is almost normal up to the tangency point. Beyond the tangency point, the curved shock effects are felt, particularly at the flank regions of the candidate probe where an approximate 20 percent increase in the convective heat flux is seen due to the entropy layer.

Table 3-2. Probe Configuration and Entry Parameters

Probe Configuration (spherically blunted conical forebody)	
Half cone angle (degree)	45
Base radius (m)	0.3112
Bluntness ratio	2
Probe mass (kg)	242
Drag coefficient	1.094
Ballistic coefficient (kg/m^2)	181.82
Atmospheric Model (by Orton)	
H_2/He percentage (volume)	89/11
Entry Parameters	
Inertial entry velocity (km/s)	60
Inertial entry angle (degree)	-9
Entry altitude (km)	1000
Entry latitude (degree)	-6.4
Azimuth angle of inertial velocity vector (degree)	72.5

For the candidate probe, no laminar calculations were performed at these entry conditions. Earlier calculations showed that entropy layer effects were small for laminar flow conditions.

Figures 3-1, 3-2, and 3-3 were generated from the MEIT procedure. Two types of calculations were performed: (1) the entropy layer option was activated, and (2) entropy behind the shock were assumed to be constant.

Figure 3-3 shows the curved shock effect on the convective heat flux for the entire trajectory. Freestream conditions, tabulated in Table 3-3, were used. As shown, during the early part of entry and until the peak heating time during the trajectory, the vortical layer effects are significant; an approximate 20 percent increase in convective heatflux due to vortical layer is seen. During the post-peak heating time of the

Table 3-3. Freestream Conditions and Comparison of Stagnation Results

Freestream Conditions					Computed by Moss (Reference 3-10)				Present Calculations			
					Shock Layer Conditions				Shock Layer Conditions			
Time (s)	Altitude (km)	Velocity (km/s)	Density (kg/m^3)	Mach No. (M_∞)	Pressure (atm)	Density Ratio (ρ_s/ρ_∞)	Temp. (^{o}K)	Convective Flux (MW/m^2)	Pressure (atm)	Density Ratio (ρ_s/ρ_∞)	Temp. (^{o}K)	Convective Flux (MW/m^2)
99.9	195.6	48.07	2.65-5	57.21	0.56	13.17	15287	79	0.56	13.45	15858	66.9
103.9	169.6	46.96	7.19-5	56.58	1.44	12.34	16079	114	1.44	12.66	16684	111.1
107.2	149.1	44.83	1.64-4	54.68	2.97	11.60	16411	140	2.97	11.94	16942	145.3
108.2	143.2	43.83	2.10-4	53.58	--	--	--	--	3.63	11.70	16903	155.0
110.2	131.9	41.17	3.38-4	50.30	5.12	10.74	16091	149	5.14	11.11	16425	165.9
111.3	126.1	39.29	4.36-4	47.60	6.01	10.36	15738	147	6.02	10.68	16280	162.5
112.2	121.5	37.52	5.34-4	44.53	6.68	10.00	15326	142	6.70	10.31	15896	157.9
113.5	115.3	34.67	7.02-4	39.55	7.45	9.46	14477	128	7.48	9.84	15036	134.9
115.3	107.6	30.31	9.89-4	37.27	7.95	8.78	12631	100	7.97	9.00	13468	102.3
117.4	100.0	25.07	1.41-3	33.11	7.90	9.94	8102	60	7.78	8.76	10150	62.8

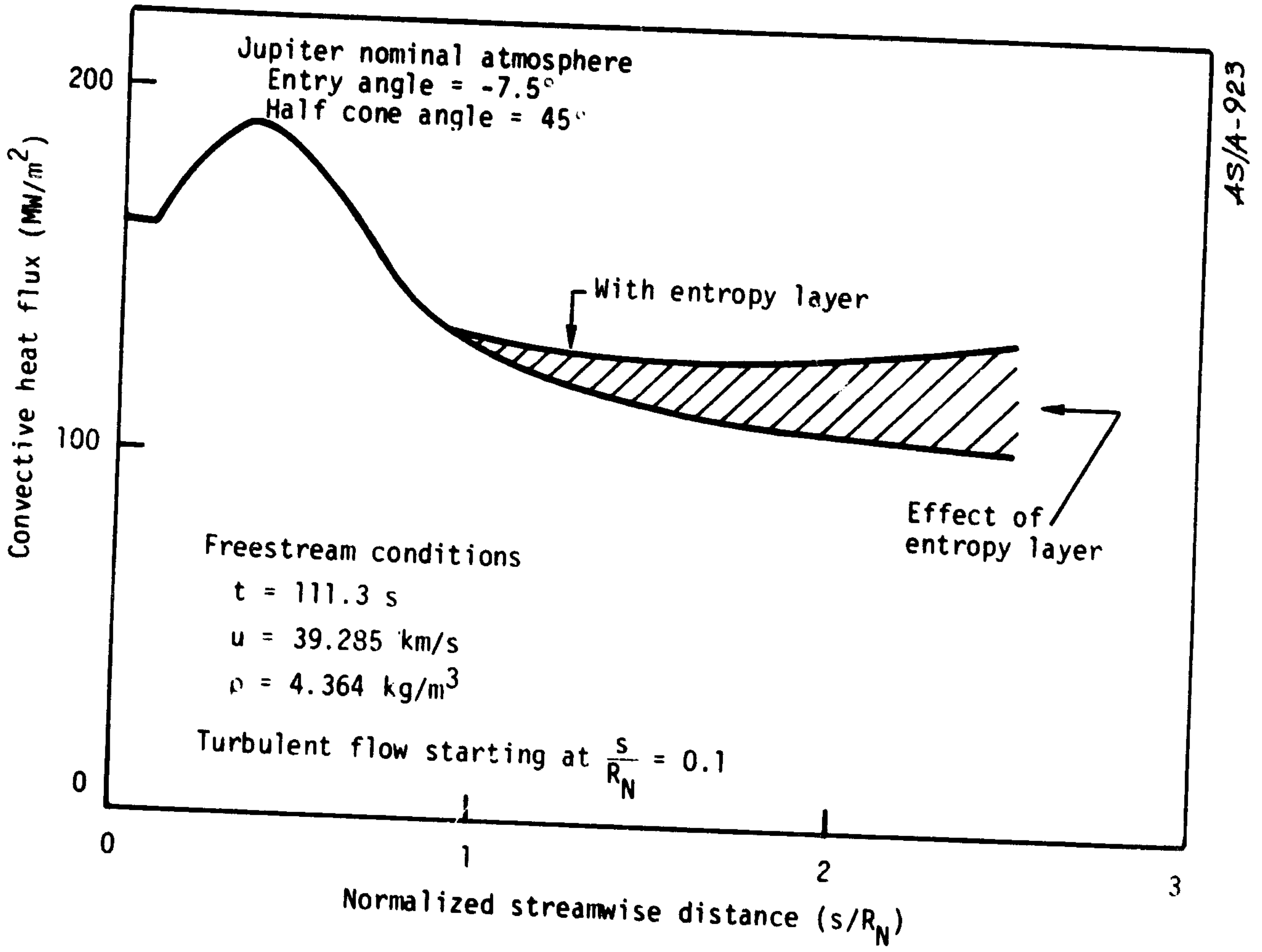

Figure 3-1. Effect of Entropy Layer on Convective Heating Rate at Peak Heating Time During the Trajectory

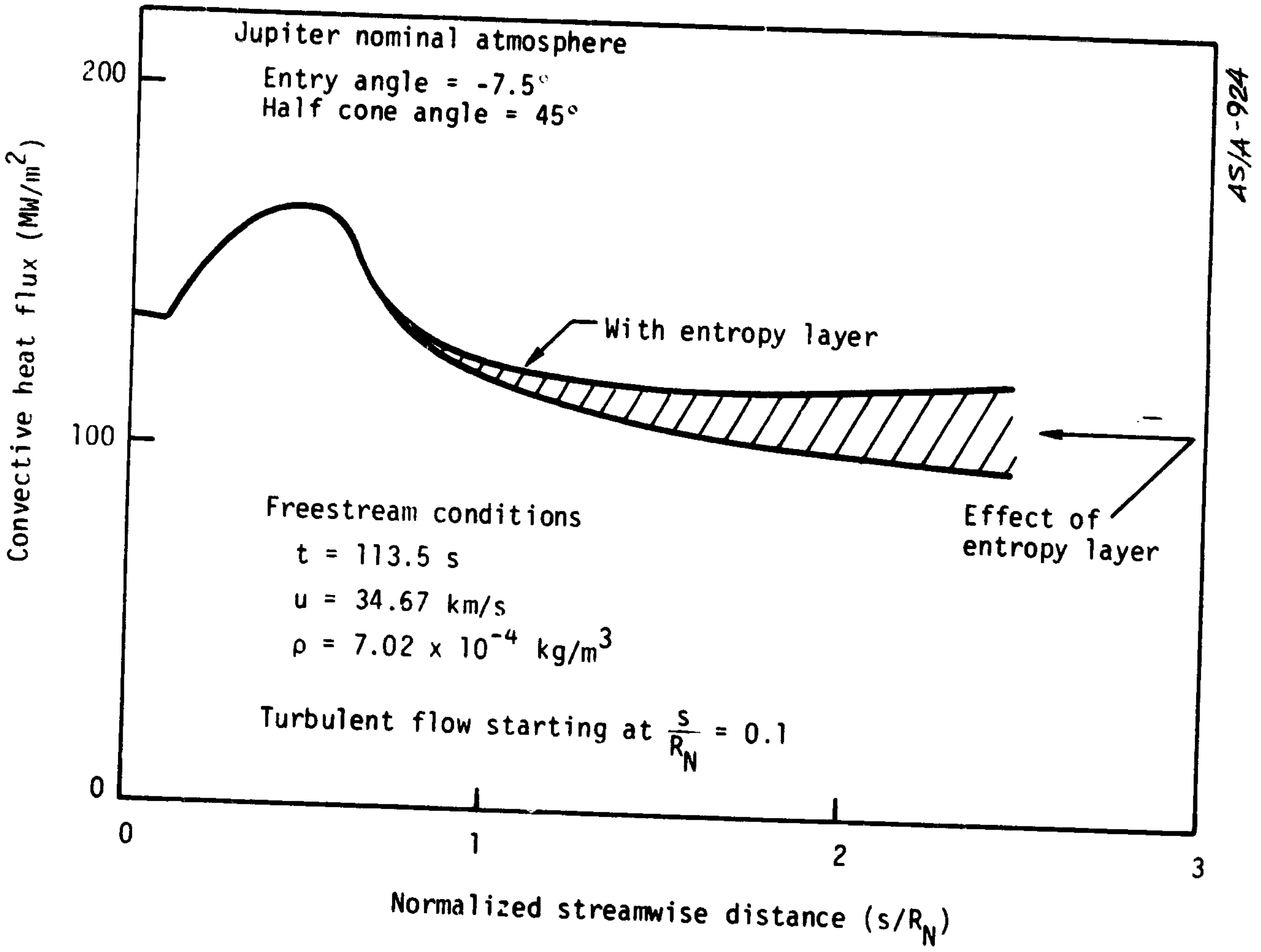

Figure 3-2. Effect of Entropy Layer on Convective Heating Rate at t = 113.5 sec

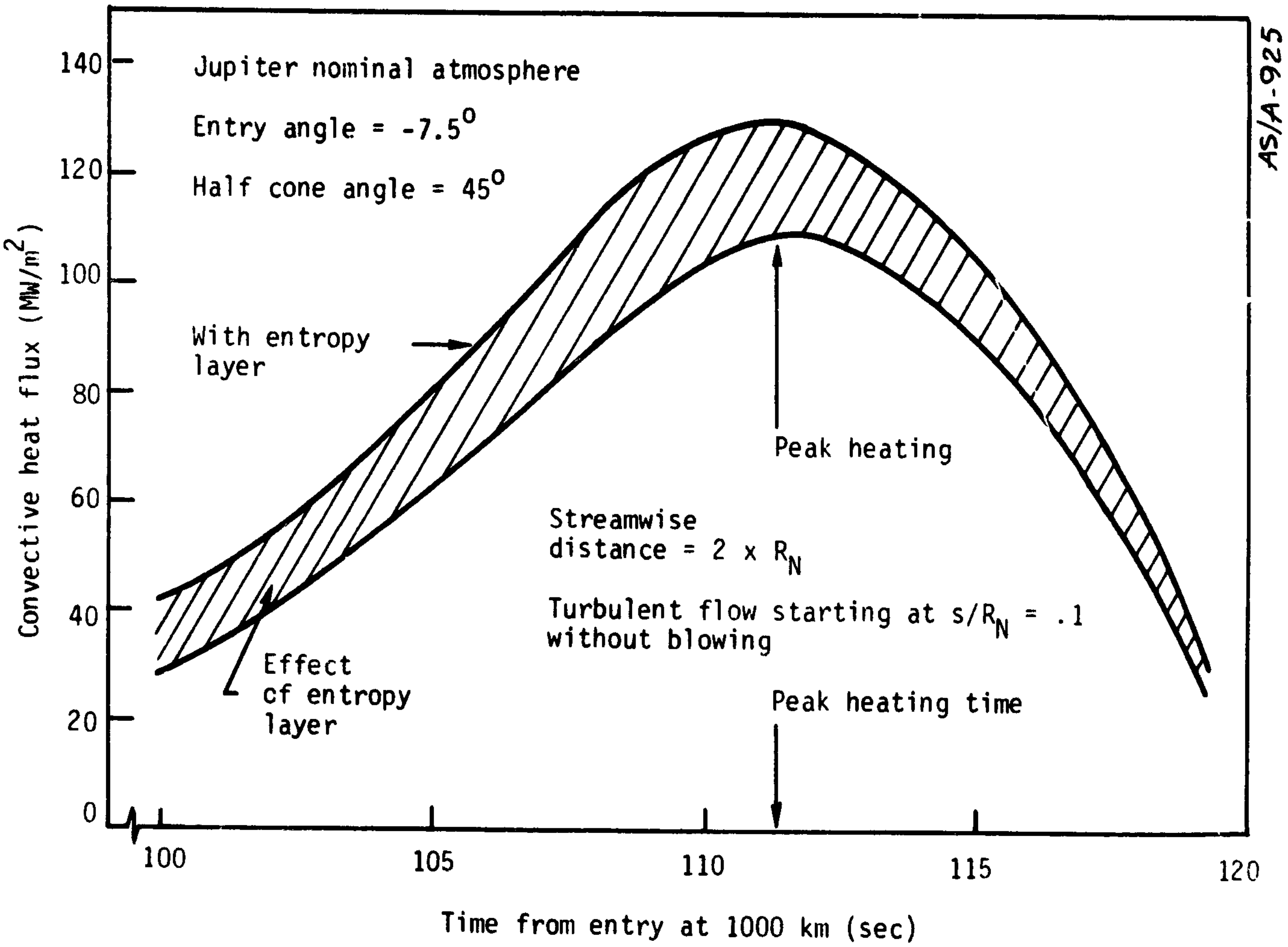

Figure 3-3. Effect of Entropy Layer on Convective Heating Rate for the Complete Jupiter Nominal Entry Trajectory

trajectory, the curved shock effects start to decrease. The reason is that during the pre-peak heating time of the trajectory, the mass entrained in the shock layer increases and reaches a maximum. In addition, during this phase of the entry, the freestream velocity of the probe is high. This increases the kinetic energy in the boundary layer and increases the convective heat flux. During post-peak time of trajectory, the probe has slowed down considerably. This reduces the net increase in the kinetic energy in the boundary layer.

3.5 CONCLUSIONS

For the analysis and calculations performed, the following conclusions are reached:

- Entropy layer effects increase the convective heat flux by as much as 20 percent
- The effects of vortical layer are significant during the pre-peak heating time of trajectory

3.6 REFERENCES

3-1. Moss, J. N., "Reacting Viscous-Shock-Layer-Solutions with Multicomponent Diffusion and Mass Injection," NASA TR-411, 1974.

3-2. Nicolet, W. E., Balakrishnan, A., "RASLE User's Manual," UM-79-10/AS, Acurex Corporation/Aerospace Systems Division, Mountain View, California, July 1979.

3-3. Balakrishnan, A., Laub, B., Chu, E., and Nicolet, W. E., "Outer Planet Probe Thermal Protection: Heating Environments and Spallation Assessment," Acurex Final Report to NASA/Ames Research Center, 1978.

3-4. Brewer, R. A., Brant, D. N., and Fogaroli, R. P., "Development of a Steady-State Shape Change Ablation Code for the Design of Outer Planet Probes," AIAA Paper No. 77-95, 1977.

3-5. Lasher, L. E., Howe, J. T., and Wilson, J. F., "Engineering Approximations for Jovian Entry," AIAA Paper No. 77-767, 1977.

3-6. Ferri, A., "Some Heat Transfer Problems in Hypersonic Flow," Aeronautics and Astronautics, Edited by Hoff, N. J., and Vincenti, W. G., Pergamon Press, New York, 1960, pp. 344-377.

3-7. Rubin, I., "Shock Curvature Effect on the Outer Edge Conditions of a Laminar Boundary Layer," AIAA Journal, Vol. 1, 1963, pp. 2850-2852.

3-8. Edquist, C. T., "Effect of Shock Curvature on Turbulent Heating of Sphere Cones," AIAA Journal, Vol. 2, 1964, pp. 1486-1487.

3-9. Dahm, T. J., Cooper, L. J., Rafinefad, D., Youngblood, S. B., and Kelly, J. T., "Passive Nosetip Technology (PANT II) Program: Vol. 1, Inviscid Flow and Heat Transfer Modeling for Reentry Vehicle Nosetips," FR-76-224, Acurex Corporation/Aerotherm Division, Mountain View, California, October 1976.

3-10. Moss, J. N., "A Study of the Aerothermal Entry Environment for the Galileo Probe," AIAA Paper No. 79-1081, presented at Orlando, Florida, June 4-6, 1979.

SECTION 4

A FEASIBILITY STUDY FOR EXPERIMENTAL ASSESSMENT OF HEATSHIELD SPALLATION

The candidate heatshield material for the Galileo probe program is carbon-phenolic. A recent study (Reference 4-1) suggested that mechanical erosion, also called spallation, is an important factor to be considered during the design of probe heatshield, and that there are currently no experimental data on carbon-phenolic performance in representative Jupiter entry environments. Although several mechanical erosion models exist, none have been verified with experimental data for heating environments typical of Jupiter entry. A study following a recommendation for an experimental program to evaluate the performance of carbon-phenolic in a typical Jupiter entry environment was undertaken. The first step defined an optimum feasible experiment to assess the carbon-phenolic spallation; the purpose of which was to review the available literature and collect existing data on carbon phenolic spallation, identify the conditions to be simulated in an experiment, locate a facility that can generate the required conditions, and finally, define the test conditions for the experiment. The following subsections briefly review the available experimental data on carbon-phenolic spallation, summarizes the theoretical models on spallation, simulation parameters, survey of test facilities, and selection of a test facility. In addition, a preliminary experiment is also defined, and, based on this study, a test program is recommended to assess the heatshield spallation.

4.1 LITERATURE SURVEY

Carbon-phenolic has frequently been used as heatshield material on earth reentry vehicles. Because of the nature of application, extensive tests were conducted on carbon-phenolic at various test facilities and theoretical models were developed to explain the test data. Available test data and analysis to predict spallation were collected as a part of this study and were reviewed. A brief summary on the available literature is given in the following subsection.

4.1.1 Experimental Evidence of Spallation

Experimental data on carbon-phenolic is available from laser, arc jet, and flight tests. Massive spallation was observed in the laser environments conducted by Brewer (Reference 4-2), Lundell and Dickey (Reference 4-3), and MDAC (Reference 4-4). Based on the laser test data, it may be concluded that the carbon-phenolic heatshield will spall; however, during laser tests, the laser beam was nonuniform, thus leading to an uneven heating load on the test specimen. Also, to obtain increased heat flux on the model, the laser beam was made small in diameter. Moreover, the specimens were exposed to sudden laser heating without any preheating of the model.

Due to spatial and temporal nonuniformity of the beam, the incident heat flux cannot be accurately measured. The small laser beam diameter and lack of preheating may induce thermal shock in the specimen which may cause spallation.

Carbon-phenolic heatshields were tested in arc jet environments by Schneider, et al. (Reference 4-5), Bishop, et al. (Reference 4-6), and

Acurex/Aerotherm (References 4-7, 4-8, and 4-9). Except for Reference 4-7, all of the arc jet tests showed spallation even at low heat flux conditions (2.6 kJ/cm^2sec). It was postulated that the heatshield fabrication methods such as the layup angle and resin content were responsible for the spallation.

Spallation has been inferred from a reentry vehicle (flap) flight data (Reference 4-1). This was based on the discrepancy between the measured recession data and the calculated thermochemical ablation allowing for roughness heating augmentation. Table 4-1 summarizes the available data on carbon-phenolic spallation.

4.1.2 Theoretical Spallation Models

A literature search yielded about six spallation models based on both theory and empirical constants. Table 4-2 presents a summary of available spall models from which the basic mechanisms proposed for spallation in general are thermal stresses, pyrolysis gas pressures, and shear stresses.

Thermal stresses cause material degradation, including delamination and cracking of individual plies. Pyrolysis gas pressure and shear stresses cause failure and material removal. For planetary entry application, shearing stresses are believed to be of secondary importance due to the anticipated massive blowing.

Howe (Reference 4-10) developed a theoretical model to predict the importance of spallation for a uniformly heated spherical shell of noncharring graphitic type material. This model indicates that the model radius is not a critical parameter because, for a carbon-phenolic type material, the hoop stress is essentially independent of the model's outer radius.

Table 4-1. Summary of Carbon-Phenolic Spallation Data

Test Program/Reference	Facility	Test Conditions	Material	Data	Spallation Observed?
Brewer (Reference 4-2)	Laser 5 kW CW CO_2 gas	Power 4 kW/cm² 2 sec test time, air, N_2, He at P = 1, 0.3	Carbon-phenolic 55 percent resin, ~ 1.45 gm/cm³	Problems with test, not much data reported; E ~ 16 MJ/kg	Yes, "sizable pieces of material were ejected"
Lundell and Dickey (Reference 4-3)	Laser ~30 kW CW CO_2 gas	P = 1 atm 15 - 150 kW/cm² (with a peak), N_2 jet near model	2-D CP from MDAC, 35 percent resin, ρ ~ 1.46 gm/cm³	$\dot{s}$ = 1.3 - 7 cm/sec for I = 15 - 90 kW/cm²; T_s to 3900K; E* = 20 - 35 MJ/kg	Yes, "spallation decreases as I increases" (photograph)
MDAC-W IR and L tests and data collection (Reference 4-4)	Lasers CW CO_2 gas (AFWL and Philco)	I = 1 - 25 kW/cm² with and without airflow; beam diameter < specimen	Carbon-phenolic, many different types, resin fractions, layups ρ = 1.28 - 1.5 gm/cm³	Q* = 4000 to 60,000 kJ/kg (some individual data may be available from specific test reports)	Yes, sometimes massive
Schneider, et al. (Reference 4-5)	CAL wave superheater	H_0 = 5200 kJ/kg P_0 = 5 - 15 atm, q_c = 11,350 to 45,400 kW/m² sec; t ~ 2.5 sec, yawed cylinder model	Carbon-phenolic, tapewrap and rosette (details not stated)	$\dot{s}$ = 0.5 - 2.5 cm/sec (which is two or three times thermochemical)	Yes; (char spallation)
Bishop and DiCristina (Reference 4-6)	CAL wave superheater	H_0 = 5345 kJ/kg P_0 = 80 atm	Carbon-phenolic, forward Dixie Cup nosetip (R_N = 0.64 cm), and 45° wedge	Not available	Yes, cones, Dixie Cup layers were removed
1971 50 MW test series (Reference 4-7)	AEDC AFFDL 50 MW	Flat enthalpy H = 5100 kJ/kg P_c = 83 atm	Carbon-phenolic (R6300); R_N = 0.64 cm and 45° conic	$\dot{s}$ = 0.89 cm/sec; T_w = 3445°K	No
Passive Nosetip Technology technology transition tests (Reference 4-8)	AEDC AFFDL 50 MW (large nozzle, low P_{t_2}, flat H)	H_{CL} = 4640 kJ/kg, P_c = 14, 16, 25 atm (test times to 20 sec)	Carbon-phenolic, reversed Dixie Cup, R_N = 0.64 to 1.65 cm, 30° conic	$\dot{s}$ = 0.2 cm/sec; T_w = 3610K for large model at 24 atm $\dot{s}$ = 0.13 cm/sec; T_w = 3500K; small model at 14 atm	No for larger models at 25 atm Yes for small models at low P (charred very deeply and delaminated)
Model holder performance during steady-state ablation tests (Reference 4-9)	AEDC AFFDL 50 MW	H_{CL} = 11,600 kJ/kg, H_{bulk} = 5345 kJ/kg, P_c = 150 atm, (environment at model holder not well characterized since it is out of test area)	Carbon-phenolic (fiber is MX 4926 typical), circumferentially wrapped model holders, front face cut at 15° to centerline, holds 1.27 cm diameter model	$\dot{s}$ = 1.3 to 2.5 cm/sec	Yes; in movies
Reentry vehicle flight test [illegible] data (Reference 4-1)	Flight	At flap, P = 9 atm, H_0 = 21,900 kJ/kg, q = 20 kW/cm²	Carbon-phenolic (fiber is MCC-3), 42 percent resin, ρ ~ 1.43 gm/cm³ [illegible] flaps, deflection angle 10°, 15°, 20°, 25°	Measured recession agrees with thermochemical recession up to 20° deflection	Yes, spallation inferred for 25° deflection due to underprediction of recession

Table 4-2. Summary of Theoretical Spallation Models

Source	Intended Application	Suggested Spallation Mechanism	Critical Parameters
Howe (Reference 4-10)	Planetary entry	● Thermally induced tangential/radial stress failure	● Transient temperature distribution ● Surface pressure ● Material physical characteristics
Aerotherm/Acurex (Reference 4-1)	Galileo Probe forebody heat-shield, rocket nozzle	● Negligible char strength above a temperature of 3750°K	● Transient temperature distribution
Mathieu (Reference 4-11)	Reentry vehicle and rocket nozzle design	● Thermal degradation of carbon-phenolic ● Char removal by surface shear and internal gas pressure	● Transient temperature distribution ● Surface shear ● Char thickness ● Surface pressure ● Gas pressure ● Material physical characteristics
Bishop, et al. (Reference 4-6)	Reentry vehicle	● Thermal degradation of carbon-phenolic ● Char removal by shear	● Char thickness ● Surface pressure ● Surface pressure gradient
Schneider, et al. (Reference 4-5)	Reentry vehicle	● Thermally induced char fracture along ply boundaries ● Material removal by internal gas pressure and surface shear	● Transient temperature distribution ● Surface shear ● Char thickness ● Surface pressure ● Gas pressure ● Material physical characteristics
Kratsch, et al. (Reference 4-12)	Galileo Probe	● High in-plane thermal and structural stresses ● Internal gas pressure on the charred material	● Transient temperature distribution ● Char thickness ● Surface pressure ● Gas pressure ● Material physical characteristics

Mathieu (Reference 4-11) proposed that spallation is caused by thermal stresses, surface shear forces, and pyrolysis gas pressure. According to Mathieu, spallation occurs when either the char thickness or the normal stress exceeds an empirically determined critical value.

Bishop and Dicristina (Reference 4-6) suggested that char spallation sharply reduces the material strength due to supporting resin structure degradation and subsequent material removal by surface shear and pressure gradient forces. On the basis of experimental and theoretical results, a correlation for critical char thickness as a function of surface pressure was developed.

Schneider,.et al. (Reference 4-5) developed an analytical model based on a comprehensive analytical and experimental study on carbon-phenolic spallation. Spallation, they concur, results from thermally induced fracture along ply boundaries coupled with material removal by pyrolysis gas pressure/aerodynamic shear. The model agrees well with the experimental data.

Kratsch, et al. (Reference 4-12) identified the action of pyrolysis gas pressure on charred material and high in-plane thermal/structural stresses as the major causes of heatshield spallation. They proposed a sequence of events leading to material removal starting with the contention that, under extremely high heat flux conditions, carbon-phenolic goes through explosive expansion normal to the plies which lead to interlaminar shear failure along with an outward rotation of plies. These delaminated plies experience a flexural failure due to the pyrolysis gas pressure.

In summary, it can be concluded from the spallation data and theoretical models, that spallation is basically a material stress related phenomenon. Any experiment designed to assess spallation must accurately simulate:

- Spatical and temporal temperature distribution
- Material physical characteristics
- Pyrolysis gas pressure
- Shear stress

4.2 SIMULATION PARAMETERS

Surveys of the available test data on carbon-phenolic and theoretical models on spallation indicated certain mechanisms for spallation. This study's objectives can be met if an experiment can be designed to simulate the Jupiter entry condition and the physical factors that were identified as probable causes of spallation. With that understanding, a set of simulation parameters were identified and were divided into primary and secondary simulation parameters.

The primary simulation parameters selected were: (1) thermochemical recession rate, $\dot{s}_{tc}$, (2) surface temperature, T_w, and (3) material physical characteristics.

Secondary simulation parameters selected were: (1) surface pressure, p, (2) surface pressure gradient, $\partial p/\partial s$, (3) surface shear, τ_w, (4) surface temperature rise, $\partial T_w/\partial t$, and (5) model geometry.

The following subsections provide the basis for selecting the above primary and secondary simulation parameters.

4.2.1 Primary Simulation Parameters

Calculated values of thermochemical recession rate ($\dot{s}_{tc}$) and surface temperature (T_w) as a function of entry time, for a typical Jovian entry, are shown in Figure 4-1 and 4-2, respectively; these values were taken from Reference 4-1. As shown in Figure 4-1, the peak recession

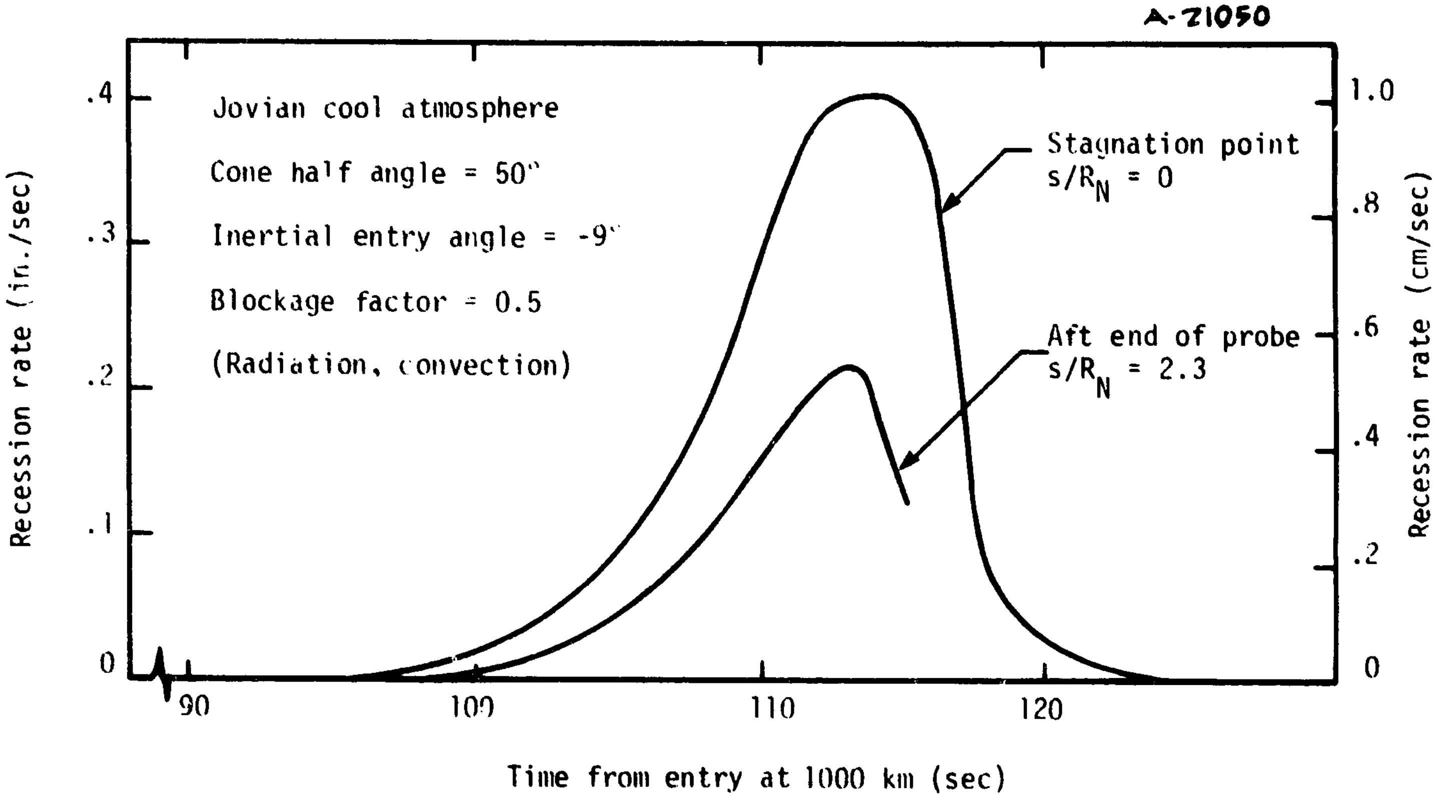

Figure 4-1. Predicted Thermochemical Recession Rate for Entry into Jovian Cool (Hunten) Model Atmosphere

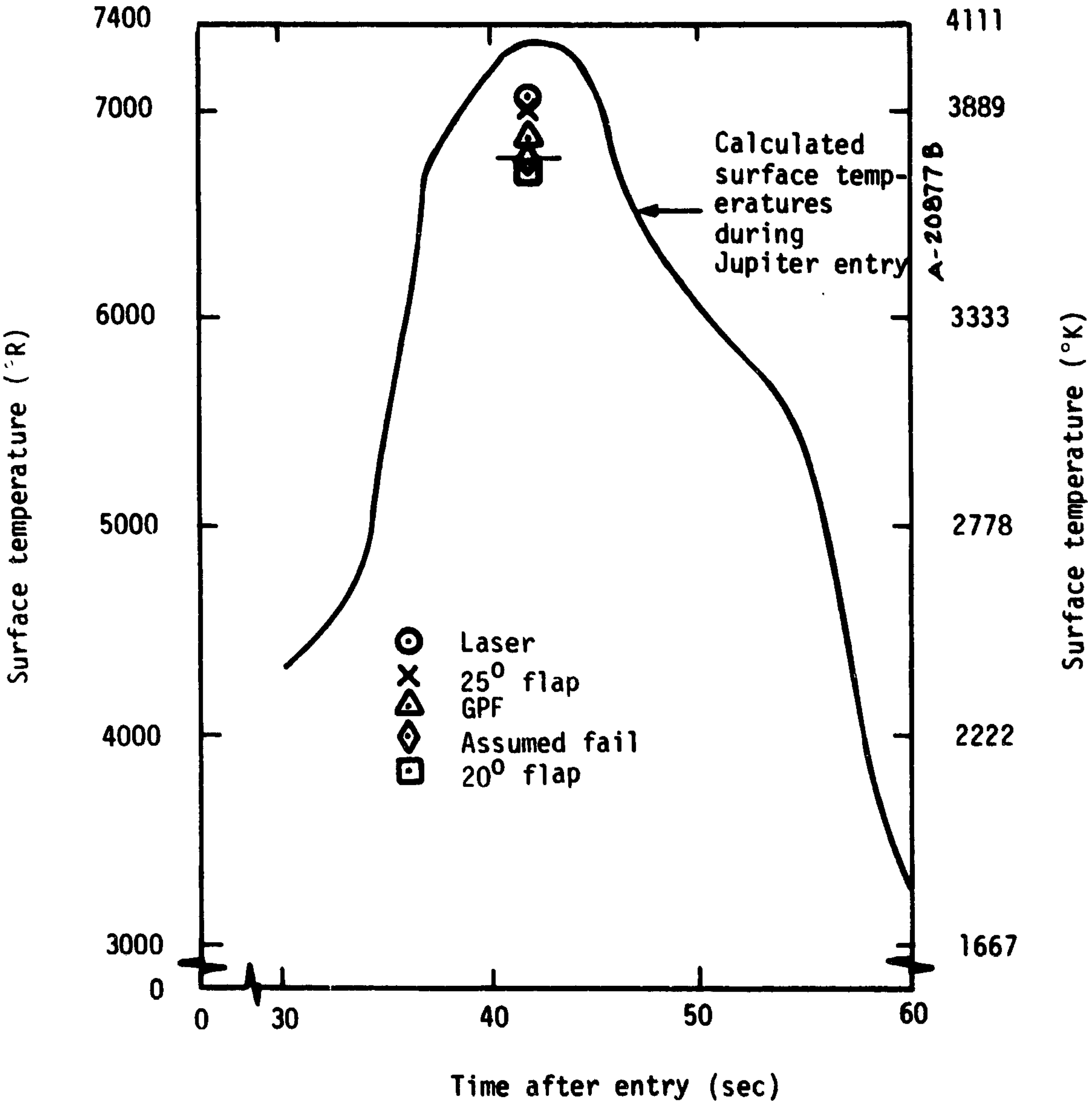

Figure 4-2. Comparison of Predicted and Measured Surface Temperatures

rate is about 1 cm/sec at the stagnation point, and about 0.5 cm/sec at the end of probe flank. The entry conditions and model atmosphere used to generate these figures correspond to the worst heating environments the probe may encounter. Based on this, and a desire to simulate a series of test conditions, $\dot{s}_{tc}$ was assigned a range between 0.5 and 1.0 cm/sec.

Figure 4-2 shows that the surface temperatures may reach as high as $4055^{\circ}K$ during entry. Also shown are the surface temperatures that have been recorded in ground based facilities. During laser tests that produced massive spallation, the surface temperature reached a maximum of $3889^{\circ}K$. For simulation purposes, the surface temperature was assigned a range between $3889^{\circ}K$ and $4167^{\circ}K$.

The literature search indicated that material physical characteristics play a key role in spallation. Material characteristics include carbon-cloth layup angle, wrap technique, phenolic resin content, and other manufacturing processes; however, these factors are beyond the control of the present study. Therefore, a test of the baseline carbon-phenolic material with known physical characteristics were considered.

4.2.2 Secondary Simulation Parameters

The primary simulation parameters discussed above may have a first order effect on the experiment, therefore, their accurate simulation is critical. However, there are other parameters that have an influence on carbon-phenolic spallation which are of second order importance. Table 4-3 lists these secondary simulation parameters along with their levels.

4.3 SURVEY OF TEST FACILITIES

The simulation parameters and their levels identified in subsection 4.2, established the requirements of a test facility; e.g., if the

Table 4-3. Primary and Secondary Simulation Parameters and Levels

Parameter	Level
Primary	
• Recession rate, $\dot{s}_{tc}$	0.5 to 1.0 cm/sec
• Surface temperature, T_w	3889 to 4167°K
Secondary	
• Surface pressure, p[a]	10 atm
• Surface pressure gradient, $\partial p/\partial s$[b]	1.6×10^6 N/m^2/m
• Surface shear, τ_w[c]	~0
• Surface temperature rise, $\partial T_w/\partial t$[d]	~100°K/sec for $T_w < 2722^{\circ}K$ ~550°K/sec for $T_w > 2722^{\circ}K$
Model nose radius, R_N[e]	>0.5 cm

[a] Surface Pressure, p:
A peak stagnation point pressure of 10 atm is predicted. Simulation is required due to it's impact on the pyrolysis gas velocity as indicated by Darcy's Law.

[b] Surface Pressure Gradient, $\partial p/\partial s$:
Maximum surface pressure gradient predicted is about 1.6×10^6 N/m^2/m. Simulation is required due to the shearing effect of pressure gradient on the char layer.

[c] Surface Shear, τ_w:
Due to the massive blowing, the surface shear is predicted to be essentially zero. The experiment should simulate the zero shear condition due to the impact of shear on spallation.

[d] Surface Temperature Rise, $\partial T_w/\partial t$:
For temperatures below 2722°K, the predicted surface temperature rise is comparatively low -- about 100° K/sec. This should be simulated since a very steep temperature rise may induce spallation. Inability to simulate this has been one of the drawbacks of laser testing to date.

[e] Model Nose Radius, R_N:
While no primary constraints have been imposed on the model geometry, it is judged that the geometry selected should allow for baseline wrapping technique and, in addition, some flexibility in varying it. Material spallation can be induced due to poor wrapping techniques. Based on a brief survey of this problem, a minimum nose-radius of 0.51 cm was selected.

conditions given in Table 4-3 can be obtained in any facility, then the question of spallation of carbon-phenolic heatshield during entry into Jovian atmosphere can be answered. To find out which ground based facilities can generate the required heating environment, a survey of all test facilities in the United States was conducted for information on their capabilities, limitations, and availability for test in a given time frame. In addition, the survey gathered information on the use of various test gases, type of heating environment, and the flexibility to use other candidate test gases.

Figure 4-3 illustrates the required recovery enthalpy, H_R, for achieving a thermochemical ablation rate, $\dot{s}_{tc}$, of 1 cm/sec as a function of local pressure, p, at the selected two temperature limits. It was assumed, for calculation purposes, that carbon-phenolic was ablating in an air environment. Figure 4-3 sets a guide for the requirements of a test facility using air as the test gas.

The facilities survey included arc jet, ballistic range, and laser heating environments. A summary of the various test facilities considered and their operational capabilities are given in Tables 4-4, 4-5, and 4-6.

The 50 MW (AFFDL) and HEAT1 (AEDC) arc jet facilities produce only convective heating environments. Between these two, the HEAT1 facility was considered to be more useful, as it can achieve a higher centerline enthalpy (H_{CL}) at a lower stagnation pressure (Pt_2). In addition, the HEAT1 facility will consider test gases other than air, particularly rich mixtures of O_2/N_2 required for producing large $\dot{s}_{tc}$. The HIP (MDAC) facility was not included since the maximum allowed model nose radius (R_N) is only 0.4 cm which is smaller than the selected model size for simulation.

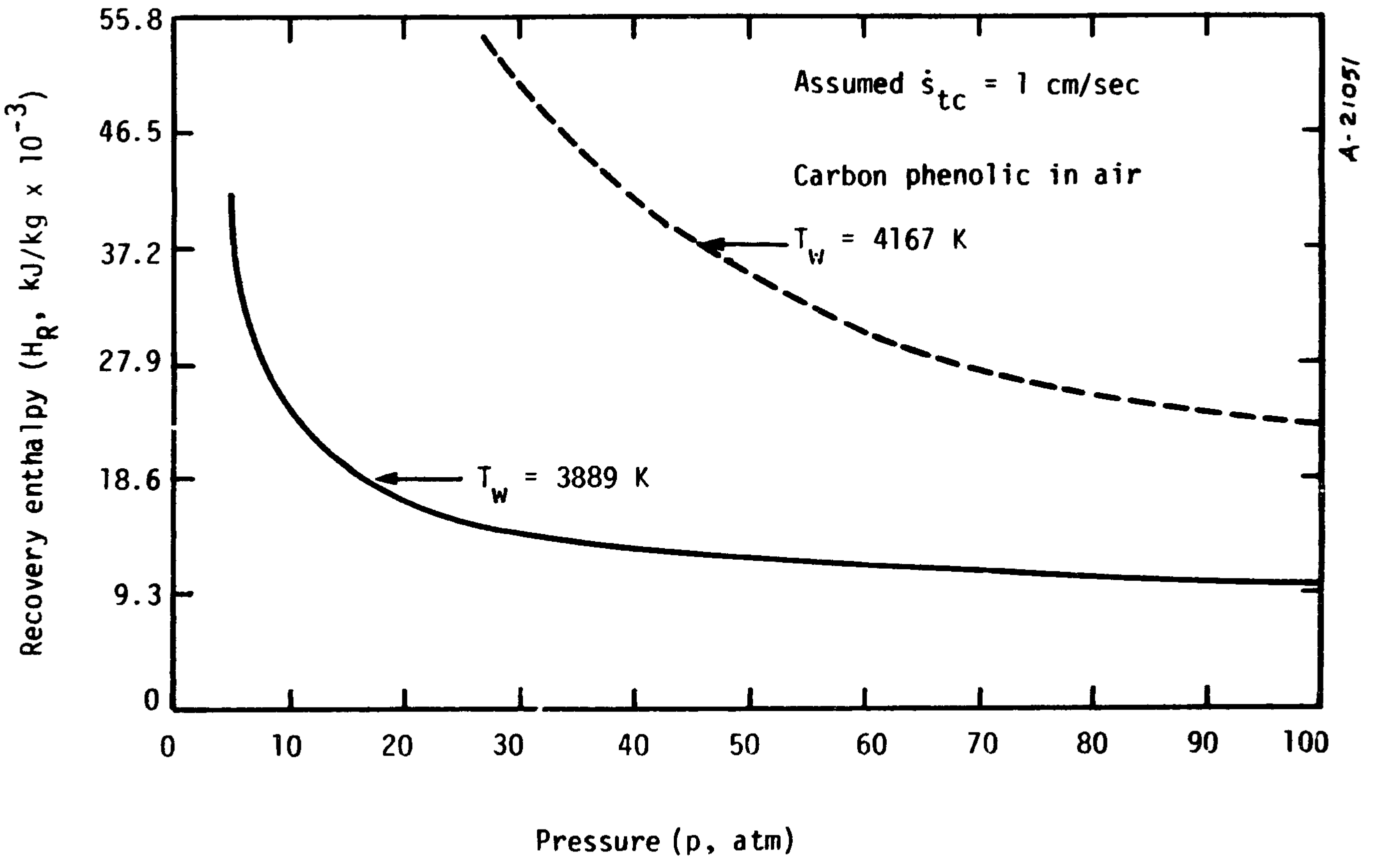

Figure 4-3. Recovery Enthalpy Requirements for Simulation in Convective Heating Air Environment

Table 4-4. Operational Range of Arc Jet Test Facilities Surveyed

Facility	Test Gas	Maximum Centerline Enthalpy (H_C, kJ/kg)	Maximum Stagnation Pressure (atm)	Maximum Radiative Heat Flux to 2.54 cm Diameter Model (MW/m^2)	Maximum Model Size (radius, cm)	Comments
CONVECTIVE HEATING ONLY						
50 MW (AFFDL)	Air	12,760	100 10	-- --	0.762 1.27	Will not consider other gases
HEAT1 (AEDC)	Air	18,560	75 10	-- --	0.889 1.52	Will consider other test gases
COMBINED CONVECTIVE AND RADIATIVE HEATING						
L4001 (NASA-Ames)	Air	27,840	1	79.5	1.91	Will consider other test gases
GPE (NASA-Ames)	H_2/He	498,800	2	60.2	5.08	Conditions achieved at time of survey
		628,720	2	90.0	5.08	Design conditions

Table 4-5. Operational Range of Ballistic Range Test Facilities

Convective Heating Environment

Facility	Maximum Centerline Enthalpy (H_C kJ/kg)	Maximum Stagnation Pressure (P atm)	Maximum Model Size To Be Used (Radius, cm)	Comments
RANGE-G (AEDC)	18,560	350	2.75	Can use various test gas mixtures; 300 m long range facility
HFFAF (NASA-Ames)	41,760	--	1.85	Various gas mixtures; 32 m long range; only shadow graphs

Table 4-6. Operational Range of Laser Test Facilities Considered

Radiative Heating Environment Only

Facility	Maximum Radiative Heat Flux to 2.54 cm Diameter Model (MW/m^2)	Comments
TSL (SANDIA)	283.8	150 kW laser
PW (Pratt & Whitney, Florida)	908	Large beam variator area ratio 8:1; will consider chamber test

Both the L4001 (NASA-Ames) and GPF (NASA-Ames) facilities create combined convective and radiative heating environments. The radiative flux from L4001 facility is derived from a 40 kw laser, while the radiative flux in GPF is emitted by the high temperature test gas mixture H_2/He. The GPF is under development, and the operational capability presented in Table 4-4 is achieved at the time of the survey. Higher power levels are anticipated in the near future. In addition to increased heating, the combined heating facilities can accommodate larger test models.

Ballistic range test facilities considered were the RANGE G (AEDC) and HFFAF (NASA-Ames). RANGE G offers free flight, or track guided model capability. RANGE G is roughly 300 m long, has sophisticated instrumentation, and has a model recovery system that offers a unique experimental capability. Models weighing up to 0.450 kg are routinely accelerated to a launch velocity of 5.8 to 6.1 km/sec using a two stage light gas gun. The HFFAF range offers a higher enthalpy and a shorter test section which is only 32 m long. The shorter range is not suitable to observe spallation.

The laser facilities considered were the TSL (SANDIA) and PW (Pratt and Whitney, Florida) facilities. The TSL facility has a 150 kw laser, and while an exact kw rating for the PW laser was not available to us, it is capable of delivering 800 kw/cm^2 to a 2.54 cm diameter model. However, the PW laser produces a nonuniform beam with the area ratio of 8:1.

4.4 SELECTION OF A TEST FACILITY TO PERFORM THE CARBON-PHENOLIC SPALLATION EXPERIMENT

The various test facilities surveyed and discussed in subsection 4.3 were evaluated to determine their suitability for performing the spallation experiment.

To answer the basic question, what are the enthalpy and pressure conditions that are required to produce the primary and secondary simulation parameter levels tabulated in Table 4-3, an analytical model was constructed based on steady-state energy balance equations.

Following Reference 4-1, under steady-state conditions, the surface energy balance equation (Q* type), valid only when the surface is in the sublimation regime, simplifies to

$$\dot{m}H_{ab} = (1 - \Psi_R)\, q_R + (1 - \Psi_c)\, q_c - q_{rr} \tag{4-1}$$

where $\dot{m}$ is the ablation rate, Ψ_R and Ψ_c are the respective radiative and convective blockage factors, H_{ab} is the heat of ablation, q_{rr} is the reradiated surface heat flux, q_R is the incident radiant flux and q_c is the convective flux to the wall.

For a convective heating only facility, $q_R = 0$, and for a radiative heating only facility $q_c = 0$. The reradiated heat flux is obtained from

$$q_{rr} = \epsilon\sigma T_w^4 \tag{4-2}$$

where ϵ is the emissivity of carbon-phenolic and is assumed to equal 0.85 in this study, σ is Stefan-Boltzman constant, and T_w is surface temperature.

The convective flux to the surface is usually written in terms of heat transfer coefficients, i.e.,

$$q_c = \rho_e u_e C_H\,(H_R - H_w) \tag{4-3}$$

where ρ_e is boundary layer edge density, u_e is edge velocity, C_H is a dimensionaless Stanton number for heat transfer, H_R is recovery enthalpy, and H_w is wall enthalpy.

The blockage factors given in Equation (4-1) can be found from correlations. For example, the convective blockage is obtained from

$$1-\Psi_c = \ln (1+2\lambda B')/2\lambda B' \qquad (4\text{-}4)$$

where B' is the dimensionless blowing parameter $B' = \dot{m}/\rho_e u_e C_H$, and λ is a correlation constant. For laminar flow it is 0.5, and is set to 0.35 for turbulent flow. The radiation blockage factors, Ψ_R, were obtained from Moss et al. (Reference 4-13).

In terms of blowing parameter B', recovery enthalpy H_R, and wall temperature T_w, Equation (4-1) becomes

$$H_R = \frac{(1-\Psi_R)q_R}{\rho_e u_e C_H} + H_w + B' \; H_{ab} + \frac{\varepsilon\sigma T_w^4}{\rho_e u_e C_H} \qquad (4\text{-}5)$$

Equation (4-5) is used to evaluate the various test facilities. The Aerotherm Chemical Equilibrium (ACE) code (Reference 4-14) was used to generate the blowing parameter B' and wall enthalpy H_w as a function of surface pressure p, surface temperature T_w, and for various test gases. For calculating the B', a 35 percent resin content was assumed for carbon-phenolic. The density of the material was assumed to be 1.46 gm/cm^3. The recession rate $\dot{s}$ and B' are related by

$$\dot{m} = B' \; \rho_e u_e C_H = \rho\dot{s} \qquad (4\text{-}6)$$

or $$\dot{s} = \frac{B'}{\rho} \cdot \rho_e u_e C_H$$

To meet the negligible shear simulation requirement, calculations were restricted to the stagnation region only. The required model nose radius R_N was computed from the correlation from Rindal, et al. (Reference 4-15). The correlation is

$$R_N = A^2 p/\rho_e u_e C_H \Big|_{\text{unblown}} \tag{4-7}$$

The correlation constant A is tabulated in Table 3-7 for various gases. For arbitrary mixtures such as H_2/He, H_2/N_2, and N_2/O_2, the correlation constant A was calculated based on the recommendation of Zoby (Reference 4-16), i.e.,

$$A = 1/(\sum_i m_i/A_i) \tag{4-8}$$

where m_i is the mass fraction of component i and A_i is correlation constant (from Table 4-7) for component i.

Equations (4-4) to (4-7) were used to compute the values of H_R, $\rho_e u_e C_H$, and R_N for various test gases/gas mixtures as a function of surface pressure p and temperature T_w, and an assumed value of $\dot{s}_{tc}$.

Using the formulated analytical model, the various facilities were evaluated on the basis of their heating environment. Convective heating facilities are discussed in subsection 4.4.1; combined heating facilities are evaluated in subsection 4.4.2; and radiative heating facilities are considered in subsection 4.4.3.

Table 4-7. Correlation Constant A for Various Gases

Gas	Constant A
Air	0.229
Nitrogen	0.218
Oxygen	0.261
Argon	0.287
Hydrogen	0.0765
Helium	0.121

4.4.1 Convective Heating Facilities

The convective heating facilities evaluated are the RANGE G, HEAT1, and GPF in convective heating mode. For the GPF, convective heating accounts for about 70 percent of currently achieved and rated heating capability.

Carbon-phenolic ablation in air, oxygen, nitrogen, argon, and gas mixtures of H_2/He and H_2/N_2 were investigated using the analytical model described in subsection 4.4. The recovery enthalpy, heat transfer coefficient, and model nose radius requird to produce an assumed ablation rate ($\dot{s}_{tc}$) and surface temperature were compared to the facility operating capability.

Figure 4-4 illustrates this comparison for carbon-phenolic ablation in air, for an assumed value of $\dot{s}_{tc}$ = 1 cm/sec at T_w = 3889 and 4167°K. As shown, the enthalpy requirements exceed the facility capability for pressures below 15 atm. The model nose radius required to simulate the transfer coefficient is too small, roughly about 0.05 cm, which is an order of magnitude smaller than the simulation requirement.

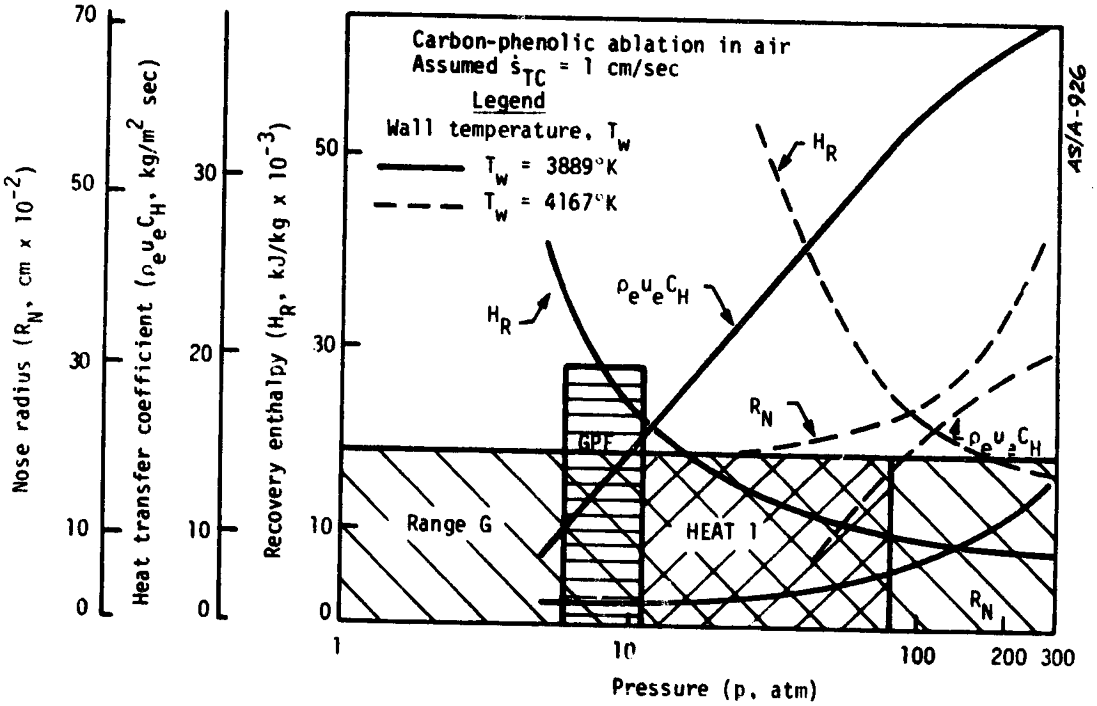

Figure 4-4. Carbon-Phenolic Ablation in Air Environment and Comparison of Required Enthalpy to Candidate Facility Performance

Using nitrogen as a test gas only results in smaller nose radius due to its lower chemical activity compared to air. Argon gas was also considered, but was rejected since it had the same deficiency as nitrogen due to its inert nature.

Figure 4-5 illustrates carbon-phenolic ablation in oxygen environment. Its higher chemical activity compared to air, nitrogen, and argon results in significantly larger nose radius. However, the increased B' requires a larger enthalpy. RANGE G is the only candidate facility that would consider oxygen as a test gas at test pressures around 100 atm. For conditions shown in Figure 4-5, the required enthalpy exceeds RANGE G capability below about 80 atm stagnation pressure. For a 100 atm test pressure, a model nose radius results in 0.64 cm which is adequate to achieve the desired transfer coefficients.

The convective heating mode capability of GPF was evaluated considering test gas mixtures of H_2/He and H_2/N_2. For H_2/He, the volume fractions for the gas mixture was assumed to be 78/22. For H_2/N_2, the volume fraction was taken as 50/50. Figure 4-6 and 4-7 show that the GPF in the convective heating mode is inadequate for achieving the desired level of simulation.

Having determined that air, nitrogen, oxygen, and gas mixtures of H_2/He and H_2/N_2 environments will not adequately simulate the required test conditions in the convective heating fcilities, attention was given to N_2/O_2 gas mixture as test gas in RANGE G and HEAT1 facilities. The test facility personnel at HEAT1 indicated an interest to run the facility at O_2/N_2 mixtures as rich as 65/35 by volume.

Detailed iterative computations were performed to evaluate an optimum model size for various assumed ablation rates of 0.5, 0.75, and 1.0 cm/sec at

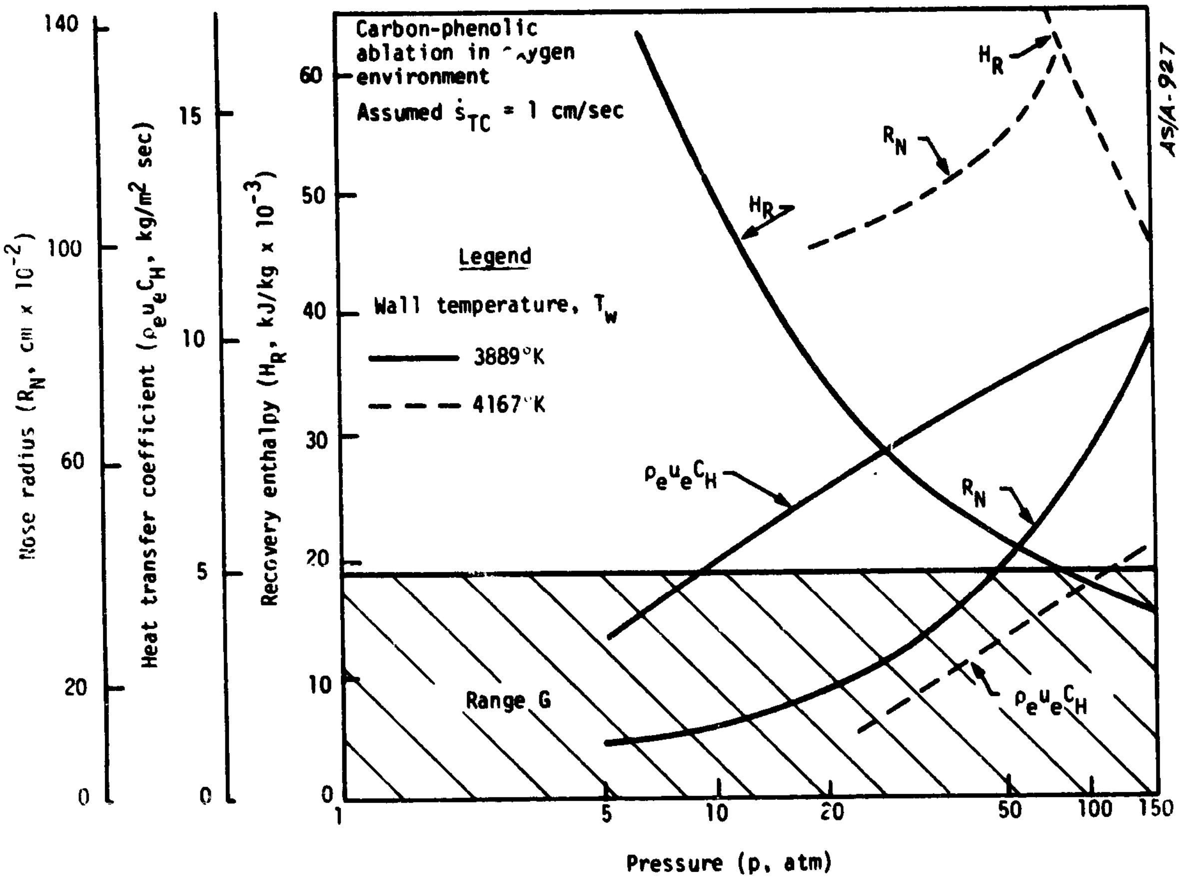

Figure 4-5. Carbon-Phenolic Ablation in Oxygen Environment and Comparison of Required Enthalpy to RANGE G Performance

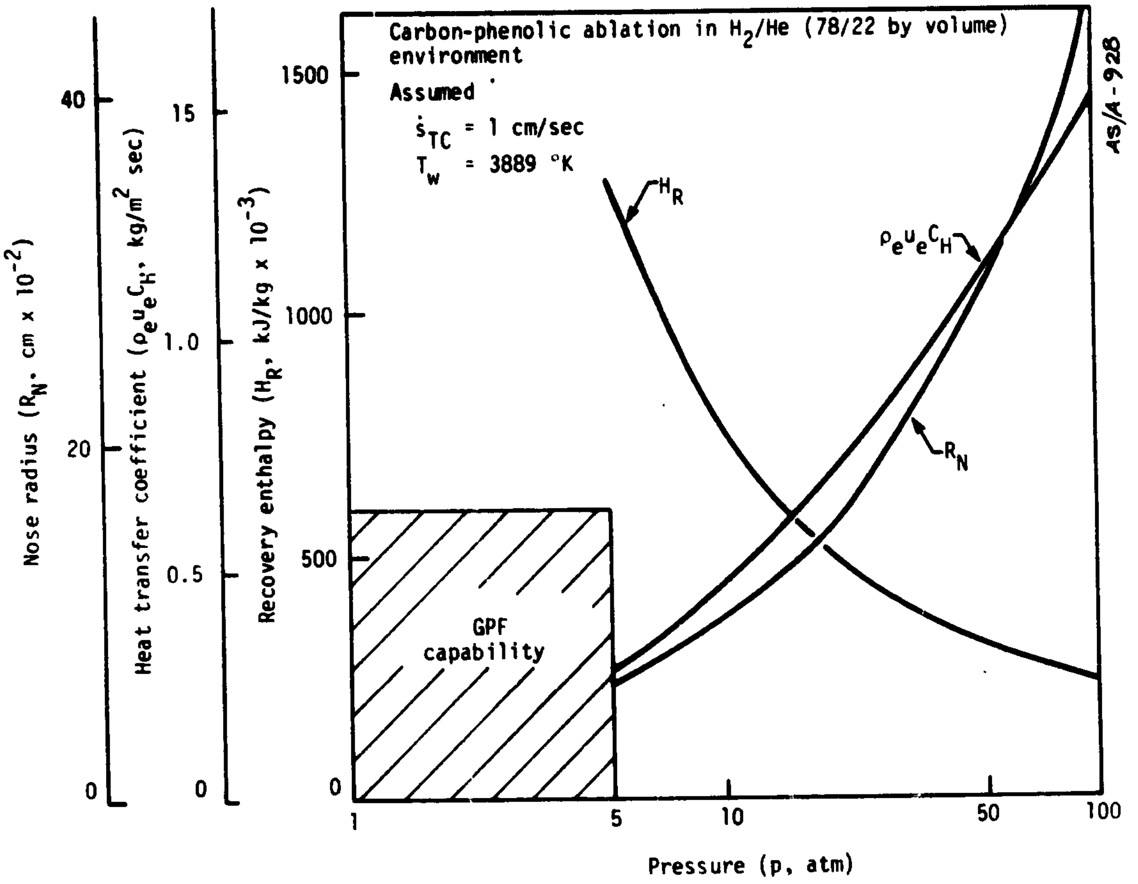

Figure 4-6. Carbon-Phenolic Ablation in H_2/He Environment and Comparison of Required Enthalpy to GPF Capability

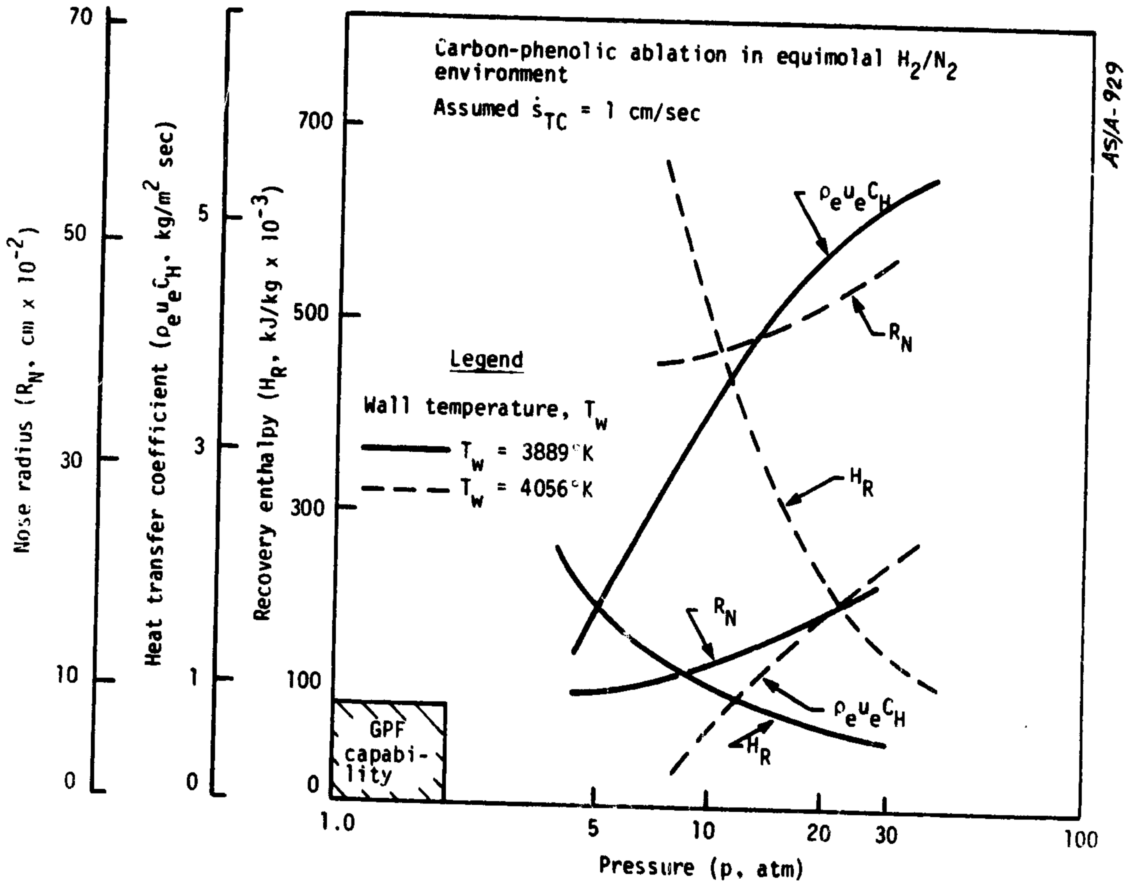

Figure 4-7. Carbon-Phenolic Ablation in Equimolal H_2/N_2 Environment and Comparison of Required Enthalpy to GPF Capability

a given surface temperature of 3889°K. The calculations resulted in model nose radius of 0.635 cm. Figure 4-8 presents the required enthalpy levels for various mixture ratios of O_2/N_2 and stagnation pressures. The higher ablation rate (0.75 and 1 cm/sec) test conditions cannot be obtained in the HEAT1 facility. However, the performance map of RANGE G covers even the most severe ablation rate condition.

Figure 4-8 shows the selection of the RANGE G facility as a candidate facility to conduct carbon-phenolic spallation experiments. The test conditions and preliminary experimental design will be discussed in subsection 4.5.

4.4.2 Combined Heating Facilities

The combined heating facilities, L4001 (NASA) and GPF (NASA), were evaluated with the aid of the analytical model described in subsection 4.4. For evaluation purposes, wall temperature T_w was assigned the value of local sublimation temperature to maximize radiative heating by uncoupling the mass transfer from the model nose radius. The incident radiative flux q_R was obtained by contacting the facilities. The sublimation temperature as a function of pressure was calculated using the ACE computer code (Reference 4-14).

The laser aided L4001 (NASA) facility was evaluated for the operating conditions of 1 atm pressure and a model size with a nose radius of 0.635 cm. For these assumed conditions, this facility supplies an incident radiant flux q_R of 315.6 MW/m^2, and has a recovery enthalpy of 27.8 MJ/kg. The local sublimation temperatue of 3819°K is below the minimum wall temperature of 3889°K and the difference is ignored. For three assumed values of ablation rates, the total heat rfluxes required are calculated; and the results are summarized in Table 4-8. The table

AS/1-930

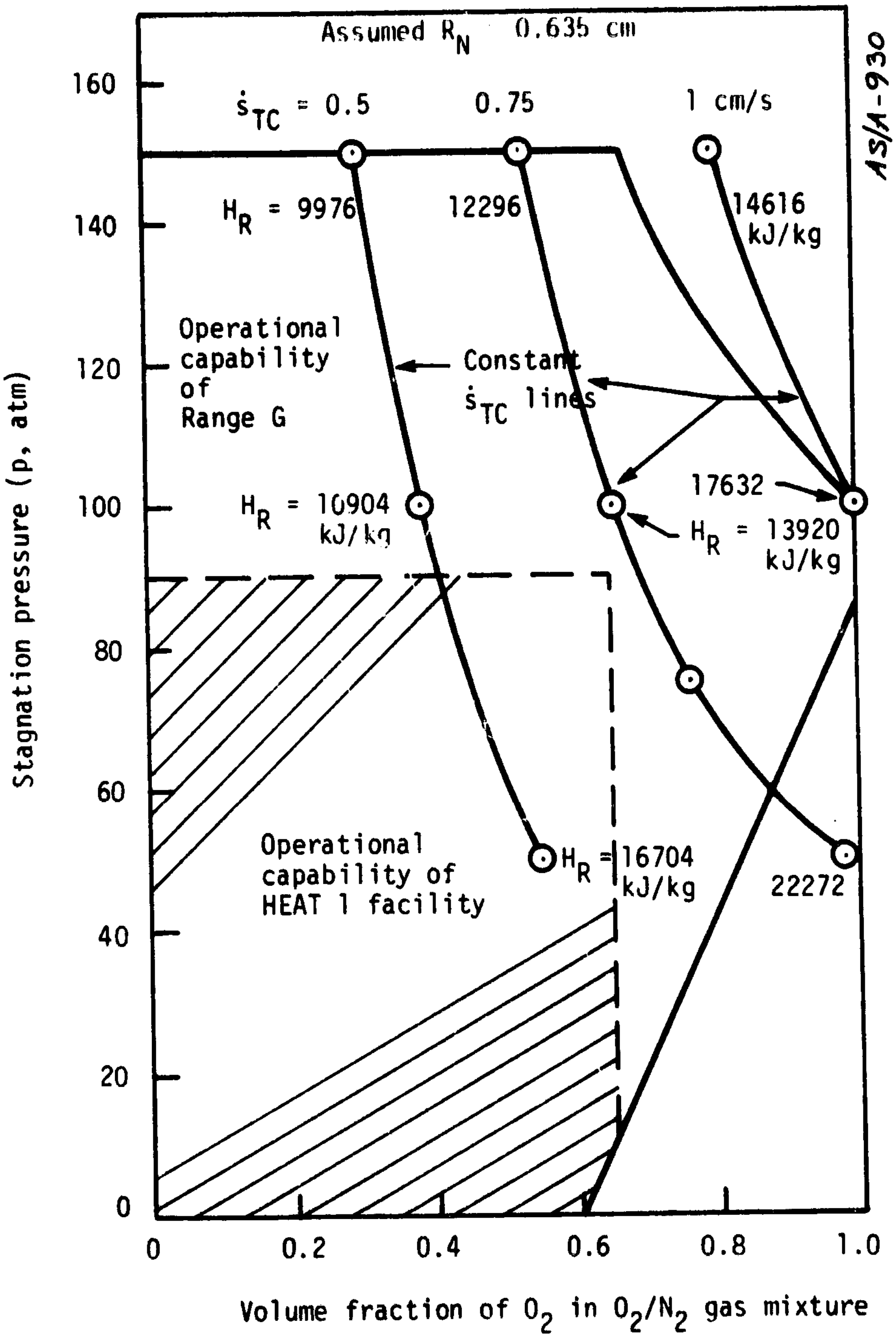

Figure 4-8. Convective Heating Facility Selection

Table 4-8. Evaluation of L4001 (NASA) Combined Heating Facility

Assumed Conditions

Carbon-phenolic ablation in air:

$P = 1$ atm, $T_W = 3819$ K, $H_W = 22.62$ MJ/kg

$R_N = 0.635$ cm, $q_R = 315.6$ MW/m^2, $H_R = 27.8$ MJ/kg

Assumed Recession Rate ($\dot{s}_{tc}$ cm/sec)	Total Flux Required for Simulation (MW/m^2)	Available		
		Convective Flux (MW/m^2)	Radiative Flux (MW/m^2)	Total Flux (MW/m^2)
0.5	184.7	2.6	157.8	160.4
0.75	271.8	2.0	157.8	159.8
1.0	359.0	1.7	157.8	159.5

shows that the simulation capability of L4001 is inadequate. For example, for an assumed $\dot{s}_{tc}$ of 1 cm/sec, the available total flux is less than one half that required.

A similar evaluation for GPF (NASA) is performed, and the results are provided in Table 4-9. Again, the simulation capability is inadequate. For producing a recession rate of 1 cm/sec, the available heat flux is roughly one third of that required.

In summary, the existing combined heating facilities do not offer adequate simulation for carbon-phenolic spallation experiment.

4.4.3 Radiative Heating Facilities

The radiative heating facilities evaluated are the two laser facilities, TSL and PW. The TSL facility was evaluated at atmospheric

Table 4-9. Evaluation of GPF (NASA) Arc Jet Facility

Assumed Conditions

Carbon phenolic ablation in H_2/He = 50/50 by volume environment:

$P = 2.82$ atm, T_w 3903 K, $H_w = 22.7$ MJ/kg

$R_N = 2.54$ cm, $q_R = 110$ MW/m^2, $H_R = 729.8$ MJ/kg

Assumed Recession Rate s_{tc} (cm/sec)	Total Flux Required for Simulation (MW/m^2)	Available Flux		
		Convective (MW/m^2)	Radiative (MW/m^2)	Total (MW/m^2)
0.50	183.0	71.1	71.5	142.6
0.75	268.9	54.1	71.5	125.6
1.00	354.7	44.2	71.5	115.7

pressure conditions, and the PW laser facility was evaluated at the required simulation pressure of 10 atm and has enough power and adequate technology to deliver up to 900 MW/m^2 to a 2.54 cm diameter model.

Performing the calculations using the analytical model described in subsection 4.4, showed that at the PW facility, the required conditions for simulation can be attained. The TSL facility was found to be inadequate to test a 2.54 cm diameter model; however, a smaller model of 1.27 cm diameter can be tested. Based on the calculation, the PW facility was also selected as a possible candidate for performing the carbon-phenolic heatshield spallation experiment. When performing the laser tests, the beam should be well focused so that there is beam uniformity. Also, the model must be preheated to a certain temperature level of 2500^0K, to avoid thermal shocking of the model when the laser heating is activated.

4.5 PRELIMINARY EXPERIMENT DEFINITION

Between the RANGE G and PW laser facility, RANGE G was selected as the best possible test facility for heatshield spallation assessment experiment. The RANGE G facility offers sophisticated instrumentation; it has performed an important role in assessing reentry vehicle nosetip and heatshield material technology, and offers high heat flux capacility along with wide variation in testing conditions. However, RANGE G cannot be effective at the required low simulation pressure of 10 atm. Since surface pressure is primary in spallation, performing experiments at high pressure is useful to assess the sensitivity of pressure on spallation.

The selected test matrix is given in Table 4-10. The indicated model nose radius of 0.63 cm is the equivalent radius of curvature at the stagnation point. A blunt faced model will be designed for the experiment to simulate the required negligible shear and flat heating profile.

4.6 SUMMARY AND CONCLUSIONS

A study was conducted to define an optimum feasible experiment to assess carbon-phenolic heatshield spallation. A literature survey yielded experimental data and theoretical models on carbon-phenolic spallation; a set of simulation parameters and their levels were established based on available data, theory and the Jupiter worst entry heating environment. A facilities survey was also conducted, and the capabilities of arc jet, ballistic range, and laser test facilities were obtained.

Based on a Q* type surface energy balance model, requirements to simulate the conditions were compared with the performance availability of

Table 4-10. Preliminary Experiment Definition and Test Matrix

Test Facility: RANGE G (AEDC)

Environment: O_2/N_2

Model Effective Nose Radius = 0.635 cm

Recession Rate ($\dot{s}_{tc}$ cm/sec)	Test Pressure (P atm)	Wall Temperature (T_w K)	Recovery Enthalpy (H_R MJ/kg)	Mole Fractions of O_2/N_2 Gas Mixture
0.50	100	3889	10.9	37/63
0.75	100	3889	13.9	66/34
1.00	100	3889	17.6	100/0
0.75	150	3889	12.3	53/47
0.75	75	3889	17.2	80/20

facilities. The above comparison led to two candidate facilities: a convective heating only facility (RANGE G) and a radiative heating only facility (PW laser). Based on other considerations, RANGE G is thought to be the best candidate facility to perform the carbon-phenolic heatshield spallation experiment. A test matrix was also defined for the RANGE G facility.

The model selected is blunt faced with an equivalent nose radius of 0.635 cm. The test gas selected is O_2/N_2 gas mixture and composition is varied in the test matrix. However, before the experiment, model design and O_2/N_2 operating map of RANGE G must be investigated.

4.7 REFERENCES

4-1. Balakrishnan, A., Laub, B., Chu, E., and Nicolet, W. E., "Outer Planet Probe Thermal Protection: Heating Environments and Spallation Assessment, Acurex Final Report to NASA-Ames Research Center, 1978.

4-2. Brewer, W. D., "Ablative Material Response to CO_2 Laser Radiation," Journal of Spacecraft and Rockets, Vol. 7, No. 12, p. 1449-1453, December 1970.

4-3. Lundell, J. H., and Dickey, R. R., "The Response of Heatshield Materials to Intense Laser Radiation," AIAA Paper No. 78-138, presented at Huntsville, Alabama, January 1978.

4-4. Washburn, R. M., private communication, Acurex Corporation, Aerospace Systems Division, Mountain View, California, May 1978.

4-5. Schneider, P. J., Dolton, T. A., and Reed, G. W., "Mechanical Erosion of Charring Ablators in Ground-Test and Reentry Environments," AIAA Journal, Vol. 6, No. 1, p. 64-72, January 1968.

4-6. Bishop, W. M., and DiCristina, V., "A Prediction Technique for Ablative Material Performance Under High-Shear Reentry Conditions," AIAA Journal, Vol. 6, No. 1, p. 59-63, January 1968.

4-7. Powars, C. A., "Reduced Data Report: Fall 1971 AFML/SAMSO Ablation Tests in the AFFDL 50 MW Arc (U)," AFML TR-33-31, Vol. I, Aerotherm Report 72-58, (Confidential) August 1972.

4-8. Shimizn, A. B., Ferrel, J. E., and Powars, C. A., "Interim Report Passive Nosetip Technology (PANT) Program, Vol. XII, Nosetip Transition and Shape Change Tests in the AFFDL 50 MW Rent Arc, Data Report," SAMSO-TR-74-86, Vol. XII, April 1974.

4-9. Arnold, J., Read, D., "Reduced Data Report: ADCON-3 Nosetip Ablation Test Series in the AFWAL/AFFDL Rent 50 MW Arc Heater Facility," Acurex Report TM-78-218, June 1978.

4-10. Howe, J. T., "Thermal-Mechanical Response to Nearly Opaque Materials Exposed to Continuous Radiation," AIAA Journal, Vol. 9, No. 10, p. 1911-1920, October 1971.

4-11. Mathieu, R. D., "Mechanical Spallation of Charring Ablators in Hyperthermal Environments," AIAA Journal, Vol. 2, No. 9, p. 1621-1627, September 1964.

4-12. Kratsch, K. M., Loomis, W. C., and Randles, P. W., "Jupiter Probe Heatshield Design," AIAA Paper No. 77-427, March 1977.

4-13. Moss, J. N., Anderson, E. C., and Bolz, C. W., "Viscous-Shock-Layer Solutions with Radiation and Ablation Injection for Jovian Entry," AIAA Paper No. 75-671, May 1975.

4-14. Powars, C. A., and Kendall, R. M., "User's Manual, Aerotherm Chemical Equilibrium (ACE) Computer Program," UM-69-7, Aerotherm Corporation, Mountain View, California, May 1969.

4-15. Rindal, R. A., Dahm, T. J., and McVey, D. F., "Graphite Temperature and Ablation Characteristics in Various Environments," AIAA Paper No. 69-148, January 1969.

4-16. Zoby, E. V., "Empirical Stagnation Point Heat transfer Relation in Several Gas Mixtures at High Enthalpy Levels," NASA TN-D-4799.

SECTION 5

GRAPHITIC HEATSHIELD SPECIMENS

The entry conditions into the Jovian environment are so severe that there is doubt about the survivability of the baseline carbon-phenolic heatshield material. In addition, the probe is weight critical as a result of the required, but excessive, heatshield weight. The concern about the severe reentry conditions and the excessive weight of the heatshield prompted a recommendation to investigate newly developed metal containing carbon-carbon materials.

The data resulting from an extensive investigation of the thermal response of various types of ablative materials was available for comparison. The materials which had been investigated included many parametric variations of the following types:

1. 2-D carbon-phenolic composites
2. 2-D carbon-phenolic composites
3. 2-D carbon-carbon composites
4. 3-D carbon-carbon composites
5. Bulk graphite
6. Pyrolytic graphite
7. Graphitized metal containing carbon-carbon composites

A study of movies of the heated materials indicated that resistance to spallation, microcracking and fracture was the order:

(7) >> (6) ~ (4) > (3) > (5) > (2) ~ (1)

A study of the effective heats of ablation of the same classes of materials indicated:

(7) >> (6) > (5) ~ (4) > (3) > (2) ~ (1)

The superior thermomechanical and ablative properties provided a basis for recommending the investigation of metal containing carbon-carbon materials for the Jupiter Probe heatshield.

The objective of this study was to assess the potential for use of metal containing carbon-carbon composites for Jovian heatshield application. This section summarizes the material selection, composite fabrication and specimen evaluation efforts which were conducted in support of this study.

5.1 SELECTION CATEGORIES

5.1.1 Material Selection

Constituent materials were selected for their potential to provide heatshield composites based on specific factors. The primary factor, the need to provide test specimens with a sufficient range in metal-matrix-reinforcement types, was to evaluate the viability of using metal containing carbon-carbon composites as heatshields. Additional factors included several significant cost factors such as raw materials, fabrication processes, and scale-up feasibility.

5.1.2 Matrix Selection

Matrices were selected to provide compatability with the metal additives and with high temperature graphitization processing. The two general matrix types considered were pitch and resins.

Pitch matrices were eliminated due to lack of prior data on the response effects of metal additions to either petroleum or coal tar type pitch based composites. Pitch matrices offer low initial cost, but the densification processing which would be required to achieve a heatshield with optimum properties would be prohibitively expensive with currently available technology.

The two resins chosen as precursors for the composite matrix were a furfuryl alcohol modified polyester and a high solids content phenolic resin. The modified polyester has been used in a series of metal bearing resins employed in composites which have been graphitized and evaluated for high energy laser response (References 5-1 and 5-2). The composites using these matrices require relatively high cost processing (2800°C under high pressure). The prior HITCO proprietary material response data provided an excellent baseline reference for the current effort.

Phenolic resins offered an excellent alternative. These resins provided a matrix with low cost acceptable char yields, and a history of prior use in carbon-carbon composites. The phenolic resins most widely used for carbon-carbon composites are SC-1008 and FF-17. These phenolic resins are compared in Table 5-1 (References 5-3 and 5-4).

FF-17 was selected as the phenolic resin for use in this task. Selection was based on two factors: first, the high solids content of the FF-17 permitted simplified processing to achieve acceptable quality laminates; second, as discussed in Section 5.2, FF-17 provided significant advantages in its shrinkage characteristics during graphitization processing.

Table 5-1. Candidate Phenolic Matrix Resins

Parameter	SC-1008[a]	FF-17[b]
Viscosity (cps)	180 - 300	2000 - 3000[c]
Gel time (@ 170°C/min)	--	5 - 6
Solids content (percent)	60 - 64	98 minimum
Solvent required	Alcohol	None
Char yield (percent)	~45	~45

[a] Monsanto Chemical Corporation phenolic resin
[b] Ironsides Resin Company phenolic resin
[c] At 71°C

5.1.3 Reinforcements

Two polyacrylonitrile (PAN) precursor based graphite fabrics were selected for use with FF-17 resin in the Task 9 composites. The first fabric selected was SWB-8. This fabric uses long staple PAN fiber. SWB-8 was used in those composites incorporating the metal containing modified polyester matrix. The discontinuous, staple fiber used as the precursor in SWB-8 can result in less shrink stresses which normally arise during graphitization but might not provide optimum composite strength.

The second fabric was Style W-1177. This fabric is a PAN filament based fabric woven of continuous Celion graphite fiber. W-1177 is a specialty woven fabric having a highly unbalanced weave with ~90 percent of the reinforcing fibers in the warp direction. This construction provides high strength levels.

Table 5-2 summarizes the properties of the fabrics used for the fabrication of specimens.

Table 5-2. Heatshield Specimen Reinforcements

Parameter	Fabric Identity	
	SWB-8	W-1177
Weave	8 Harness Satin	8 Harness Satin
Construction (yarns/cm)	15 x 15[a]	12 x 2[b]
Thickness (cm)	0.073	0.025
Weight (g/m^2)	260	238

[a] Warp x Fill
[b] 3000 filament Celion in warp; 1000 filament Celion in fill

5.1.4 Metal and Graphite Additives

Various metals and metal compounds of the transition metal series were considered as potential starting materials to obtaining metal containing carbon-carbon composites. The compounds included oxides, carbides, nitrides and halides. As discussed in Section 5.2 tungstic oxide (WO_3) was selected as the metal compound. The primary reasons for the selection of tungstic oxide included compatability with the selected FF-17 phenolic resin during laminate cure and postcure and thermal stability during carbonization/graphitization to the point of conversion to tungsten carbide.

Asbury 3376 graphite was added to the composite constituents as a fine, high purity particulate. This graphite was incorporated to provide a source of carbon in addition to the FF-17 phenolic resin for the reaction $WO_3 + 4C \rightarrow WC + 3CO$. This additive has been used in previous programs. Table 5-3 summarizes the properties of Asbury 3376 graphite.

These materials were employed in fabrication of composites for this program as discussed below.

Table 5-3. Properties of Particulate Graphite

Designation	3376[a]
Carbon content (percent)	99
Average particle size (microns)	0.75
Density (g/cm^3)	2.22

[a] Product of Asbury Graphite, Incorporated

5.2 FABRICATON

Six composites were fabricated to provide high energy laser, thermal conductivity and arc heater ablation specimens. These composites were fabricated using the constituents described in the previous section. A detailed description of the characterizations and processes used in phenolic matrix composite fabrication is presented.

5.2.1 Composites Based on a Modified Polyester

Composites based on modified polyesters matrix were procured from HITCO, Gardena, California. Three of the composites contained metals; one each tungsten, molybdenum and tungsten with metal boride. A fourth composite was provided without metal constituents to serve as a baseline.

As noted in Section 5.1, the matrix used in these composites is a proprietary product. The fabrication process for the composites includes graphitization at 2800^{o}C under high pressure. The physical properties of the fully graphitized composites are summarized at the conclusion of Section 5.2.2

5.2.2 Composites Based on a Phenolic Matrix

This section discusses the fabrication efforts conducted on metal containing phenolic matrix composites. The discussion includes resin characterization, metal compound-phenolic resin compatability assessment, prepreg-process development studies and the final fabrication methods used in preparing graphitized carbon-carbon composites.

Resin Characterization

A limited characterization of the FF-17 phenolic resin was conducted to verify the critical temperature ranges for curing and to establish baseline data for the char forming characteristics of the matrix resin. Characterization was conducted using differential scanning calorimeter (DSC) and thermogravimetric analyses (TGA). The results were used to provide guidance for cure methods to be used in composite fabrication.

The results of the DSC analysis confirmed that the predominant cure reaction occurred between 125°C and 200°C with a peak exotherm occurring at 170°C (Figure 5-1). The TGA results indicate that volatiles were released within the same temperature range (Figure 5-2). Figure 5-2 also identifies 350°C as the temperature for the onset of thermal degradation of the FF-17 phenolic resin.

The TGA data were obtained in a static air environment. Since high temperature postcures were anticipated, this data confirmed the need for maintaining an inert atmosphere curing postcure.

The DSC and TGA results identified the critical temperature ranges for cure and postcure.

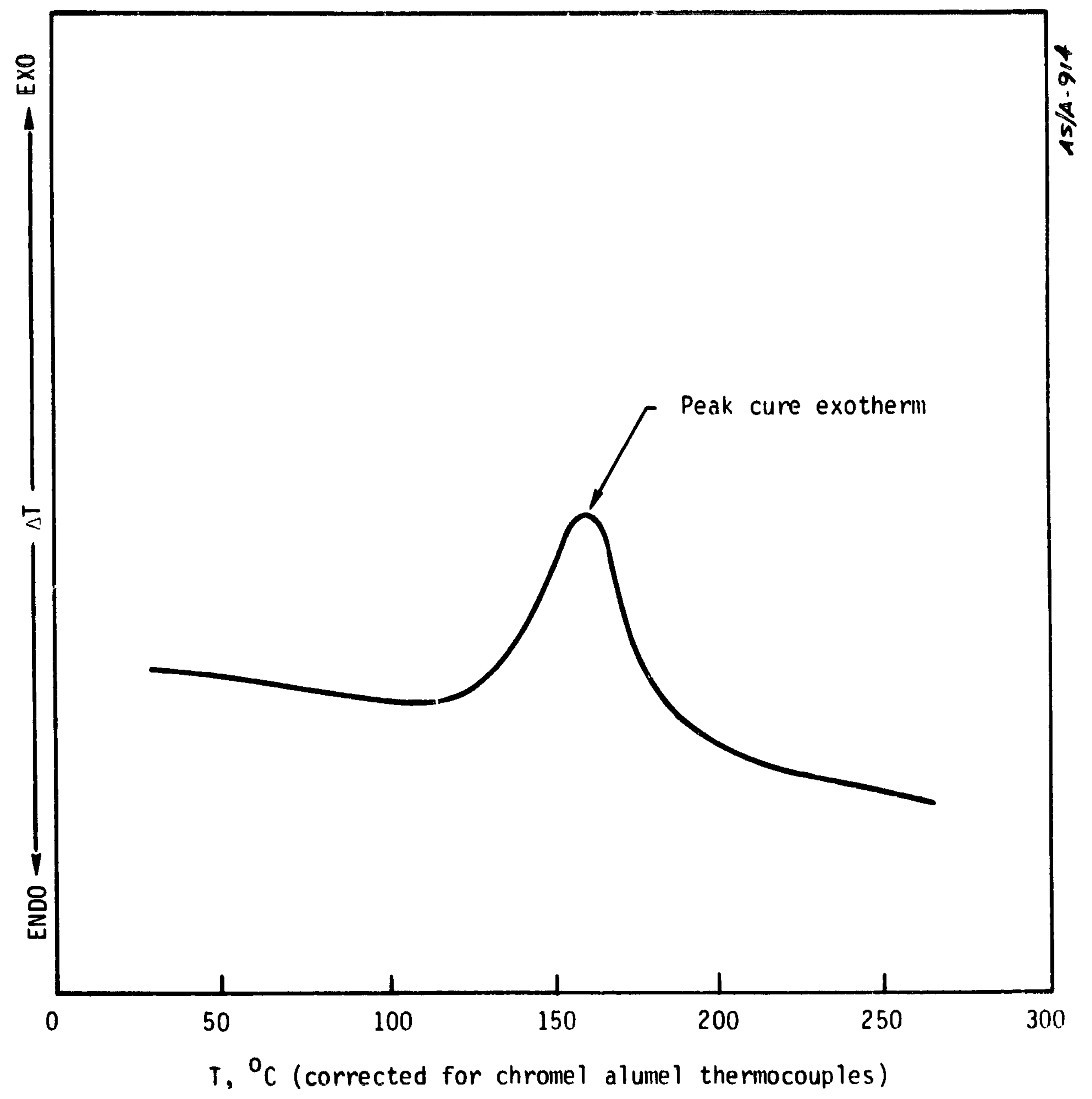

Figure 5-1. DSC Analysis of FF-17 Phenolic Resin (3°C/min)

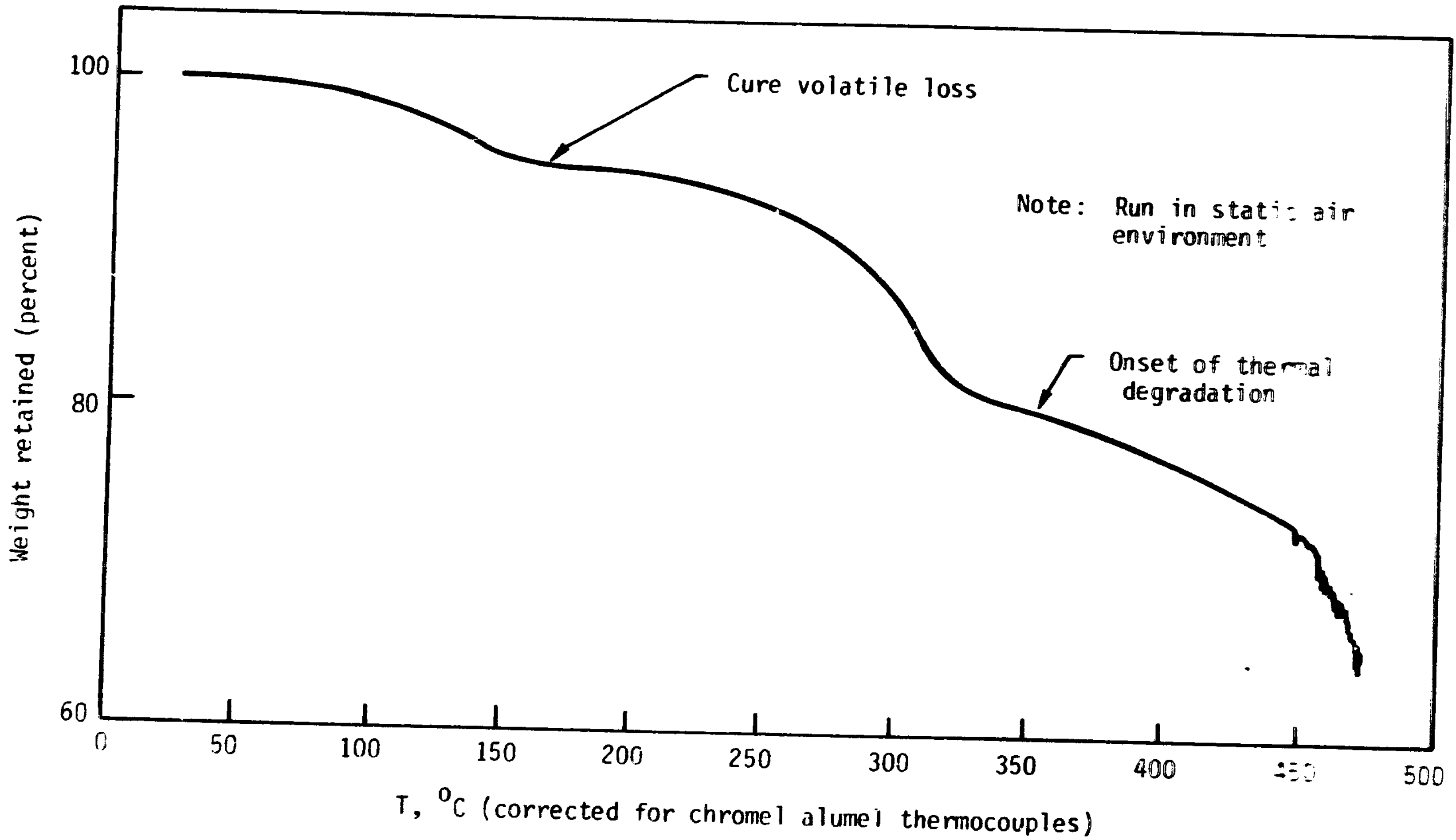

ASA-915

Figure 5-2. TGA Curve for FF-17 Phenolic Resin (3°/min)

Metal Compound-Phenolic Resin Compatability Assessment

As discussed in Section 5.1, WO_3 was selected as the metal compound for use in the phenolic matrix composites fabricated under this task. Some of the factors which led to selection of WO_3 were discussed in this preceding section. Additional factors are identified in the discussion below.

For high quality composites to be fabricated from metal compound-phenolic constituents, chemical and processing compatability is required. The approach used to assess and verify the compatability of these constituents was to mix candidate metal compounds with the FF-17 phenolic resin and subject the mixture to a programmed time-temperature cycle representative of that anticipated for the end item composite. Compatability was judged by the presence or absence of chemical reaction as evidenced by foaming and significant weight loss. Those candidate metal compound-resin mixtures were considered compatable which exhibited no foaming or weight loss above that resulting from volatile emission during resin cure. Mixtures were prepared by blending on a 3 roll paint mill. The blended mixtures were placed in individual foil cups. The cups were placed in an air circulating oven preheated to 71°C. The oven was then heated to 110°C over 3 hr and the temperature then increased at 30°C/min to 170°C. After visual evaluation and weight changes were recorded, selected samples were subjected to a 14 hr 170°C postcure to evaluate the effects of longer cure cycles.

Baseline samples of FF-17 resin with no filler and FF-17 resin with only Asbury 3376 fillers were included. Metal compounds screened included MoO_3, MoC, Mo_2C, MoO_2, WO_3, WO_2, and V_2O_3. Table 5-4 summarizes the weight changes and visual observations which resulted from this exposure.

c-2

Based on the above cited criteria and the data presented in Table 5-4, tungstic oxide (WO_3) was considered to be the most compatable metal compound meeting the ultimate objective of fabricating specimens representative of heatshield materials. Tungstic oxide was chosen over Mo_2C, which exhibited lower weight loss, for two major reasons: (1) there was extensive data for tungsten containing composites derived from modified polyester resins, and (2) there was evidence available which indicated the in-situ formation of the tungsten carbide provided a uniform distribution which was considered desirable for a heatshield.

Table 5-4. Metal Compound FF-17 Compatability Evaluation

Sample Identity	Mixture	Initial Weight (g)	Cured Weight Change (%)	Postcured[a] Weight Change (%)
5-1	FF-17	21.535	-0.92[e]	-1.51
7-4	FF-17 + MoO_3	36.515	-2.89[d]	c
7-5	FF-17 + 3376[b]	36.159	-0.50	-
7-4	FF-17 + MoO_3 + 3376[b]	36.720	-2.76[d]	c
8-8	FF-17 + MoO_2	21.331	-0.87	-1.56
8-9	FF-17 + WO_3	21.433	-0.77	-1.54
8-10	FF-17 + WO_2	21.557	-0.83	-
8-11	FF-17 + V_2O_3	21.468	-0.82[d]	-1.84
8-12	FF-17 + Mo_2C	21.309	-0.72	-1.39

[a] Based on initial weight
[b] Asbury 3376 graphite powder
[c] Not postcured due to high weight loss during cure
[d] Extensive foaming noted
[e] Clear, void free casting

Prepreg-Process Evaluation

The cure characteristics and metal compound-phenolic resin compatability were described previously in this section. A definition of the response of the prepreg to cure and postcure processing and of the resulting laminate to high temperature processing was required prior to fabrication of the composites from which test specimens would be obtained.

The approach taken to defining the interrelationships between prepreg, laminate processing, laminate properties and high temperature processing involved the following steps:

- Prepare a series of prepreg batches with variations in matrix pickup (FF-17, WO_3 and Asbury 3376)
- Use the prepreg batches to prepare three composites for cure
- Vary the cure and postcure parameters for these composites
- Determine the physical properties of these composites
- Remove sections from each composite
- Pyrolyze the sections and redetermine the physical properties

The weight loss, density and linear shrinkage of FF-17 when exposed to high temperature was available (Reference 5-5). The weight loss, bulk density and linear shrinkage of FF-17 is essentially complete at 649°C as noted in Reference 5-5. Consequently, this information led to exposure of the composite sections to an inert atmosphere to the following cycle: 23°C to 274°C in 5 hr, 274°C to 816°C in 8.5 hr, held at 816°C for 1 hr. The samples were then cooled to 23°C in the inert atmosphere.

The key result of this assessment was that maximum density, reduced porosity and minimum shrinkage was obtained when prepreg pickup was maintained at approximately 51 percent. The prepreg batches were deliberately fabricated to achieve a high (70 percent) pickup and a lower

(51 percent) pickup range. As shown in Table 5-5, the composite fabricated from the lower pickup prepreg had a 7.34 percent reduction in thickness due to shrinkage in pyrolysis. This is contrasted with a 19 percent reduction in thickness for the composite fabricated from the 70 percent pickup prepreg.

Composite Fabrication

Figure 5-3 summarizes the fabrication processes used for the composites for thermal conductivity, arc heater and high energy laser test specimens.

Prepreg production was successfully accomplished to provide materials for the composite layup. Typical resin pickup for various batches of prepreg is shown in Figures 5-4 and 5-5. These figures summarize the results of a study conducted to establish the proper staging for the prepreg based on a mixture of FF-17, tungstic oxide, and Asbury 3376 an W-1177 fabric. The staging conditions employed for the pie prepreg used for composite fabrication were extended time at elevated temperatures to achieve reduced prepreg volatile content and gel time.

The staged prepreg was then cut into individual plys. The plys were stacked into a mold and cured in accordance with the time, temperature and pressures shown in Figure 5-6.

Figure 5-7 summarizes the postcure cycle used for the metal containing carbon-carbon composites. Laminate properties including density, thickness, and open porosity were determined after the cure and postcure cycles. These results are summarized at the end of Section 5.2.2.

The graphitization cycle used for the postcured composites is shown in Figure 5-8. This graphitization was conducted under low (g/cm^2) static loads applied by graphite blocks. Application of high pressures

Table 5-5. Physical Changes with Processing

Laminate Identity	Prepreg Processing				Bulk Density (gm/cm^3)		Open Porosity (%)		Thickness		
	Pick-up (%)	Gel (Min at 325^{o}F)	Cure Pressure (KN/m^2)	Postcure Time/temp/pressure (hr) (^{o}C) (KN/m^2)	Post Cured	Carbon-ized	Post Cured	Carbon-ized	Cured	Post Cured	Carbon-ized
COMPLETE COMPOSITE											
36-17	70	2.6	689	26 / 149 / 1387+ 41 / 232 / 1387	1.384	--	--	--	3.74	3.44	--
36-25	68	1.4	2067	16 / 177 / 2067+ 40 / 288 / 2067	1.442	--	--	--	3.24	2.96	--
36-28	52	1.7	2067	16 / 163 / 2067+ 40 / 288 / 2067	1.537	--	--	--	2.08	1.98	--
COMPOSITE SECTION											
36-17	a	a	a	a	1.394	1.516	3.890	24.985	--	3.45	2.97[b]
36-25	↓	↓	↓	↓	1.452	1.549	1.797	21.185	--	3.21	2.58[c]
36-28	↓	↓	↓	↓	1.518	1.508	2.887	16.351	--	1.98	1.83[d]

[a] Same as above
[b] 19 percent shrinkage in thickness
[c] 13 percent shrinkage in thickness
[d] 7.3 percent shrinkage in thickness

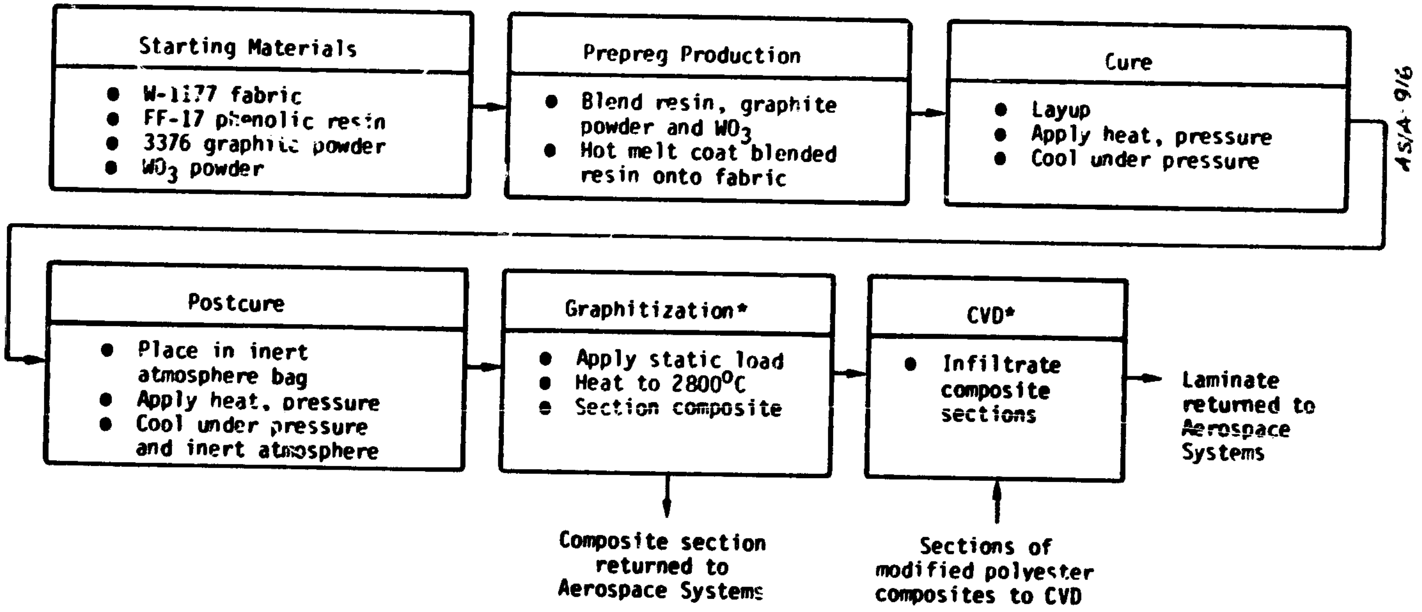

*Conducted at Supertemp

Figure 5-3. Composite Fabrication Summary

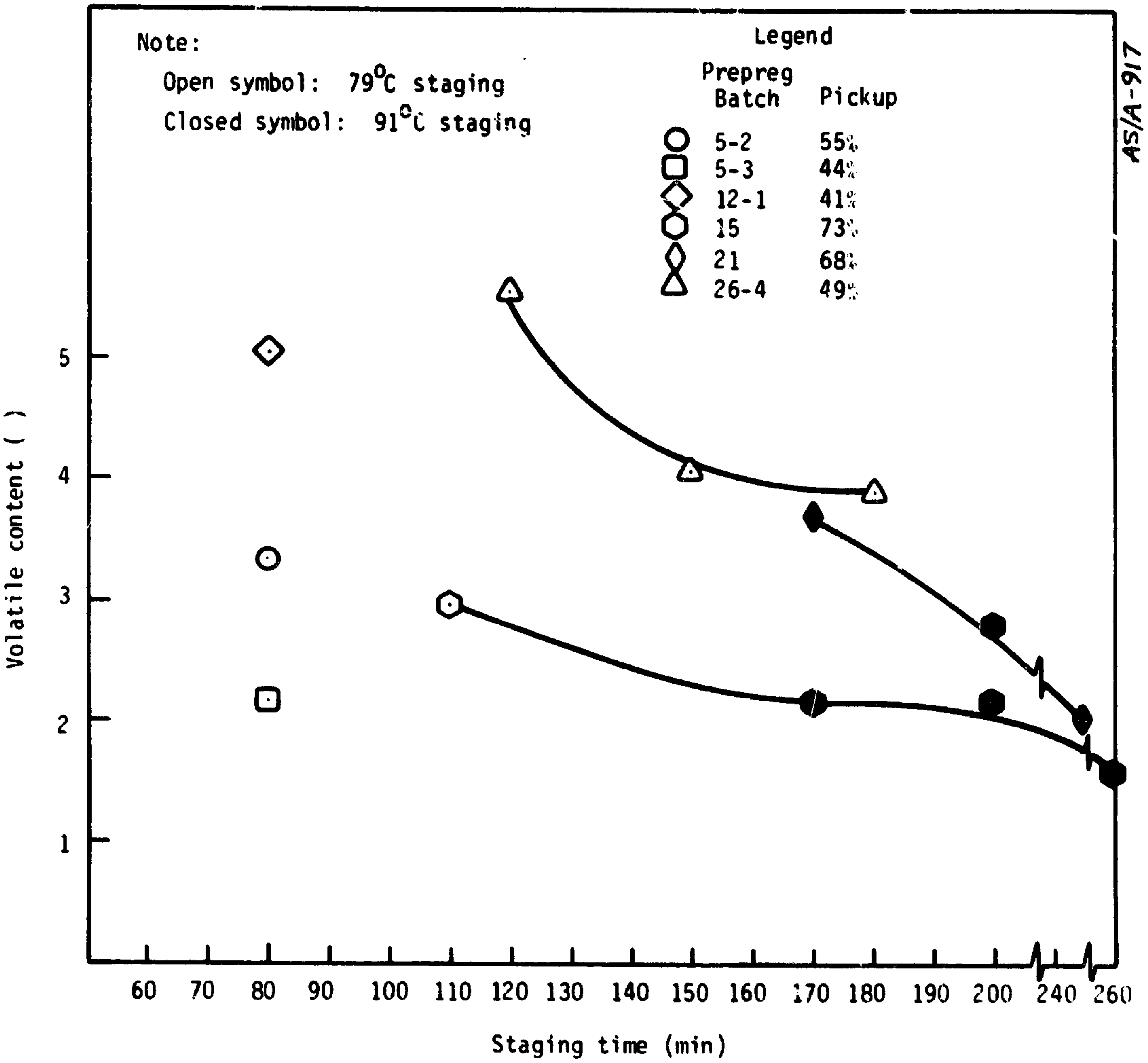

Figure 5-4. Prepreg Volatile Content Variation with Staging Parameters

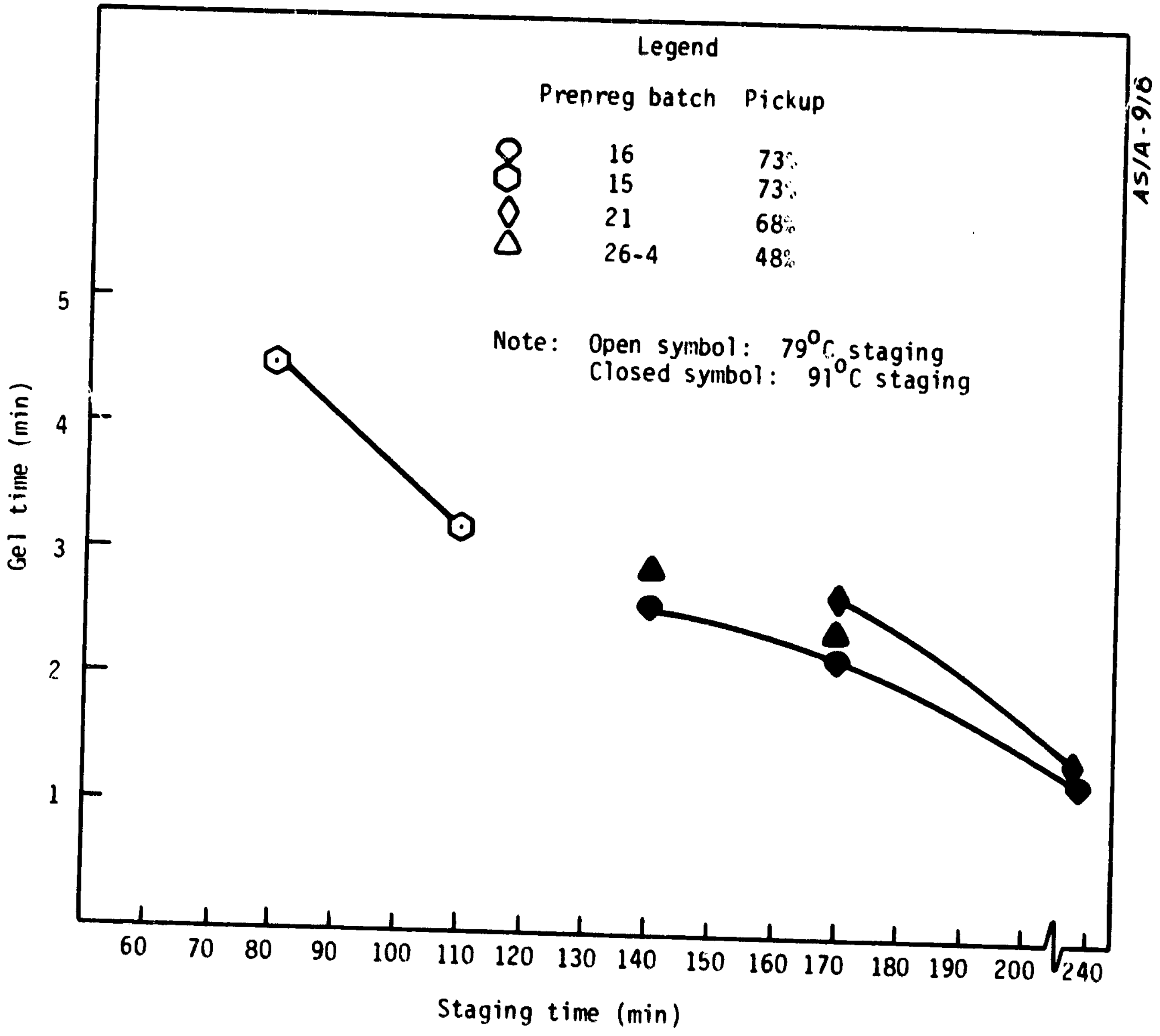

Figure 5-5. Prepreg Gel Time Variation with Staging Parameters

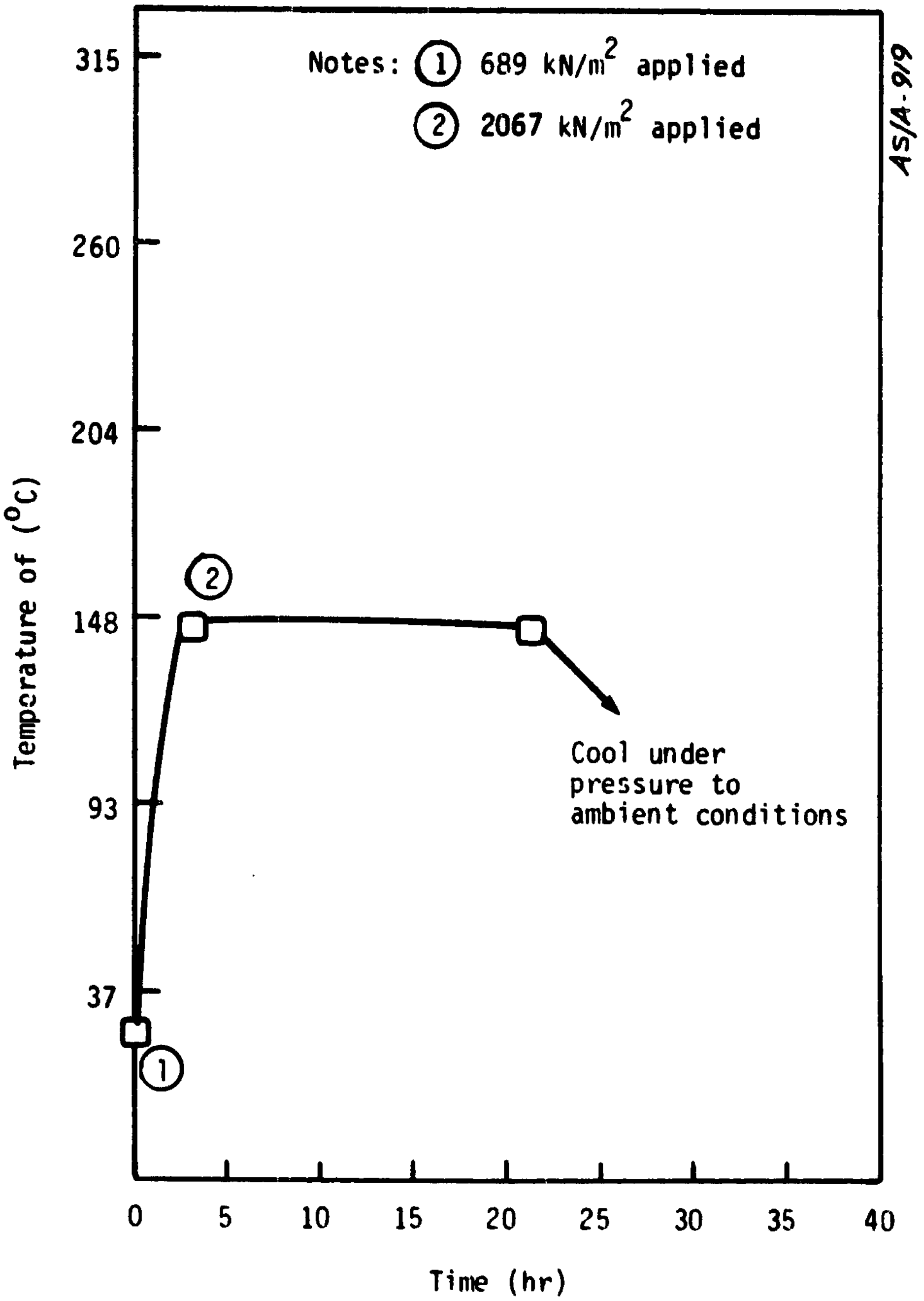

Figure 5-6. Composite Cure Cycle

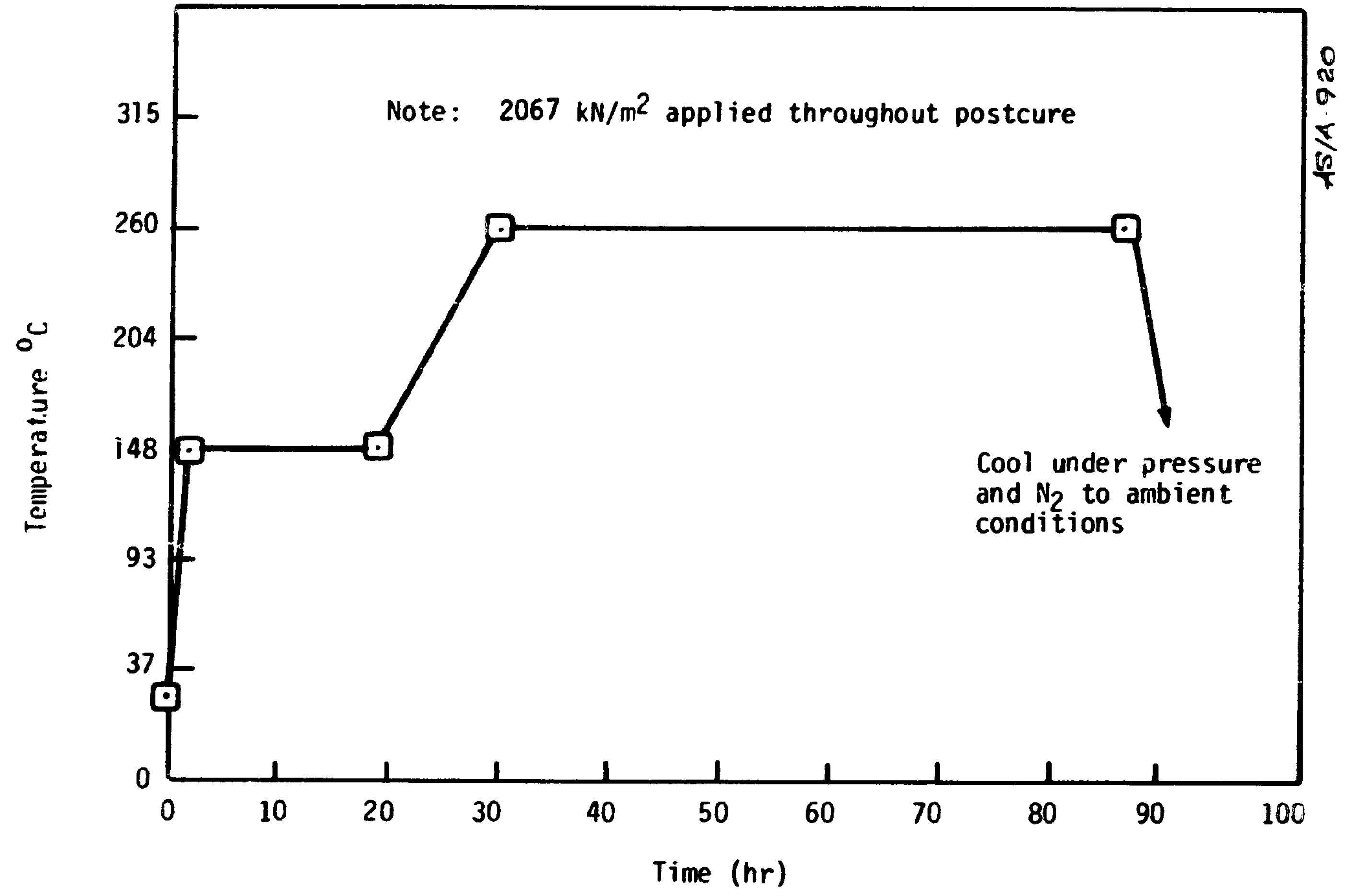

Figure 5-7. Postcure Cycle for Metal Containing Composite 6

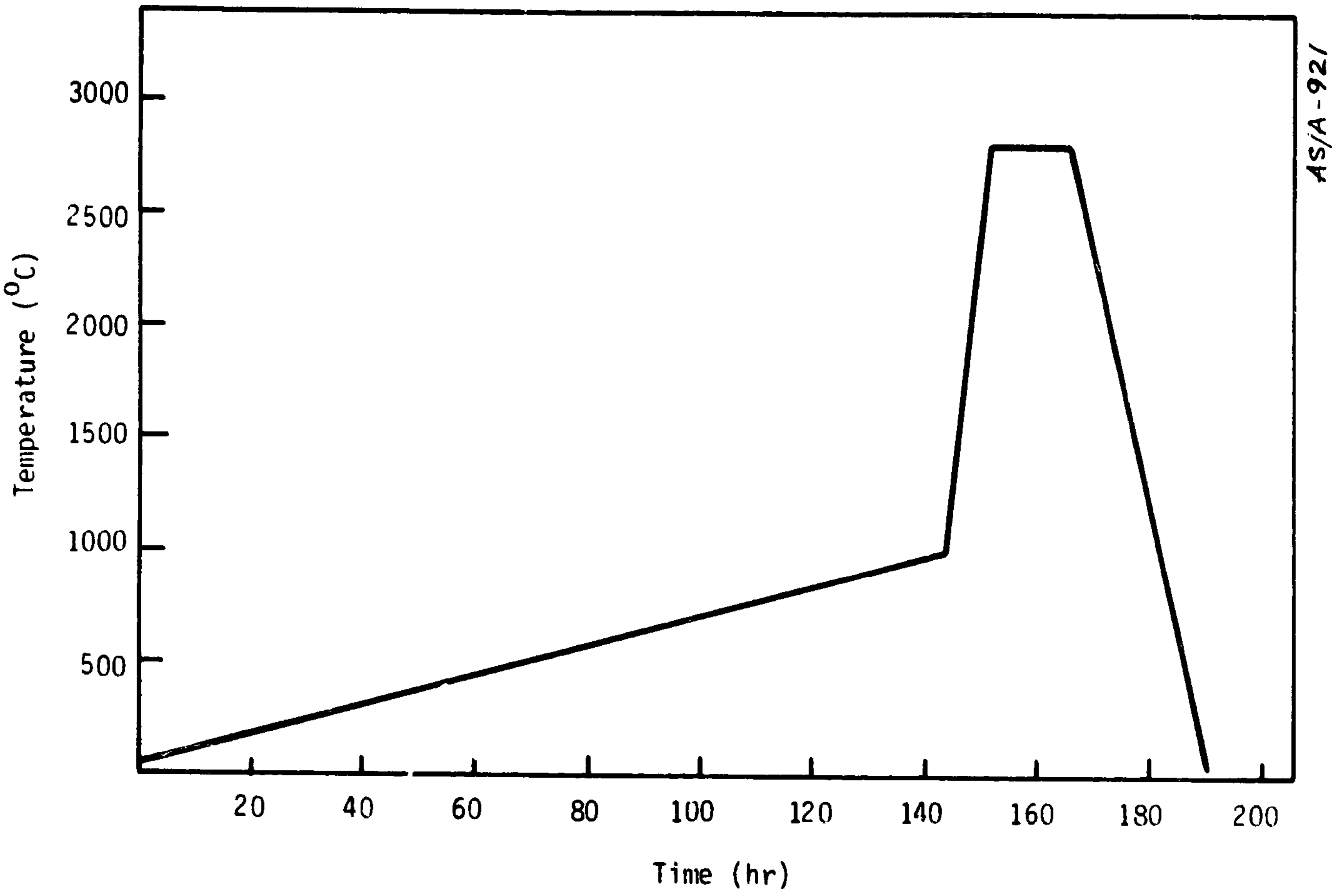

Figure 5-8. Graphitization Cycle for Composites 5 and 6

would have resulted in inherent limitations in maximum composite size and higher costs for potential heatshield application. As shown in Figure 5-3, the composites were then sectioned. One of the sections was submitted to CVD processing. The other section was used to document the as graphitized composite conditions.

Carbon vapor deposition (CVD) was then conducted on sections of each of the composites based on FF-17 matrix. Sections of each of the modified polyester based composites were included in this CVD processing.

Composite Summary

Table 5-6 summarizes the constituents for each of the composites used in this effort. Table 5-7 summarizes the final properties of each of the six composites before and after CVD processing. As shown in Table 5-7, the modified polyester based composites had significantly lower open porosities and higher densities than the FF-17 based composites after graphitization. This was expected since the polyester based composites had been graphitized under high pressure.

However, after CVD processing of the graphitized composites, the density and open porosity of the FF-17 phenolic and the modified polyester based composites were within the same range. This is considered to be of major significance for potential scale-up heatshield sized, economical composites.

5.3 COMPOSITE PERFORMANCE ASSESSMENT

Individual specimens were machined from the composites fabricated as described in Section 5.2. These specimens were intended for thermal conductivity, high energy laser and arc heater convective ablation evaluations. A specimen identity convention was adopted to provide full definition of the test type, composite source, processing history and specimen serial number. This identity convention is presented in Figure 5-9.

Table 5-6. Composite Constituent Summary

Composite Identity	Reinforcement		Precursor[a] Matrix	Additive	
	Type	Fabric Style		Type	Content[f] (%)
1	Staple PAN	SWB-8	Polyester[b]	Mo	--
2	Staple PAN	SWB-8	Polyester[b]	W[d]	--
3	Staple PAN	SWB-8	Polyester[b]	e	--
4	Staple PAN	SWB-8	Polyester[b]	W	5.3
5	Celion[a]	W-1177	Phenolic	W	4.3
6	Celion[a]	W-1177	Phenolic	W	4.3

[a] Continuous PAN graphite fiber
[b] Furfuryl alcohol modified
[c] Matrix graphitized in composite
[d] Also contains metal boride
[e] No additive
[f] Weight percent metal

Table 5-7. Effect of CVD Processing on Composites

Composite Identity	Description		Weight (g)		Density (g/cm^3)		Open Porosity (%)	
	Matrix[a]	Fabric	Before	After	Before	After	Before	After
1	Polyester/Mo	SWB-8	345	352	1.96	1.98	12.76	11.24
2	Polyester/W[c]	SWB-8	416	418	2.43	2.37	4.87	3.52
3	Polyester/–[b]	SWB-8	311	314	1.94	1.96	8.55	7.98
4	Polyester/W	SWB-8	359	361	2.09	2.08	11.80	10.64
5	Phenolic/W[c]	W-1177	289	339	1.73	1.96	24.54	11.40
6	Phenolic/W[c]	W-1177	447	548	1.72	1.83	27.44	11.04

[a] Graphitized resin/metal additive
[b] No metal additive
[c] Added to matrix as WO_2 and graphite filler
[d] With boride additive

W X Y - Z

Specimen serial number: -1, -2, etc.

Processing designator:

S = standard

P = post processed (CVD)

Composite designator:* 1, 2, 3, etc.

Test type

A = arc test

L = laser test

T = thermal conductivity test

*See Table 5-5 for constituent definition.

Figure 5-9. Specimen Identity Convention

5.3.1 Laser and Arc Heater Specimens

Ten arc heater ablation models were fully machined and mounted in model holders. These models were machined to provide a 30 degree angle between the composite laminae and the model test surface.

Additionally, 36 high energy laser test specimens were fully machined to a configuration suitable for the hole boring test mode.

5.3.2 Thermal Conductivity Assessment

Comparative thermal conductivity was determined on two representative specimens (Figure 5-10). Specimen T1P-1 is a molybdenum containing, modified polyester based specimen which had been CVD processed. Specimen T6P-1 is a tungsten containing, FF-17 phenolic-based specimen which had also been CVD processed.

Thermal conductivity was determined over a 100 to 500°C range. The specimen consisted of a 0.750 in. diameter, 0.060 in. thick disc. Conductivity measurements were conducted in a nitrogen environment.

The close agreement between the thermal conductivity results provide a further basis for considering metal containing carbon-carbon composites based on either modified polyester or phenolic resins to be viable heatshield candidates.

5.4 REFERENCES

5-1. Schaeffer, R. E., "Furfuryl Alcohol Modified Polyester Resins Containing Metal Atoms," U.S. Patent 4,087,482, May 1978.

5-2. Dodson, J. D., and Washburn, R. M., "Development of Laser Barrier Materials (U)," Contract No. N60921-78-C-0208, Acurex Final Report in preparation (SECRET).

5-3. Monsanto Polymers and Petrochemicals Company, Resinox SC-1008 Data Sheet.

5-4 Ironsides Resins, Inc., Resin FF-17, Modified Phenolic Data Sheet

5-5. Seibold, R. W., "Carbonization of Phenolic Resin," sponsored under Air Force Materials Laboratory, Contract F33615-73-C-5139.

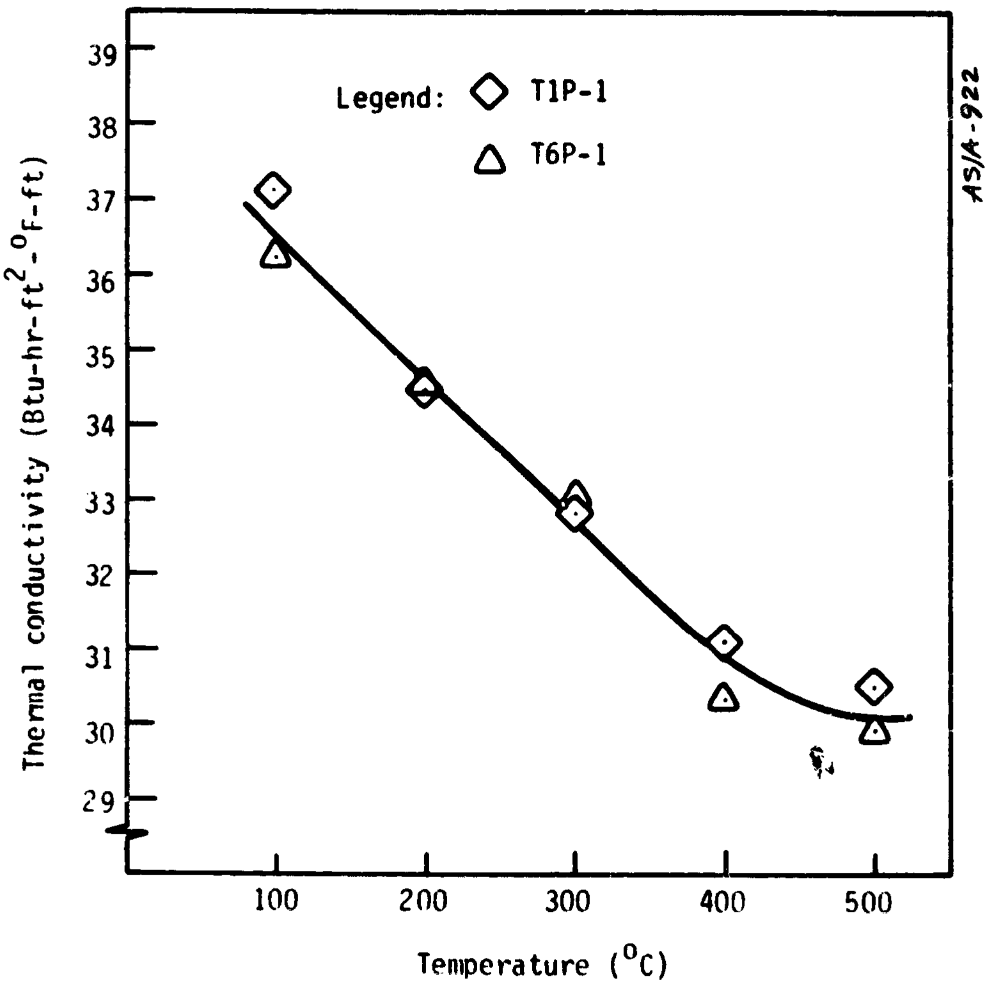

Figure 5-10. Thermal Conductivity of Speciman Materials

SECTION 6

ENTRY HEATING ENVIRONMENTS

A scientific probe entering the Jupiter atmosphere will experience extremely high heating rates, orders of magnitude higher than that encountered during manned earth entry. Previous calculations have shown that a Jupiter probe will lose approximately 25 to 40 percent of its total weight through severe forebody ablation. A comfortable margin of error in the calculations would increase the heatshield weight to the point where the probe could not carry a scientific payload.

Since the heating pulse influences the definition of the heatshield thickness, an accurate prediction of the time history of both the radiative and convective heating rates is important. Therefore, all the important factors must be included when predicting the heating rates.

Heating rates to the probe surface are influenced by the following factors:

- Atmospheric models and atmospheric structure
- Entry trajectory, including gravitational forces of the planet, rotation of the planet, and the nonspherical shape of the planet
- Atmospheric composition models, which have an effect on the thermodynamic, transport, and radiative properties
- Probe configuration, including shape, cone angle, mass, and drag coefficient

- Probe entry conditions
- Probe shape change effects

All of these factors are to be included in any heating environment calculation procedure. Recently, Balakrishnan et al. (Reference 6-1) reported a parametric study on the effect of these factors on heating rates. A recently updated atmospheric structure of the planet is used in this study, and the effect of the atmospheric structure on the convective and radiative heating is investigated.

According to Reference 6-1, the trajectory calculations performed were for a spherical planet. However, the planet Jupiter is not an exact sphere in shape; rather, it is an oblate spheriodal planet. The effect of a nonspherical shape of the planet on the entry trajectory parameters such as freestream velocity, density, altitude, and time is also studied.

The cold wall radiative heating to the wall is calculated by an approximate method in Reference 6-1. In that approach, the entire shock layer is assumed to be uniform and the conditions behind the shock are used for computing radiative heat fluxes. However, for probes that have smaller cone angles, $\theta_c = 45^o$; the assumption of uniform shock layer leads to a significant error in the heating rates. Section 3 presented the effect of entropy layer on convective heating. In this section, the effect of entropy layer which leads to nonuniform shock layer conditions are analyzed for a particular time during the trajectory.

This section is divided into three subsections. Section 6.1 presents the effect of atmospheric structure on heating rates; Section 6.2 discusses the effect of nonspherical shape of planet on entry trajectory; and Section 6.3 illustrates the influence of entropy layer on radiative heating.

6.1 EFFECT OF ATMOSPHERIC STRUCTURE ON HEATING RATES

Recently, NASA-Ames Research Center suggested new model atmospheres for Jupiter based on the data obtained by the latest Pioneer 10 and Pioneer 11 missions and earth-based experiments. The model atmospheres were proposed by Orton (Reference 6-4). Last year, NASA-Ames, on the basis of Hunten (Reference 6-3) proposed an interim model atmosphere. The parametric calculations reported in Reference 6-1 were performed with the Hunten model atmospheres. Figure 6-1 compares the pressure-altitude relationship for nominal model atmosphere proposed by Orton and Hunten. As shown, at high altitudes (above 300 km) there is a significant difference between the two models. Figure 6-2 shows the variation of temperature with altitude for the two model atmospheres. For comparison purposes, only nominal model atmosphere is considered. The two models proposed only changes to the atmospheric structure; the atmospheric composition was not altered. For example, both the models assume that the Jupiter nominal model atmosphere consists of 89 percent by volume of hydrogen and the remaining 11 percent helium.

Figure 6-3 compares the pressure-temperature relationship for the nominal model atmosphere. The Orton model is shown along with the model proposed by Hunten and an earlier atmosphere model available in Reference 6-2. As shown, significant differences exist between the three models.

The Aerotherm-developed Trajectory-Heating Environment Techniques/Analysis (THETA) (Reference 6-1) was modified to calculate the trajectory and the heating rate history. The THETA code uses input tables of altitude versus pressure, temperature and density. For the Orton model, from the table of above quantities supplied to us by NASA-Ames, the input to THETA code was constructed.

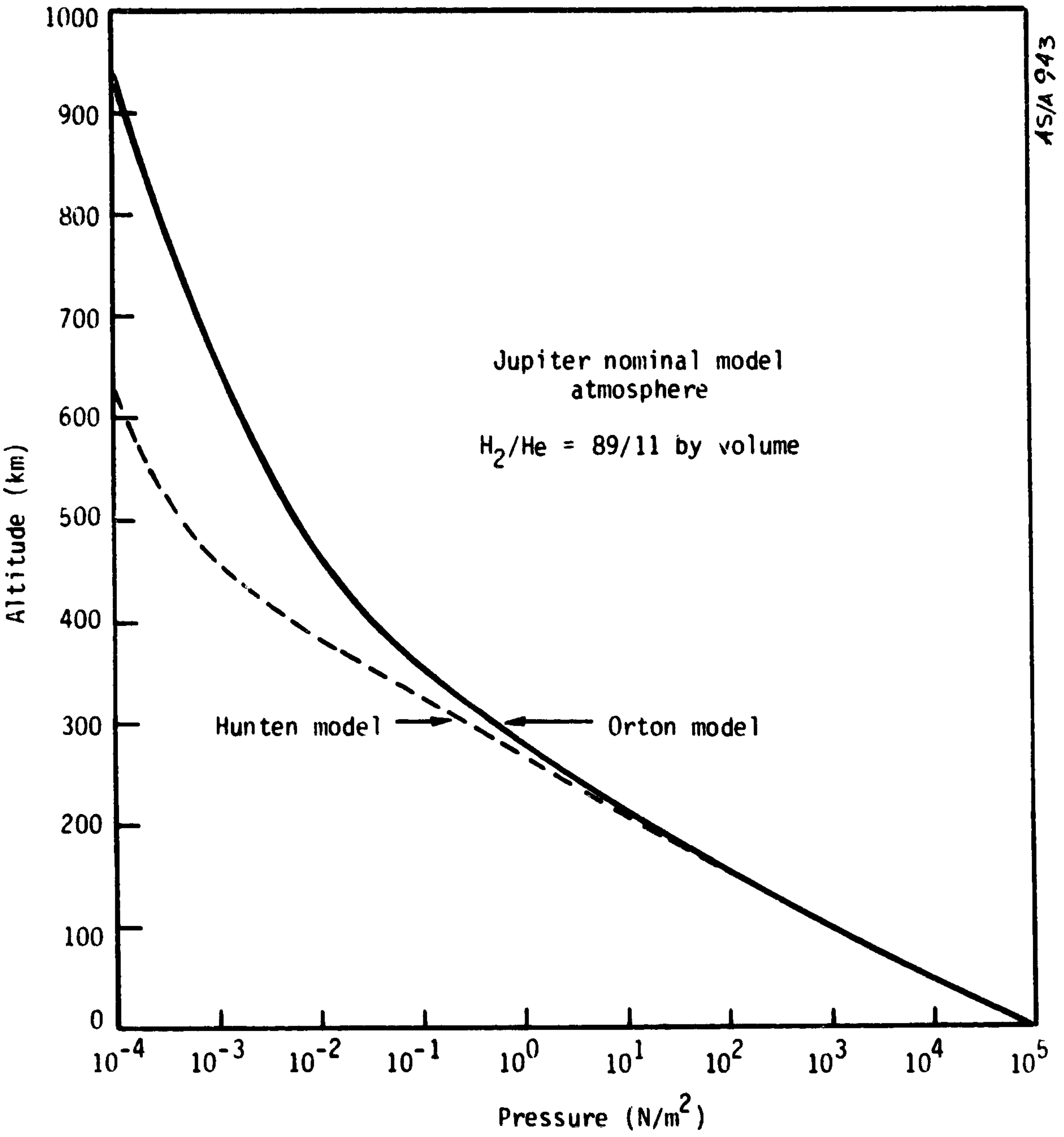

Figure 6-1. Comparison of Pressure-Altitude Relationship for Nominal Model Atmosphere

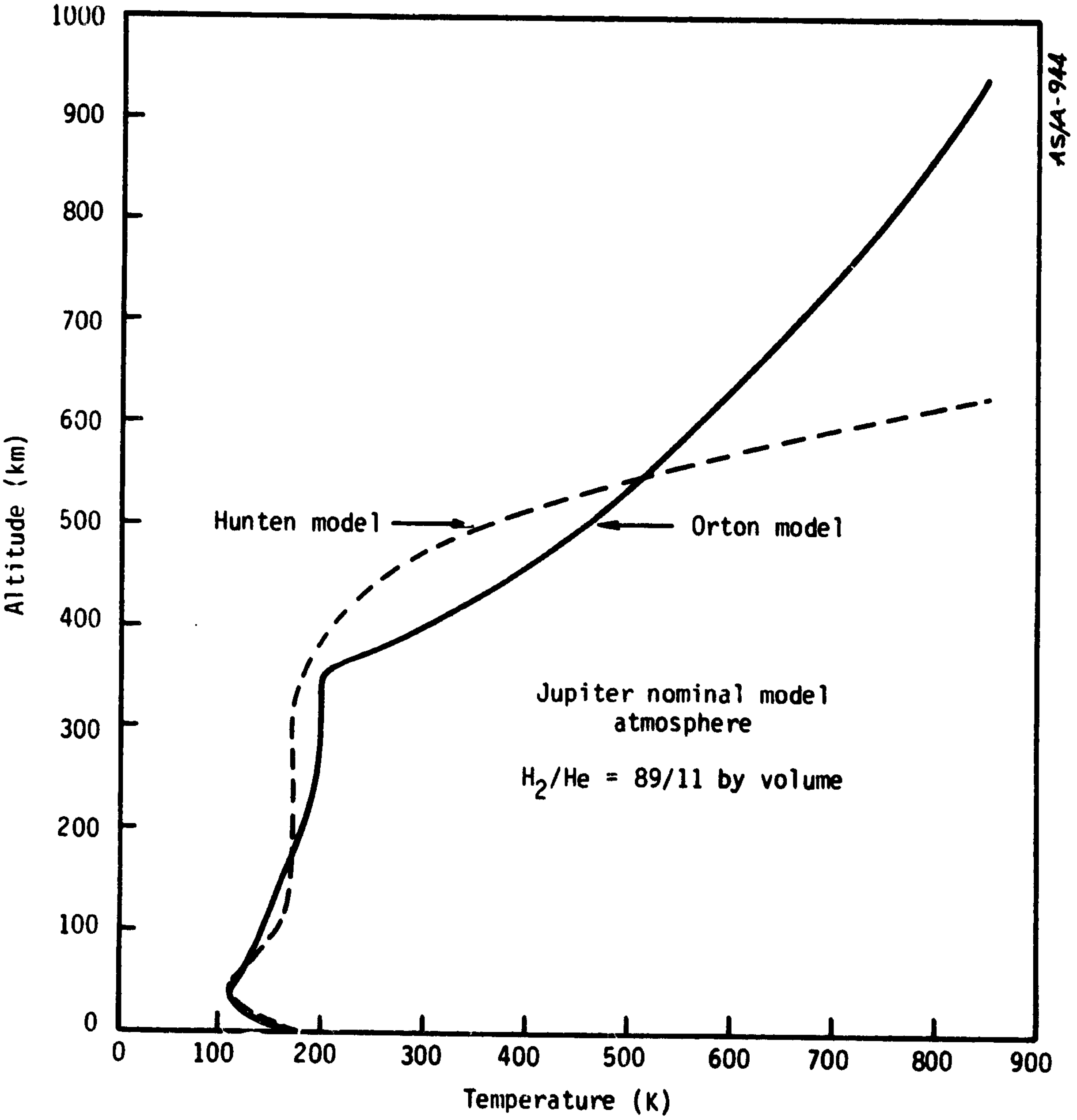

Figure 6-2. Comparison of Temperature-Altitude Relationship for Nominal Model Atmosphere

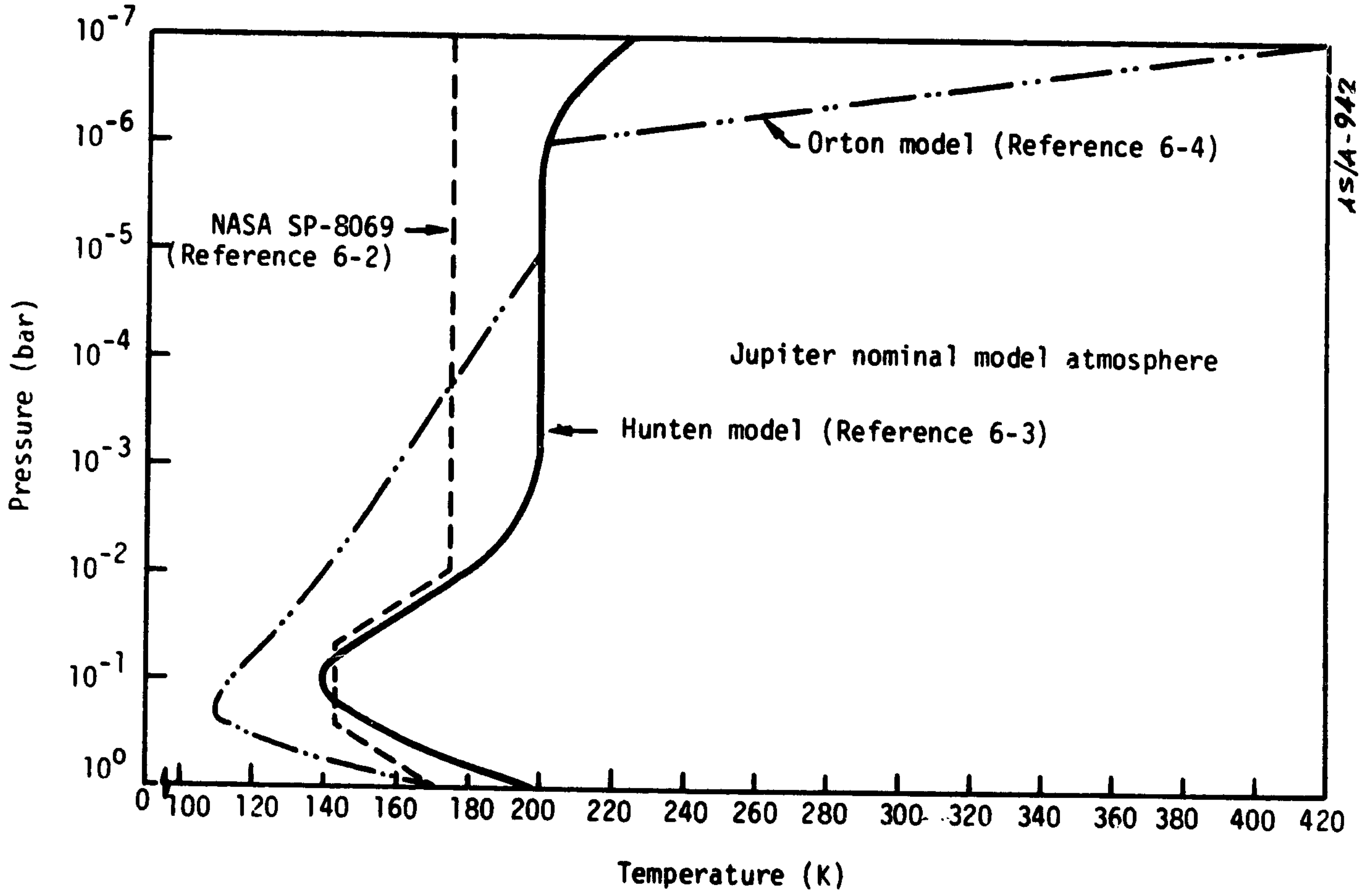

Figure 6-3. Comparison of Pressure-Temperature Data for Nominal Model Atmosphere

Figure 6-4 shows the effect of model atmosphere on the entry trajectory. Probe configuration and entry parameters were supplied by NASA-Ames. Table 3-2 summarizes the probe configuration and entry parameters used in the calculations. As shown, the effect of atmospheric structure on the trajectory parameters is rather small since, as shown in Figures 6-1 and 6-2, the model atmospheres proposed by Orton and Hunten differ significantly only above 350 km altitude. During the entry trajectory, the relative entry velocity is not affected until the probe descends to an altitude of about 400 km. Significant deceleration of the probe occurs only in the altitude region between 150 to 50 km range.

Figure 6-5 presents the effect of model atmosphere on cold wall radiative heating at the stagnation point. Figure 6-6 gives results for the convective heating rate. The calculated results show that the effect of model atmosphere structure on the heating rates is small. Only a 5 percent increase in radiative heating rate is seen; the convective heating rate increases by about 2 percent. A similar trend is noticed at other streamwise locations.

In summary, differences in the model atmospheric structure of the planet has a negligible effect on entry trajectory and on cold wall radiative and convective heating rates.

6.2 ENTRY TRAJECTORY MODIFICATIONS

The Aerotherm-developed THETA code uses a trajectory calculation scheme to estimate the local value of freestream quantities such as velocity, density, and altitude as a function of entry time. The trajectory computational procedure solves the governing equations of motion that consider gravitational effects of the atmosphere and angular rotation of the planet. Reference 6-1 describes in detail the governing

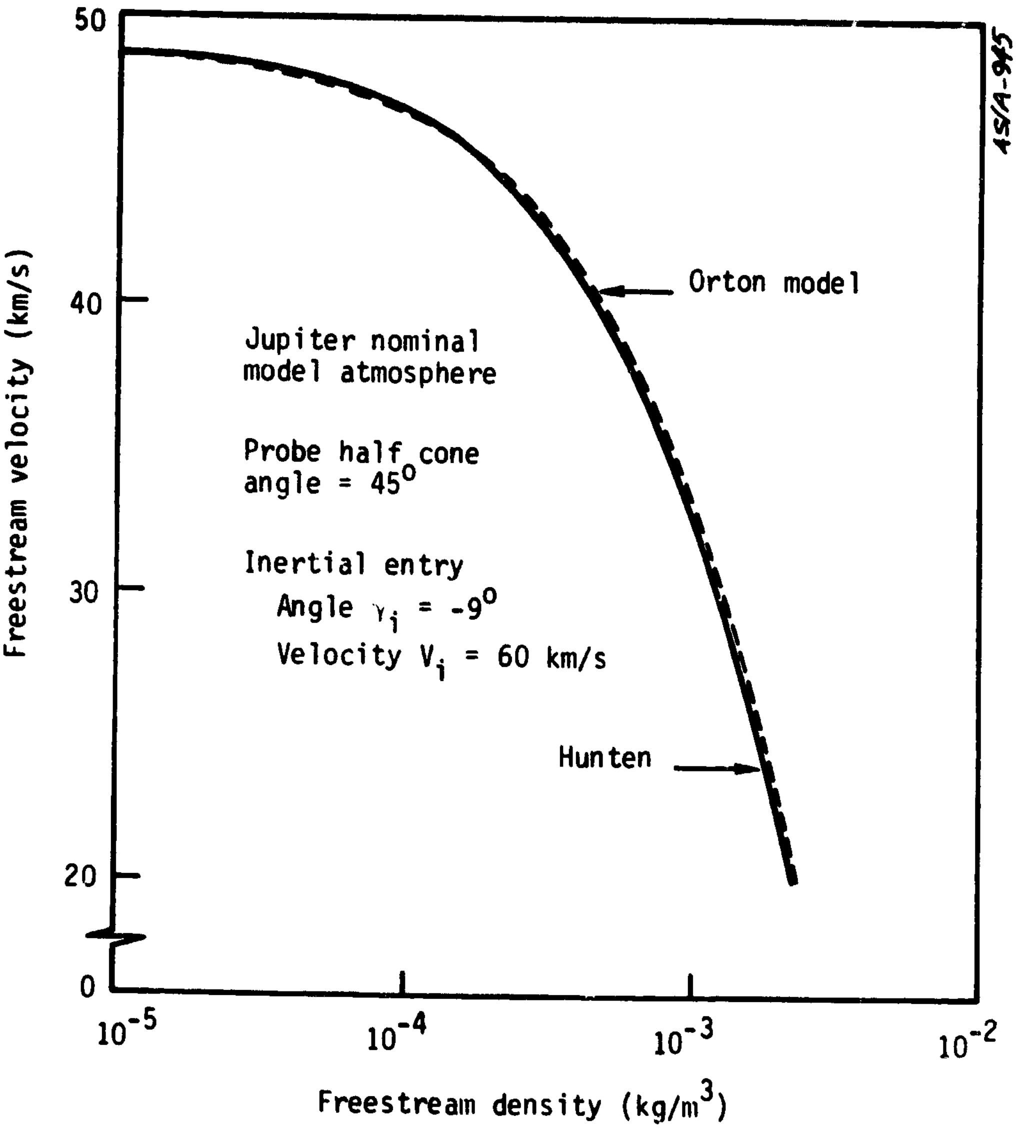

Figure 6-4. Effect of Model Atmosphere on Entry Trajectory

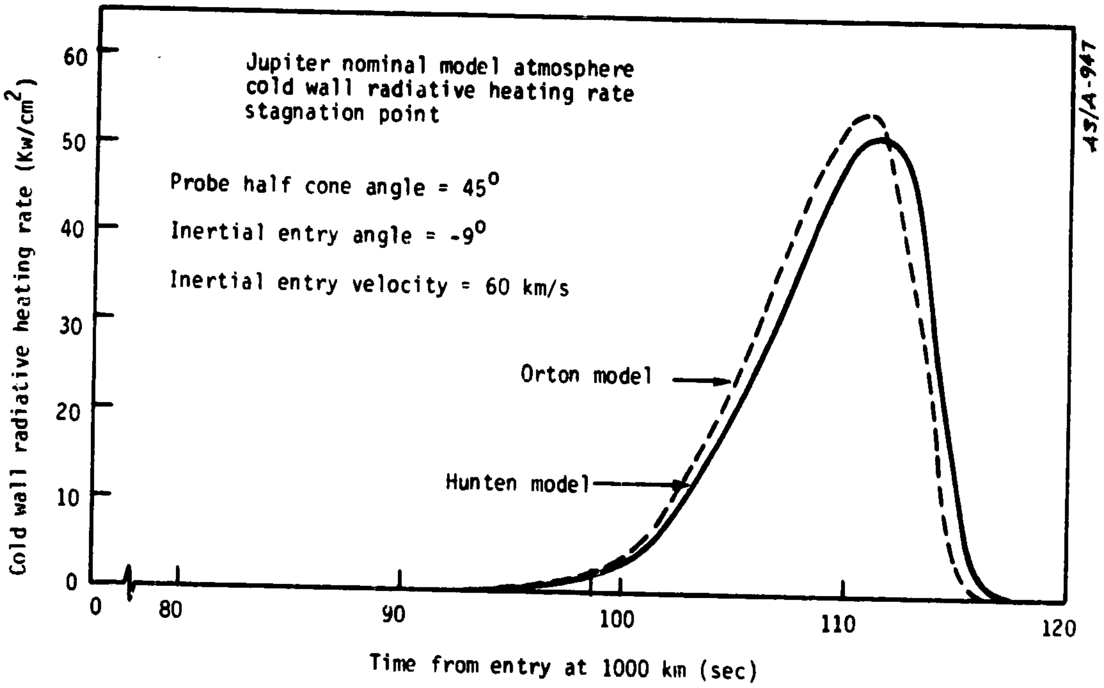

Figure 6-5. Effect of Model Atmosphere on Stagnation Point Cold Wall Radiative Heating Rate

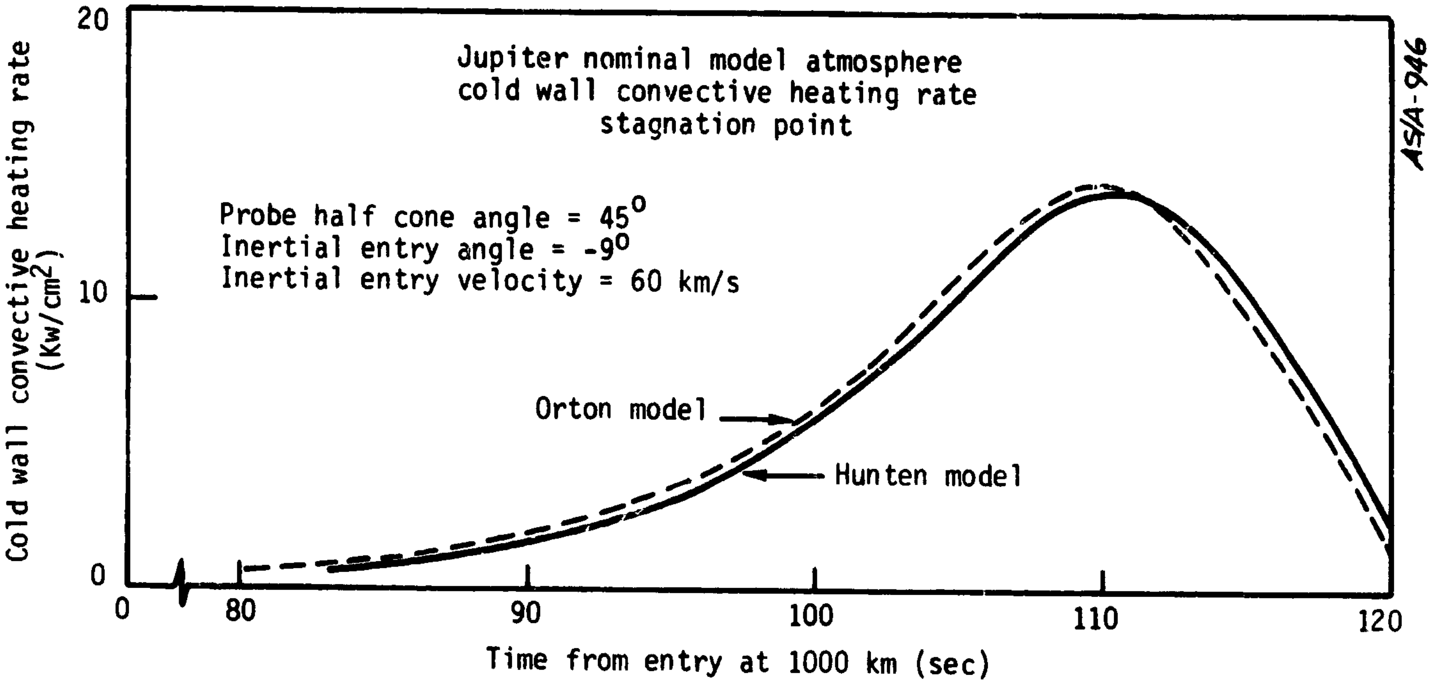

Figure 6-6. Effect of Model Atmosphere on Stagnation Point Cold Wall Convective Heating Rate

equations of motion, the solution technique, and compares the results obtained with other trajectory calculation procedures. However, the above work assumed the planet to be spherical in shape and used an effective mean radius for the planet.

It was recently shown that the above assumption introduced errors in the calculated entry quantities. This work was undertaken to modify the trajectory calculational procedure described in Reference 6-1, and to treat the planet to be an oblate spheriod.

The required modifications were rather minor. Instead of assigning a mean value for the radius of the planet, it was calculated, based on the latitude, minor and major radii of the planet. The equation used was

$$R_J = \left(\sqrt{\left(\frac{\mathrm{COS}\theta_L}{R_{major}}\right)^2 + \left(\frac{\mathrm{SIN}\theta_L}{R_{minor}}\right)^2}\right)^{-1} \qquad (6\text{-}1)$$

where θ_L is the latitude in degrees, R_{major} is the radius of the planet along the major axis, R_{minor} is the radius of the planet along the minor axis, and R_J is the radius of the planet Jupiter.

With this modification, trajectory calculations were performed for an entry into the nominal model (Orton) atmosphere. The probe configuration and entry parameters were tabulated in Table 3-2. Figures 6-7 and 6-8 show the effect of nonspherical nature of the planet on freestream velocity and density, respectively.

As shown, the spherical shape model of the planet introduces time lag in the time versus velocity/density calculations. For this particular case, the time difference between a spherical planet and nonspherical planet is roughly 6 sec. The present results given in Figures 6-7 and 6-8

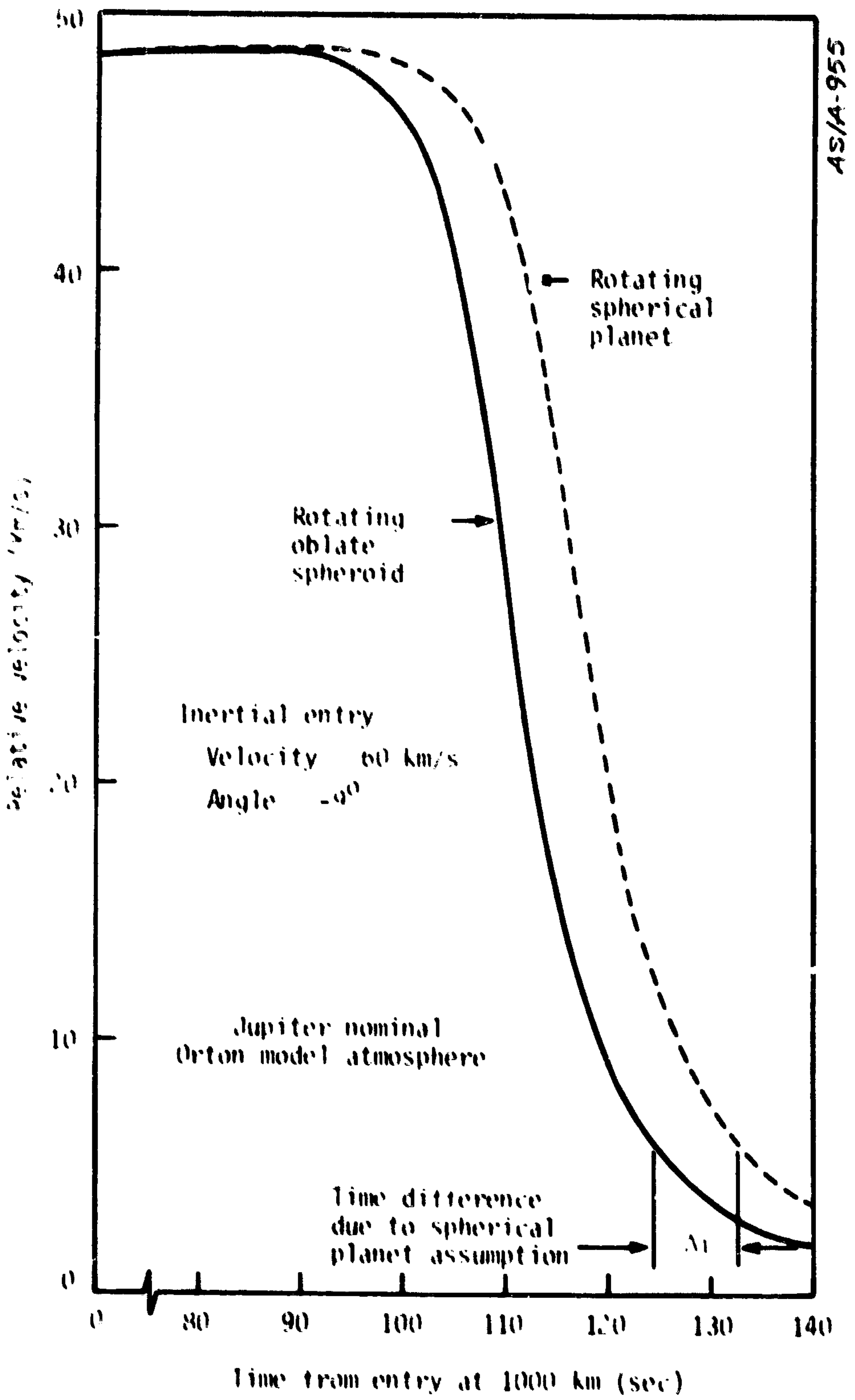

Figure 6-7. Effect of Nonspherical Nature of Planet on Trajectory-Freestream Velocity Versus Entry Time

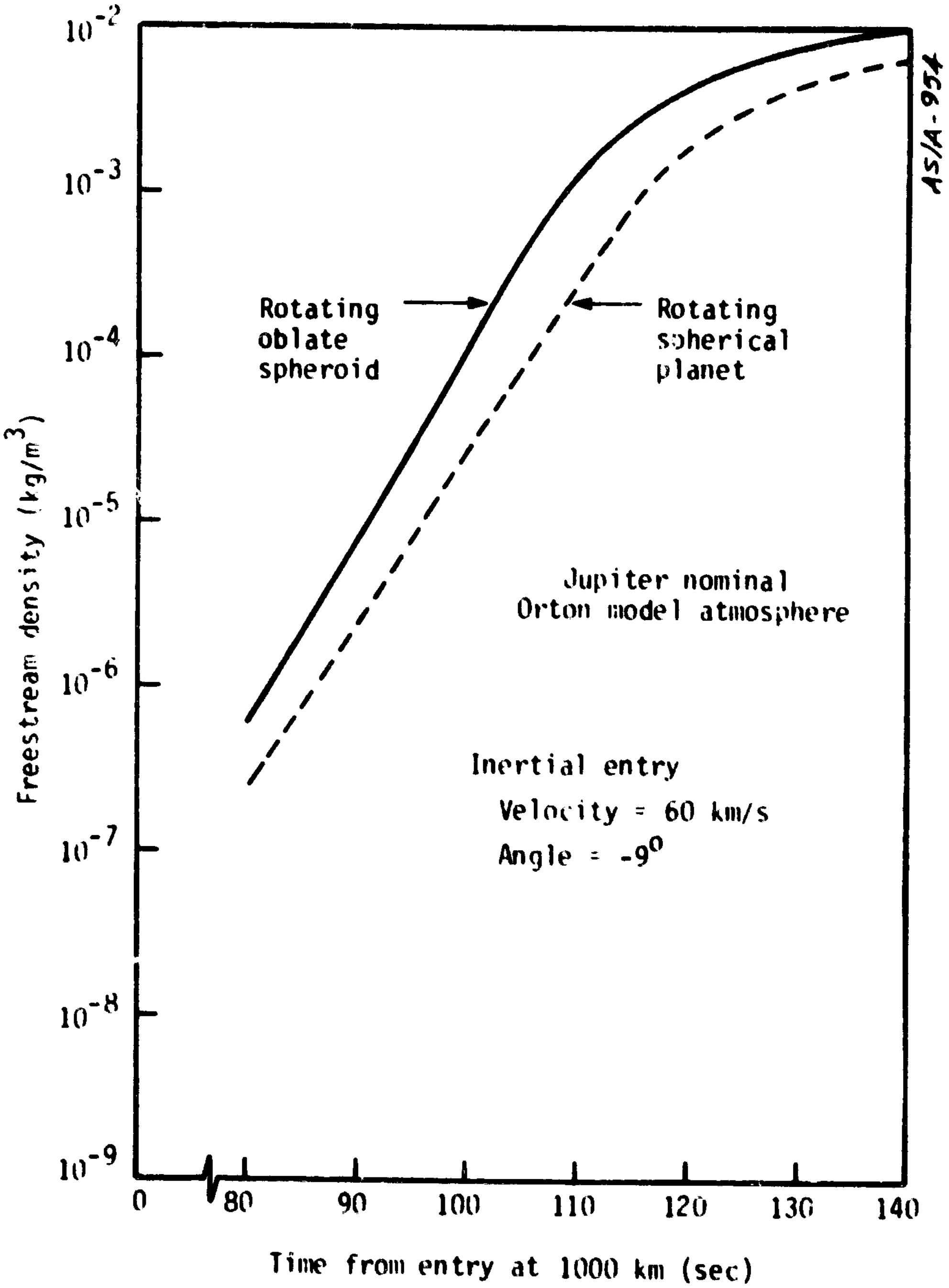

Figure 6-8. Effect of Nonspherical Nature of Planet on Entry Trajectory, Freestream Density Versus Entry Time

are compared with other trajectory calculational procedures, such as POST (Reference 6-5) where the agreement was good.

6.3 COMPARISON OF COLD WALL RADIATIVE HEATING CALCULATIONS

The cold wall radiative heating to the wall in the THETA code is caluclated by an approximate method. This method, for a particular trajectory point of interest, determines the specific shock layer conditions. These conditions, assumed to be uniform in the shock layer, are then used to obtain the radiative fluxes from a table of fluxes computed by RADICLE code (Reference 6-7). These tables are for a matrix of pressure, enthalpy, and shock standoff distances. These fluxes are then corrected for adiabatic cooling. The cooling correction factors were generated on the basis of benchmark solutions obtained by the RASLE code (Reference 6-8). However, at the time of preparation of THETA code, benchmark solutions by RASLE code was available only at the stagnation point. Therefore, the cooling corrections used in THETA code was based on stagnation point results.

Recently, benchmark solutions with the RASLE and HYVIS codes (Reference 6-6) were made available. Figure 6-9 compares the cold wall radiative heating distribution around the body calculated by the benchmark type code (HYVIS) and by approximate type code (THETA), and the marked differences in the heating rates between the two procedures were noticed. Since the approximate type codes are used for parametric design studies, it was important to be discreet with the results. This study was undertaken to find out the reasons for the large differences between the two codes.

As seen in Figure 6-9, the cold wall radiative heating rates, computed by the two codes, at and near the stagnation point up to a s/R_N

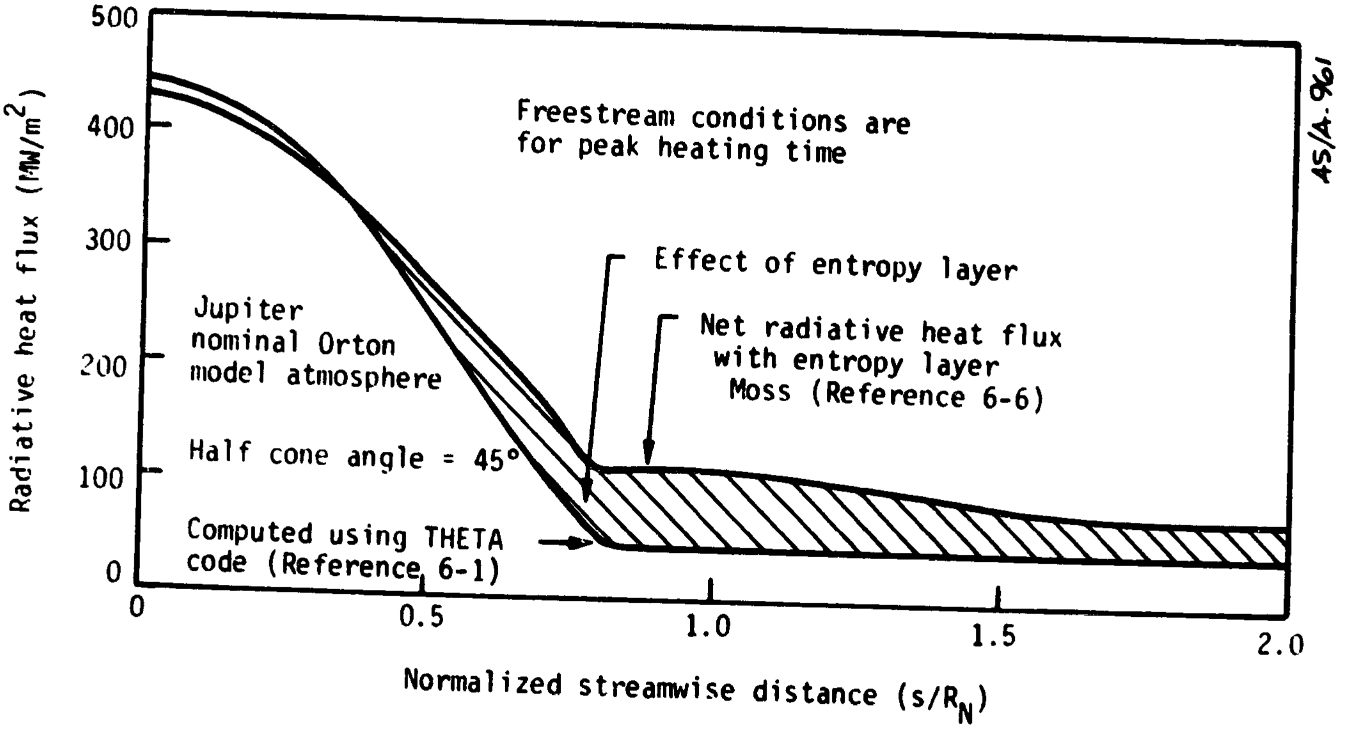

Figure 6-9. Effect of Entropy Layer on Radiative Heat Flux Distribution

value of 0.4 are nearly equal. However, for values of s/R_N larger than 0.4, the heating rates between the two codes differ by a factor of 2. To analyze the differences, a particular streamwise location, $s/R_N = 0.79$, was selected.

Moss (Reference 6-6), using the HYVIS code, solved the thin shock layer equations and obtained the temperature and pressure distributions in the shock layer. Figure 6-10 presents the shock layer properties, for the selected trajectory point, as obtained by Moss. In addition, Figure 6-10 shows the shock layer conditions obtained by the THETA code; the shock layer is assumed to be uniform in the THETA code. According to the HYVIS code, most of the shock layer is at a higher temperature compared to the shock (surface) temperature. This is due to the entropy layer and its effect was considered in detail in Section 3.

From Figure 6-10, it can be also seen that the entropy layer does not markedly affect the pressure distribution in the shock layer. Therefore, the assumption of uniform pressure in the shock layer is valid; however, the assumption of uniform temperature is not valid. The higher temperature entropy layer contributes significantly to the radiative flux.

To check the computations of HYVIS, the temperature and pressure distributions in the shock layer are input into the RADICLE code. Assuming that the shock layer is nonuniform, and using the shock standoff distance calculated by the HYVIS code, the RADICLE code was used to predict the radiative flux to the wall equaled to 105 MW/m^2 which compared well with that predicted by HYVIS, which was equal to 107.2 MW/m^2. Figure 6-11 illustrates the results. Though there are differences in the spectral radiative heat fluxes to the wall, the integrated values agree reasonably well. Figure 6-11 compares only the

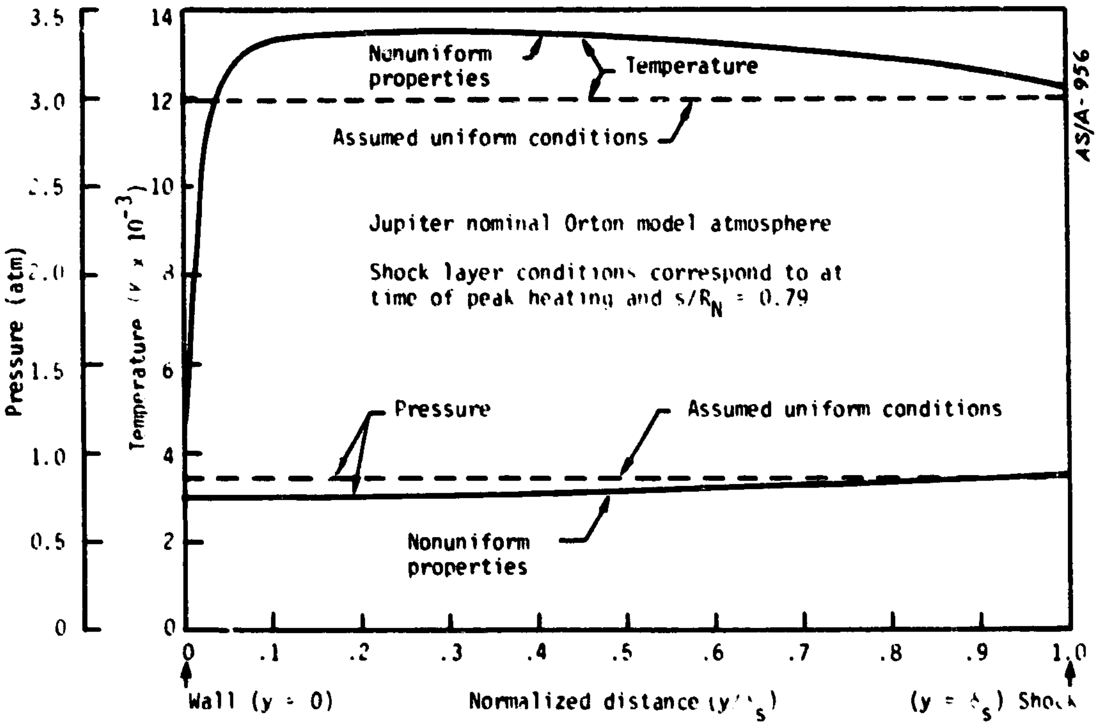

Figure 6-10. Effect of Entropy Layer on the Shock Layer Thermodynamic Conditions

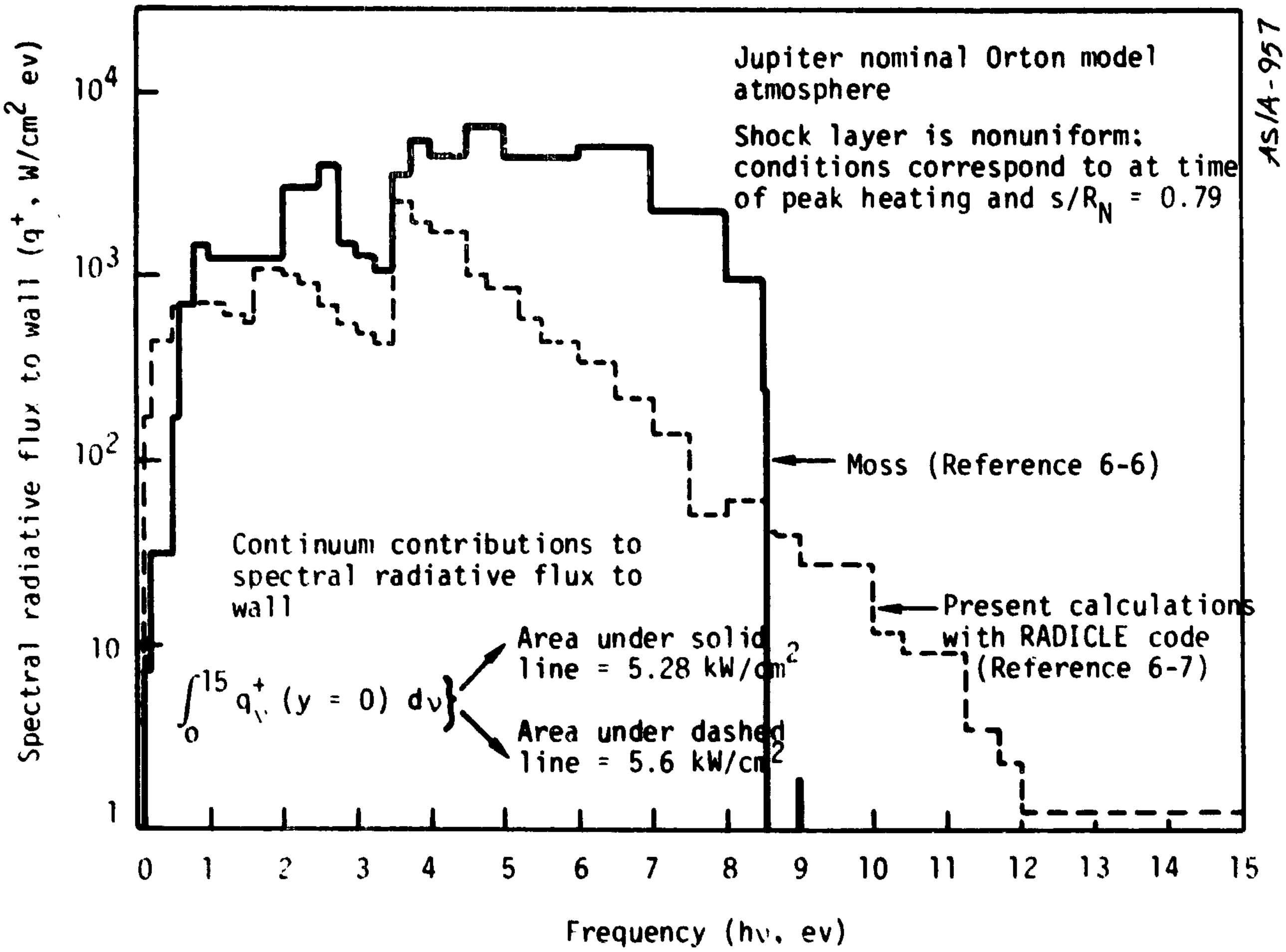

AS/A-957

Figure 6-11. Comparison of Continuum Spectral Radiative Flux to the Wall continuum spectral fluxes. Similar agreement for line spectral fluxes were also obtained.

In summary, this study indicated that the uniform shock layer assumption leads to erroneous results. The nonuniformity in the shock layer results because of the entropy layer. The available approximate computer codes to predict the radiative heating rate history are to be modified to include the entropy layer affects.

6.4 REFERENCES

6-1. Balakrishnan, A., Laub, B., Chu, E., and Nicolet, W. E., "Outer Planet Probe Thermal Protection: Heating Environments and Spallation Assessment," Acurex Final Report to NASA-Ames Research Center, 1978.

6-2. Anon., "The Planet Jupiter (1970)," SP-8069, December 1971, NASA.

6-3. NASA-Ames Research Center, Galileo Project Office, "Interim Jupiter Model Atmospheres," April 1977.

6-4. NASA-Ames Research Center, Galileo Project Office, "Jupiter Atmosphere Models," January 1978.

6-5. Brauer, G. L., Cornick, D. E., Habeger, A. R., Petersen, F. M., and Stevenson, R., "Program to Optimize Simulated Trajectories (POST)," CR-132689 through CR-132691, NASA, 1975.

6-6. Moss, J. N., "Study of the Aerothermal Entry Environment for the Galileo Probe," AIAA Paper No. 79-1081, presented at Orlando, Florida, June 4-6 1979.

6-7. Nicolet, W. E., "User's Manual for RAD/EQUIL/1973, A General Purpose Radiation Transport Program," CR-132470, NASA, 1973.

6-8. Nicolet, W. E., and Balakrishnan, A., "RASLE User's Manual," UM-79-10/AS, Acurex Corporation/Aerospace Systems Division, Mountain View, California, July 1979.